CENTRO DE INVESTIGACIONES
EN OPTICA, A.C.

DESIGN, FABRICATION AND INVESTIGATION OF SPECIAL PHOTONIC CRYSTAL FIBERS FOR MULTIPARAMETER SENSING

Tesis que para obtener el grado de Doctor en Ciencias (Óptica)

Presenta: Mauricio Salazar Sicachá

Director de Tesis: Dr. Uladzímir Minkóvich

versión definitiva. Incluye cambios sugeridas por revisores

León · Guanajuato · México
Agosto de 2024

Dedicated to my father DARIO SALAZAR MARTINEZ
to my mother Luz Marina Sicachá Penagoz
to my siblings Dario and Claudia Milena
to my maternal grandmother ANA BERTILDA
and to all my Family.

Acknowledgment

This doctoral thesis was carried out thanks to the Center for Research in Optics (CIO), which provided its facilities, and the National Council of Science and Technology (CONAHCYT), which gave a scholarship as financial support.

Thanks to my entire family, especially to my parents Dario S. M. and Luz Marina P. S., to the adviser and colleagues for all their contributions, and be it in my professional academic training, comprehensive personal training, or for their collaboration in carrying out the different stages of this work.

Thanks to Dr. Uladzimir Minkovich for all his work and enormous dedication during the completion of this thesis. Finally, thanks to the synodal committee of this thesis and to the Dr. Alexander B. Sotsky and his research group for their review work and all their observations and contributions.

Acronyms

PCF Photonic Crystal Fiber

NA Numerical Aperture

LMR Lossy Mode Resonance

RI Refractive Index

FDTD Finite-Difference Time-Domain

OSA Optical Spectrum Analyzer

SMF Single Mode Fiber

MMF Multimode Fiber

FBG Fiber Bragg Grating

LPFG Long Period Fiber Grating

EDFA Erbium-Doped Fiber Amplifier

SPR Surface Plasmon Resonance

OTDR Optical Time-Domain Reflectometer

SMPCF Single Mode Photonic Crystal Fiber

MMPCF Multimode Photonic Crystal Fiber

Abstract

In this work, a special two-ring single-mode photonic crystal optical fiber with high losses of the fundamental mode is designed for multiparameter sensing applications using the lossy mode resonance phenomenon. To achieve this phenomenon, a photonic crystal fiber with an absorptive coating was analyzed, and causal relationships between design parameters and system response were found. Subsequently, a pair of optical fibers were manufactured by varying the microstructure, and a setup was implemented using bending to promote confinement losses. Tests were then conducted to corroborate the existence of resonant modes through the influence of the coating.

Resumen: En este trabajo se diseña una fibra óptica de cristal fotónico monomodal de 2 anillos con altas pérdidas en el modo fundamental para aplicaciones en sensado multiparamétrico, utilizando el fenómeno de resonancia de modos débiles. Para esto, se analizó un sistema de fibra de cristal fotónico con recubrimiento absorbente y se encontraron relaciones causales entre parámetros de diseño y la respuesta del sistema. Posteriormente, se fabricó un par de fibras ópticas variando la microestructura y se implementó un setup de estas utilizando un bending para favorecer las pérdidas por confinamiento, y luego se hicieron pruebas para corroborar la existencia de modos débiles resonantes mediante la influencia del recubrimiento.

List of Figures

List of Tables

Contents

Introduction

In the last decade of the past millennium, a photonic crystal or microstructured optical fiber was developed as a consequence of continuous scientific and technological advances in physics and engineering [1, 2]. This led to the emergence of multiple research studies in the field of photonics and physical optics due to the scientific and technological potential of these types of devices [3, 4].

Photonic crystal fiber (PCF) technologies represent a significant advancement for basic science, technology, and industry due to their unique capabilities and versatility [5, 6]. In basic science, these fibers enable the exploration of new physical and optical phenomena thanks to their ability to manipulate light in ways not possible with conventional optical fibers [7]. For example, PCFs can confine light in an air core, allowing the investigation of light-matter interactions under conditions that mimic a vacuum [8]. Additionally, their capacity to guide light through materials with exotic optical properties has facilitated the study of new states of matter and the development of highly sensitive sensors [9].

In the technological and industrial fields, PCFs have revolutionized data transmission and communications, offering higher speeds and bandwidths than traditional technologies [10]. These fibers are essential for the development of high-capacity optical communication systems, which are fundamental for modern internet and telecommunications infrastructure [11]. Additionally, in the industry, they are used in sensor applications for environmental, medical, and structural monitoring due to their high sensitivity and precision [12]. For instance, sensors based on PCFs can detect mini-

mal changes in temperature, pressure, and chemical composition, which is crucial for applications in areas such as biomedicine and industrial monitoring [13, 14]. These applications not only improve the efficiency and safety of industrial processes but also open new possibilities for the development of emerging technologies [15, 16].

Thus, in the last decade, various devices and physical systems based on PCFs have been reported, aiming to complement, improve, or even invent methodologies that allow the acquisition of new technologies or the understanding of physical phenomena that enable the continued and enhanced technological development of modern society, both at the academic and industrial research levels, in fields that are transversal [17, 18].

Now, physical and chemical optical fiber sensors that use Lossy Mode Resonance (LMR) have been the subject of intensive research [19, 20]. LMR occurs due to the interaction of light propagating through an optical fiber coated with an absorbing film with suitable optical properties. If the modes supported by the coating are in phase matching with the modes of the fiber, then the fiber modes can couple to the coating modes, generating a lossy mode. LMR will undergo variation if the properties of the film (either the refractive index or thickness) change or if changes occur in the optical properties of the surrounding medium. These variations result in a detectable modulation of the fiber's transmission spectrum, which constitutes a sensing effect [19, 20].

In most cases, the devices used to generate LMR are typically standard optical fibers in which the mode propagation constants exceed the refractive index of the coating [20]. Thus, phase-matching modes in the fiber and the coating have evanescent fields in the fiber's coating region without any form of resonance. This implies that coupling of these modes requires close contact between the fiber core and the absorbing film. This necessitates removing a portion of the fiber's coating and using a different coating material in its place to generate resonance [19].

The LMR phenomenon, as explained earlier, is generated through the coupling in the coating of the energy contained by the fundamental mode. The fundamental mode is characterized by having a circular pattern with graduated intensity within a transverse trace when inspecting the output signal in an optical fiber [21, 22]. This pattern has higher intensity at the center than at the ends, and its intensity values are typically associated with a Gaussian distribution. When the conditions for the propagation of only the fundamental mode within an optical fiber are met, it can be said that all signals traveling through the core follow the same optical path under the paraxial approximation. This considerably reduces the number of internal reflections and, therefore, decreases optical power losses, allowing signals to travel much longer distances or alternatively facilitating the efficient detection of changes in the transmission spectrum. On the other hand, in the multimodal regime, we can observe an intensity pattern resulting from the combination of different pure and hybrid electromagnetic propagation modes of higher order [23, 24]. In other words, an optical fiber operating in this regime allows for significant differences in the optical paths of the propagated rays, increasing the number of internal reflections and thus increasing energy losses. This limits the propagation range and sensitivity of the fiber compared to an optical fiber operating in the single-mode regime.

Now, in standard optical fibers the work regime is determined by the diameter of the core. The larger the diameter, the greater the number of modes the optical fiber can support for a specific wavelength. On the other hand, within the design of special optical fibers, PCFs can be used to modify the optical properties of the waveguide based on the microstructure defined for the fiber [25]. By modifying the lattice parameters of the microstructure, it is possible to achieve single-mode operating regimes for specific wavelengths and it is also possible to increase the fundamental mode losses to facilitate the creation of loss modes presented in the LMR phenomenon.

In this work, we consider the possibility of obtaining LMR using a PCF with high losses (HL-PCF) instead of standard fiber due to the mentioned limitations [19]. The

proposal is based on the idea that if a PCF is formed by a finite number of air channels in a dielectric matrix, then the mode propagation constants within the PCF are typically lower than the refractive index of the matrix (in contrast to conventional fibers) [25]. As a result, the modes leak from the fiber core, meaning the modes experience confinement losses. In PCFs, coupling occurs between the confinement loss modes and the modes of the coating by phase-matching. Coupling of filtered modes from different waveguides (fiber-coating) can occur at a significant distance between the guides. This makes it possible to obtain LMR due to the coupling between the core modes of the PCF and the modes of an absorbing film applied directly to the outer surface of the fiber's cladding without local modification of the cladding, as is the case with conventional fibers. The described LMR has the advantage of allowing single-mode operation in the sensor and also eliminates nearly all losses due to diffraction in PCF irregularities[19].

In this work, a PCF was designed and fabricated to increase confinement losses within the single-mode regime in the infrared region. Subsequently, sensing tests were conducted using the fabricated fibers through bending, which promotes system losses to enhance the likelihood of forming LMR. By analyzing the characteristic peaks of the loss pattern of the mentioned system for different concentrations of glycerin, a refractometer was obtained, intended to serve as the basis for a multiparameter sensing platform.

The design of the optical fiber was carried out by implementing a numerical method based on an experimental model proposed by Koshiba and Satoih, which allows for defining an appropriate single-mode regime based on the geometric parameters of the fiber's microstructure. The sensing device design was then developed by studying the LMR phenomenon in PCFs, working in collaboration with Dr. Sotsky's group to obtain sufficient calculations and to analyze the corresponding physical system. Subsequently, the microstructural parameters were rescaled to define the dimensions of all the elements of the preform (stack) and the fabrication process was

carried out using the drawing tower at the Center for Optical Research (CIO). Finally, the fabricated optical fiber was used to construct a sensing system by incorporating bending in the fiber to enhance losses and the formation of LMR, allowing the measurement of refractive index variations. Characterizations were obtained for glycerin concentrations.

Thus, the design and fabrication of a multiparameter sensing platform were carried out using a system composed of PCF with high confinement losses, to which bending was applied to promote the formation of LMR in the coating. During the study of the sensing system design, two scientific articles were published, the results of which contribute to the construction of the theoretical framework that allows for understanding the physics of the LMR phenomenon in the PCF-coating system through causal relationships between the design parameters and the system response. Finally, this multiparameter sensing system was used to characterize the concentration of glycerin by studying the LMR peaks.

Bibliography

[1] R.S. Windeler J.K. Ranka and A.J. Stentz. *Visible continuum generation in air-silica microstructure optical fibers with anomalous dispersion at 800 nm.* Opt. Lett., vol. 25, no. 1, pp. 25-27, 2000.

[2] T.A. Birks A. Ortigosa-Blanch W.J. Wadsworth J.C. Knight, J. Arriaga and P.S.J. Russell. *Anomalous dispersion in photonic crystal fiber.* IEEE Photon. Technol. Lett., vol. 12, no. 7, pp. 807-809, 2000.

[3] P.St.J. Russell J.C. Knight, T.A. Birks and D.M. Atkin. *All-silica single-mode optical fiber with photonic crystal cladding.* Opt. Lett., vol. 21, no. 19, pp. 1547-1549, 1996.

[4] P.St.J. Russell. *Photonic-crystal fibers.* J. Lightw. Technol., vol. 24, no. 12, pp. 4729-4749, 2006.

[5] J.D.C. Jones D. Mogilevtsev-T.A. Birks J.C. Knight M.J. Gander, R. McBride and P.S.J. Russell. *Experimental measurement of group velocity dispersion in photonic crystal fibre.* Electron. Lett., vol. 35, no. 1, pp. 63-64, 1999.

[6] P. Mergo Z. Holdynski, M. Napierala and T. Nasilowski. *Experimental investigation of supercontinuum generation in photonic crystal fibers pumped with sub-ns pulses.* J. Lightw. Technol., vol. 33, no. 10, pp. 2106-2110, 2015.

[7] P. St. J. Russell. Photonic crystal fibers. *Science*, 299(5605):358–362, 2003.

[8] J. C. Knight, T. A. Birks, P. St. J. Russell, and D. M. Atkin. All-silica single-

mode optical fiber with photonic crystal cladding. *Optics Letters*, 21(19):1547–1549, 1996.

[9] T. M. Monro, D. J. Richardson, and P. J. Bennett. Sensing with microstructured optical fibres. *Measurement Science and Technology*, 12(7):854–858, 1999.

[10] T. A. Birks, J. C. Knight, and P. St. J. Russell. Endlessly single-mode photonic crystal fiber. *Optics Letters*, 22(13):961–963, 1997.

[11] B. J. Eggleton, C. M. de Sterke, and R. E. Slusher. Bragg solitons in the nonlinear schrödinger limit: Experiment and theory. *Journal of the Optical Society of America B*, 16(4):587–599, 1999.

[12] A. Cucinotta, S. Selleri, M. N. Zervas, and J. L. Auguste. Design optimization of photonic crystal fiber lasers. *IEEE Journal of Quantum Electronics*, 42(11):1079–1086, 2006.

[13] X. Jiang, W. Jin, M. S. Demokan, and C. C. Chan. Optical fiber humidity sensor based on a side-polished fiber coupler. *Optics Communications*, 202(1-3):121–125, 2002.

[14] J.H.V. Price F.Poletti F. He M.L.V. Tse, P. Norak and D.J. Richardson. *Pulse compression at 1.0 μm in dispersion-decreasing holey fibers.* Opt. Lett., vol. 31, no. 23, pp. 3504-3506, 2006.

[15] J. Kou, J. Luo, G. Chen, and H. Ye. Temperature-insensitive fiber bragg grating based on photonic crystal fiber. *Optics Letters*, 32(3):336–338, 2007.

[16] A. Mussot A. Kudlinski, S.F. Wang and M. Conforti. *Soliton annihilation into a polychromatic dispersive wave.* Opt. Lett., vol. 40, no. 9, pp. 2142-2145, 2015.

[17] H.N. Paulsen C.K. Nielsen K. Molmer S. Keiding K.M. Hilligsoe, T.V. Andersen. *Supercontinuum generation in a photonic crystal fiber with two zero dispersion wavelengths.* Opt. Express, vol. 12, no. 6, pp. 1045-1060, 2004.

[18] A.B. Rulkov B.A. Cumberland A.K. George S.V. Popov J.C. Travers, J.M. Stone. *Optical pulse compression in dispersion decreasing photonic crystal fiber.* Opt. Express, vol. 15, no. 20, pp. 13203-13211, 2007.

[19] I. Del Villar, F. J. Arregui, C. R. Zamarreño, J. M. Corres, C. Bariain, J. Goicoechea, C. Elosua, M. Hernaez, P. J. Rivero, A. B. Socorro, A. Urrutia, P. Sanchez, P. Zubiate, D. Lopez, N. De Acha, J. Ascorbe, and I. R. Matias. Optical sensors based on lossy-mode resonances. *Sensors and Actuators B: Chemical*, 240:174–185, 2017.

[20] A. Ozcariz, C. Ruiz-Zamarreño, and F. J. Arregui. A comprehensive review: Materials for the fabrication of optical fiber refractometers based on lossy mode resonance. *Sensors*, 20(7):1972, 2020.

[21] Roberta Conlan y T.A. Heppenheimer. *Las comunicaciones modernas: la revolución del láser y la fibra óptica.* National Academy of Sciences, 2019.

[22] Regis J. Bates. *Optical Switching and Networking Handbook.* McGraw-Hill, 2001.

[23] Casimer DeCusatis. *Handbook of Fiber Optic Data Communication: A Practical Guide to Optical Networking, 4th Edition.* Elsevier Academic Press, 2014.

[24] José María Hernández y María Teresa Martín Sánchez Manuela Martín Sánchez, Gabriel Pinto. *El aparato de Colladon y su relación con la fibra óptica: Reseña histórica y aplicaciones didácticas.* Notas de clase, researchGate, septiembre de 2015.

[25] Masanori Koshiba Kunimasa Saitoh. *Empirical relations for simple design of photonic crystal fibers.* Optical Society of America, Optics Express, Vol. 13, No. 1, pp. 267-274, 2005.

Objectives

General objective

Fabricate and investigate special photonic crystal fibers for multiparameter sensing.

Specific objectives

Design a multiparametric sensing system based on photonic crystal fiber to study the formation of Lossy Mode Resonance in an absorbing coating.

Establish causal relationships between the design parameters and the LMR response in a PCF through computational calculations.

Manufacture a serie of single-mode photonic crystal optical fibers with high confinement losses.

Build a multiparameter sensing platform that allows measuring variations in refractive index using a single-mode optical fiber with high confinement losses.

Chapter 1

Fundaments of Fiber Optics

1.1 Guided waves

A PCF is a waveguide. For this reason, it is of our interest to describe in this chapter the physical foundations that allow its theoretical conceptualization. In the first instance, the description of this physical system is done by considering the propagation of an electromagnetic wave (EM wave) in a material medium characterized by possessing a particular geometry. All of this is accomplished by solving the equations proposed by James Clerk Maxwell (a Scottish physicist) in 1865, which can have an analytical or numerical solution depending on the complexity of the problem. Its solution is achieved through numerical methods such as finite difference methods in the time domain or in the frequency domain (FDTD: Finite Differences Time Domain or FDFD: Finite Differences Frequency Domain, respectively). The latter method involves a domain change and is made possible through the use of Fourier theory, specifically its canonical transformation that allows transitioning from the time domain to the spectral domain. The solution of the Maxwell's equations enables determining how the propagation of EM waves can occur within waveguides. By this, we specifically refer to the ways in which the EM field can be distributed within a waveguide according to a corresponding set of propagation constants (β_i). Subsequently, based on this, we can understand how, from Maxwell's equations, one can calculate the distribution of the electric field in a waveguide with cylindrical sym-

metry to study its possible propagation modes associated with the electromagnetic field [1]. This will allow us to configure what is understood as the Fiber Optic (FO) and then define its optical properties [2, 3].

1.1.1 Maxwell's Equations in Materials

A waveguide is any material object that allows for the manipulation of electromagnetic radiation in such a way that its propagation can be controlled. This specifically refers to controlling the path followed by a beam of light when it is confined within a material and allows for controlled propagation of radiation within it. To achieve this, the principle of total internal reflection (TIR) exhibited by electromagnetic radiation when it transitions from one medium to another is utilized. This results in an angular deviation from its propagation direction away from the normal, and beyond a certain angle of incidence, this deviation causes the radiation to continuously reflect along the material [4]. Below is the total internal reflection condition derived from Snell's law for a transmission angle of $\pi/2$, n_1 and n_2 are the refractive indices of the media, θ_1 y θ_2 are the angles of incidence and transmission respectively which are measured from the normal of the interface to the incident or transmitted beam, all of this information being contained in the same plane known as the plane of incidence:

$$n_1 \sin\theta_1 = n_2 \sin\theta_2, \tag{1.1}$$

$$\theta_1 = \arcsin(\frac{n_2}{n_1}), \quad n_2 > n_1. \tag{1.2}$$

As already mentioned, a mathematical description of the propagation of a light beam through a material can be given using Maxwell's equations. Electromagnetic radiation is composed of two fields that oscillate in time, generating each other throughout space and can be described as two functions $\vec{E}(\vec{r},t)$ y $\vec{H}(\vec{r},t)$, where by using the method of separation of variables to solve the differential equations that satisfy it can be obtained that the temporal part has a complex exponential solution whose argument is negative and depends on the product between the angular velocity ω and the time t, all this just for a monochromatic electromagnetic (EM) wave [2]. Thus,

the equations that must satisfy these fields have the form:

$$\vec{\nabla} \cdot (\epsilon_0 n^2 \vec{E}) = \sigma, \tag{1.3}$$

$$\vec{\nabla} \cdot (\mu_0 \vec{H}) = 0, \tag{1.4}$$

$$\vec{\nabla} \times \vec{E} = -\mu_0 \frac{\partial \vec{H}}{\partial t} = i\omega\mu_0 \vec{H} = i\sqrt{\frac{\epsilon_0}{\mu_0}} k\vec{H}, \tag{1.5}$$

$$\vec{\nabla} \times \vec{H} = \vec{J} + \epsilon_0 n^2 \frac{\partial \vec{E}}{\partial t} = \vec{J} - i\omega\epsilon_0 n^2 \vec{E} = \vec{J} - i\sqrt{\frac{\epsilon_0}{\mu_0}} k n^2 \vec{E}, \tag{1.6}$$

of which, considering that the electrical permittivity (ϵ) and magnetic permeability (μ) do not change in time but only in space ($\vec{r}$) and which can also be written as $\epsilon(\vec{r}) = n^2(\vec{r})$ and also because in practice the magnetic contribution of the materials that serve as a medium is considered weak, it has to be $\mu = \mu_0$, wave equations can be constructed that must satisfy both fields [2]. The wave equation for the electric and magnetic field has the form:

$$(\vec{\nabla}^2 + k^2 n^2)\vec{E} = -\vec{\nabla}(\vec{E} \cdot \vec{\nabla}\ ln\ n^2) - i\sqrt{\frac{\mu_0}{\epsilon_0}} \left\{ \vec{J} + \frac{1}{k}\vec{\nabla}(\frac{\vec{\nabla} \cdot \vec{J}}{n^2}) \right\}, \tag{1.7}$$

$$(\vec{\nabla}^2 + k^2 n^2)\vec{H} = (\vec{\nabla} \times \vec{H}) \times \vec{\nabla}\ ln\ n^2 - \vec{\nabla} \times \vec{J} - \vec{J} \times \vec{\nabla}\ ln\ n^2. \tag{1.8}$$

Now, to find the solutions to these wave equations, we need to define the boundary conditions and initial conditions and rewrite the problem in the coordinate system that best fits the geometry presented.

Specifically, in the case of PCFs, their boundary conditions will be given by the structure of the photonic crystal, which can be characterized by including the periodic variations of the electrical permittivity $\epsilon(\vec{r})$, On the other hand, the initial conditions and geometry of the waveguide are identical to those used for a conventional FO. The solution of this approach for PCFs is done by using the generalized plane wave method that encompasses the vector nature of Maxwell's equations [5]. This method is an extension of the scalar plane wave method widely used in solving the Schrödinger wave equation for electrons immersed in periodic potentials. Specifically, the previous problem of finding solutions to the wave equation for a PCF can be rewritten as an

eigenvalue problem, where it is then possible to obtain its solution through numerical simulation by applying the aforementioned plane wave method. This method incorporates the use of Bloch's theorem, transforming the direct space into reciprocal space by introducing Fourier series expansions and their transforms. This approach allows us to determine the permitted and forbidden energy bands that arise due to the periodicity exhibited by the functions describing this physical system, which is characterized by having a periodic lattice structure [5].

1.1.2 Optical Fibers: Cylindrical Coordinates

To solve the system of equations posed in the previous section, it is necessary to introduce the Laplacian operator as the sum of its transverse component (XY plane) plus its longitudinal component (z-axis). This is possible because an optical fiber remains invariant under longitudinal translations. Similar to the temporal solution obtained for the longitudinal component, it is possible to perform a separation of variables, and the solution is analogous. However, the product inside the argument of the negative imaginary exponential now involves the propagation constant β and the z-component of the position vector [2]. Thus, considering that there are no net nonzero current densities or point charges in the material where the electromagnetic wave propagates, the previous problem can be reformulated as follows:

$$\vec{E}(\vec{r},t) = \vec{e}(\vec{r}_t)e^{i(\beta z-\omega t)}, \tag{1.9}$$

$$\vec{H}(\vec{r},t) = \vec{h}(\vec{r}_t)e^{i(\beta z-\omega t)}, \tag{1.10}$$

$$\vec{\nabla} = \vec{\nabla}_t + \hat{z}\frac{\partial}{\partial z} = \hat{r}\frac{\partial}{\partial r} + \frac{\hat{\phi}}{r}\frac{\partial}{\partial \phi} + \hat{z}\frac{\partial}{\partial z}, \tag{1.11}$$

$$(\vec{\nabla}_t^2 + k^2n^2 - \beta^2)\vec{e} = -(\vec{\nabla}_t + i\beta\hat{z})(\vec{e}_t \cdot \vec{\nabla}_t \; ln \; n^2), \tag{1.12}$$

$$(\vec{\nabla}_t^2 + k^2n^2 - \beta^2)\vec{h} = ((\vec{\nabla}_t + i\beta\hat{z}) \times \vec{h}) \times \vec{\nabla}_t \; ln \; n^2. \tag{1.13}$$

The above system of equations must be solved for each of the components of the electric and magnetic fields. For this purpose, equations 1.5 and 1.6 are utilized,

enabling the expression of the transverse components of these fields in terms of combinations of their longitudinal components of the electric and magnetic fields. Thus, we have:

$$e_r = \frac{1}{n^2k^2 - \beta^2}\left\{\beta\frac{\partial\ ie_z}{\partial r} + \sqrt{\frac{\mu_0}{\epsilon_0}}\frac{k}{r}\frac{\partial\ ih_z}{\partial\phi}\right\}, \tag{1.14}$$

$$e_\phi = \frac{1}{n^2k^2 - \beta^2}\left\{\frac{\beta}{r}\frac{\partial\ ie_z}{\partial\phi} - \sqrt{\frac{\mu_0}{\epsilon_0}}k\frac{\partial\ ih_z}{\partial r}\right\}, \tag{1.15}$$

$$h_r = \frac{1}{n^2k^2 - \beta^2}\left\{\beta\frac{\partial\ ih_z}{\partial r} - \sqrt{\frac{\mu_0}{\epsilon_0}}\frac{kn^2}{r}\frac{\partial\ ie_z}{\partial\phi}\right\}, \tag{1.16}$$

$$h_\phi = \frac{1}{n^2k^2 - \beta^2}\left\{\frac{\beta}{r}\frac{\partial\ ih_z}{\partial\phi} + \sqrt{\frac{\mu_0}{\epsilon_0}}kn^2\frac{\partial\ ie_z}{\partial r}\right\}. \tag{1.17}$$

Finally, by substituting these relationships into the system generated by equations 1.12 and 1.13, coupled differential equations for the longitudinal components of both fields are obtained. The solution of these equations automatically allows for the calculation of the other components. As mentioned earlier, there is a direct relationship between the longitudinal and transverse components. The coupled equations are presented below:

$$\vec{\nabla}_t^2 e_z + (n^2k^2 - \beta^2)e_z - \frac{d\ ln\ n^2}{dr}\frac{\beta}{(n^2k^2 - \beta^2)}\left\{\beta\frac{e_z}{\partial r} + \sqrt{\frac{\mu_0}{\epsilon_0}}\frac{k}{r}\frac{\partial h_z}{\partial\phi}\right\} = 0, \tag{1.18}$$

$$\vec{\nabla}_t^2 h_z + (n^2k^2 - \beta^2)h_z - \frac{d\ ln\ n^2}{dr}\frac{n^2k^2}{(n^2k^2 - \beta^2)}\left\{\frac{h_z}{\partial r} + \sqrt{\frac{\epsilon_0}{\mu_0}}\frac{\beta}{kr}\frac{\partial e_z}{\partial\phi}\right\} = 0. \tag{1.19}$$

1.1.3 Propagation Modes

Now, it will be important to define what modes of propagation will exist in the waveguide based on the values assigned to its components. In particular, there are transverse electric (TE) and transverse magnetic (TM) modes that are defined by nullifying their respective z-components [2]. That is, a TE mode has a null e_z component, and a TM mode has a null h_z component. Now, when both components are null, we refer to them as transverse electromagnetic (TEM) modes, which are the typical modes under which electromagnetic waves propagate in a vacuum. Finally, in general, when there are no null components, we refer to them as hybrid modes

HE and EH [2]. Below is a diagram showing the first propagation modes present in an optical fiber according to their characteristic parameters such as normalized frequency (V) and normalized propagation constant (β). This diagram illustrates the different modes and their regions based on characteristic parameters in an optical fiber, providing a visual representation of the variety of propagation modes supported by the waveguide.

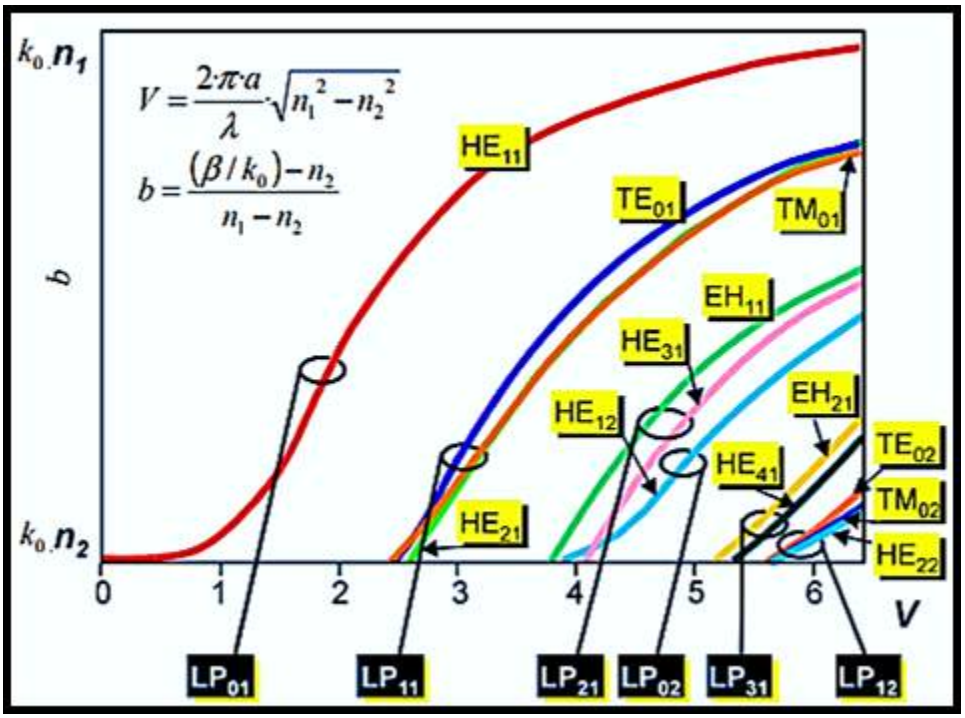

Figure 1.1: *Diagram β vs V showing the first modes of propagation of an FO* [6].

Now, the propagation modes generated by a cylindrical resonator are the $TEM_{\rho,l}$ modes, where ρ is the radial number representing the quantity of concentric rings associated with intensity, and l is the angular number representing the quantity of divisions associated with the radial structure [2]. The modes propagated in an optical fiber are of a vectorial nature and can be approximated using scalar mode theory through the linear polarization of the modes ([2] and [6]). This is achieved by grouping the different modes into sets using $LP_{n,m}$, where the indices n and m traverse the mode groups distributed on the β vs V diagram, as shown previously. Below, the $TEM_{\rho,l}$ modes generated by a cylindrical resonator are illustrated in the diagram

that illustrates the $TEM_{\rho,l}$ modes generated by a cylindrical resonator. The radial number ρ and angular number l determine the characteristics of these modes, and they are distributed in groups on the β vs V diagram.

The donut mode TEM^*_{0i} is a specific laser beam pattern formed by the superposition of two TEM^*_{0i} modes, where i is an integer (e.g., 1, 2, 3). To create this mode, one TEM^*_{0i} mode is rotated by an angle of $\frac{360^\circ}{4i}$ relative to the other before they are combined. This rotation and superposition result in a beam profile with a dark central region and a bright, ring-like intensity distribution, giving it a donut appearance. The syntax for describing this mode is TEM^*_{0i}, where i indicates the specific configuration of the superimposed modes.

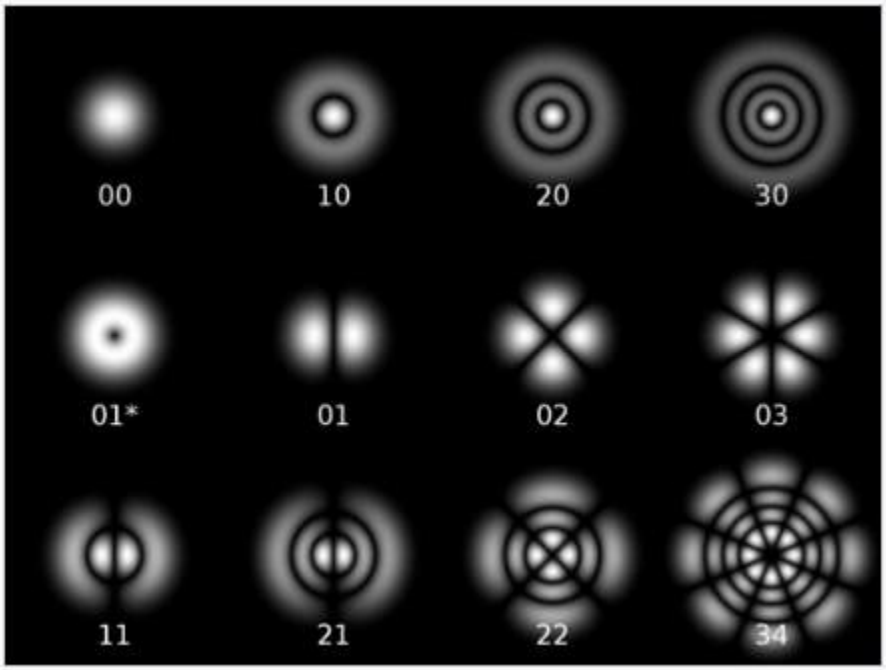

Figure 1.2: *$TEM_{\rho,l}$ propagation modes generated by a cylindrical resonator* [7].

1.2 Properties of Optical Fibers

There are several important characteristics in optical fibers (FO) such as: Numerical Aperture, Normalized Frequency, Attenuation, and Cutoff Wavelength. These characteristics are crucial as they determine the mode and efficiency of operation of an

optical fiber.

1.2.1 Numerical Aperture (NA):

The numerical aperture of an optical fiber provides an indication of how many light rays can satisfy the condition of total internal reflection (TIR) along the fiber. Its value is calculated as the square root of the difference of the squares of the refractive indices of the core n_1 and the cladding n_2, respectively, or the product of the sine of the maximum angle $\theta_{\max}$ that satisfies TIR and the refractive index of the medium n_0 where the fiber is located ([6] and [1]). Mathematically, it is expressed as:

$$NA = \sqrt{n_1^2 - n_2^2} = n_0 \ sin(\theta_{max}). \tag{1.20}$$

This measure is fundamental for understanding the fiber optic's ability to collect and guide light, and a higher numerical aperture value typically indicates greater light-capturing capacity and improved signal transmission efficiency.

For other hand, numerical aperture also determines the resolution of an optical system together diffraction which also influences what can be resolved. Diffraction is a phenomenon that causes light to scatter as a wave. This property prevents even the highest resolution lens from being able to focus on a single pinpoint source, resulting in the focal point being more of a disk than a point. The smallest resolvable disk of light is known as the Airy disk, and its radius is expressed by the following formula

$$r = 0.61 \ \lambda/NA \tag{1.21}$$

The value of this formula represents the resolution. According to this equation, the higher the numerical aperture, the smaller the radius of the Airy disk. Therefore, a lens with a higher NA can resolve smaller features, leading to a sharper image.

1.2.2 Normalized Frequency

The normalized frequency provides an indication of the number of modes a fiber optic can support and is directly proportional to the numerical aperture. For values of normalized frequency less than 2.405, it is said that an optical fiber operates in the single-mode regime, and for values greater than or equal to this threshold, the fiber optic transitions to the multimode regime ([6] and [1]). The limit at which the transition from one regime to another occurs is characterized by the cutoff frequency that the source coupled into the fiber must have. Mathematically, the normalized frequency is expressed as:

$$V = \frac{2\pi}{\lambda}\ a\ NA. \tag{1.22}$$

Where $\frac{2\pi}{\lambda}$ is the wave vector associated with the source coupled into the optical fiber, a is the diameter of the optical fiber, and NA is its numerical aperture. This parameter is crucial for determining the number of modes a fiber can support and, consequently, significantly affects its performance in terms of transmission capacity and signal quality.

1.2.3 Attenuation

Attenuation is a measure of the transparency or purity of the material from which the optical fiber is made and is directly proportional to the material's absorption at a specific wavelength. This quantity can be calculated for a particular optical fiber using an Optical Spectrum Analyzer (OSA), which obtains the power spectrum in dBm of a white light source transmitted through the optical fiber at two instances: the first involves the measurement (P_0) over a short length (for example, $L_0 = 1m$) of the optical fiber, which is used as a reference, and the second involves another measurement (P_1) over a long length (for example, $L_1 = 10m$) of the optical fiber ([6] and [1]).

Finally, the calculation of attenuation can be obtained as the difference between these spectra. This subtraction yields the attenuation, providing information about

the loss of power as the light travels through the optical fiber over the specified lengths L_0 and L_1.

$$\alpha[dB/m] = -\frac{(P_1[dBm] - P_0[dBm])}{\Delta L[m]}, \tag{1.23}$$

where, additionally, there are the relationships:

$$P_1[W] = P_0[W] \cdot 10^{-\frac{\alpha\ \Delta L}{10}}, \tag{1.24}$$

$$P[dBm] = 10\log(\frac{P[mW]}{1mW}). \tag{1.25}$$

1.2.4 Fundamental mode

The fundamental mode of a Gaussian beam can be represented in intensity as follows:

$$I(r) = I_{max}\ e^{-r^2/2\omega_0^2}. \tag{1.26}$$

Where the intensity is a function of the radius (r) and decays as the argument is quadratic and negative, modulated by the squared width of the fundamental mode ω_0. The standard deviation is given by $\omega_0/2$ ([6] and [1]). Also, there is an interesting relationship involving the diameter of the incident beam (d_2) on a positive lens with the waist diameter (d_1) it generates. This relationship is expressed as follows:

$$d_2 = \frac{4\ \lambda\ f}{\pi\ d_1}. \tag{1.27}$$

Where λ and f are the wavelength of the source and the focal length of the lens, respectively. Finally, through the Marcuse equation, a mathematical relationship can be established between the effective mode radius (ω_{eff}) and the core radius (a_{eff}) of a single-mode optical fiber, which can be expressed as follows:

$$\frac{\omega_{eff}}{a_{eff}} = 0.65 + \frac{1.619}{V_{eff}^{1.5}} + \frac{2.879}{V_{eff}^{6}}. \tag{1.28}$$

Then, once the value of ω_0 is known, it is possible to calculate the numerical aperture

as:

$$NA = n_0 \ sin(\theta) = n_0 \ sin(tan^{-1}(\omega_0/L)). \tag{1.29}$$

Where L is the distance to the screen or reference point. This is illustrated below:

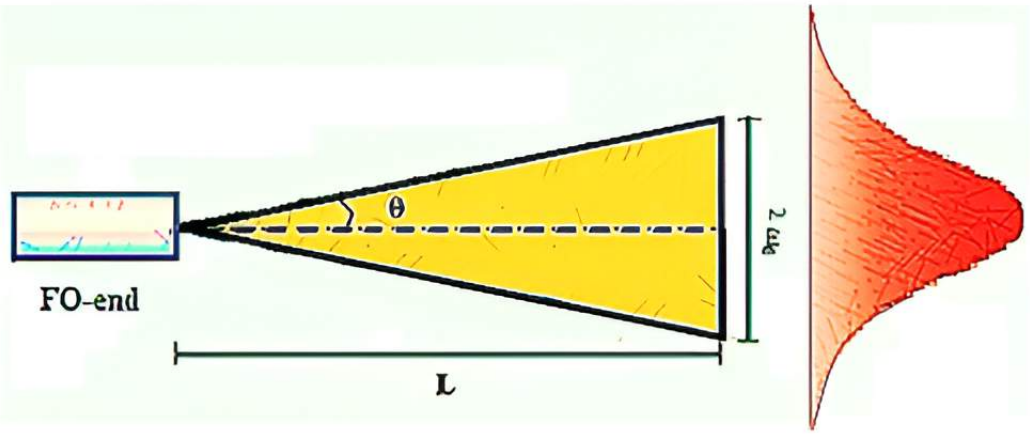

Figure 1.3: *Calculation of the numerical aperture from the width associated with the fundamental mode of propagation [8].*

1.2.5 Chromatic Dispersion

Chromatic dispersion (D) is a measure of the changes in refractive index at different wavelengths ([9] and [10]). It can be calculated as the variation of the inverse of the group velocity with respect to the wavelength in vacuum as:

$$D = \frac{d}{d\lambda}\left(\frac{1}{v_g}\right) = -\frac{\lambda}{c}\frac{d^2 n_{eff}}{d\lambda^2} + D_m. \tag{1.30}$$

Where, $D_m = \dfrac{dn_m}{c\ d\lambda}$ is known as the material dispersion and is calculated using the Sellmeier equation shown below:

$$n_m^2(\lambda) = 1 + \frac{B_1\lambda^2}{\lambda^2 - C_1} + \frac{B_2\lambda^2}{\lambda^2 - C_2} + \frac{B_3\lambda^2}{\lambda^2 - C_3}. \tag{1.31}$$

For each material there are different coefficients B_i and C_i with i = 1, 2, 3. Specifically for the case of silica, which is the material used in FOs, there are the following coefficients represented in the table 1.1

	B1	B2	B3	C1	C2	C3
Sílice	0.696166300	0.407942600	0.897479400	4.67914826 x$10^{-3}\mu m^2$	1.3512031 x $10^{-2}\mu m^2$	97.9340025 μm^2

Table 1.1: Sellmeier coefficients for SiO2.

On the other hand, Rayleigh dispersion is also present, contributing 96% of the losses present in an FO. The attenuation is subtended along the Rayleigh scattering, which traces a lower bound along it. Mathematically the attenuation due to this dispersion can be written as:

$$\alpha_R \propto \frac{k_B\ T_f}{\lambda^4} \tag{1.32}$$

Where k_B is the Boltzmann constant and T_f is the cooling temperature to which the material was subjected during its manufacture.

1.3 Photonic Crystals

Photonic crystals (PCs) are structures that possess a dielectric function with periodicity in one, two, or three dimensions, and their main characteristic is that they interact with different ranges of the electromagnetic spectrum depending on the scale of the structure's periodicity [5]. This interaction manifests when the scale order of the structure's periodicity coincides with the order of the scale at which electromagnetic radiation propagates through the PC [11]. Examples of these PCs in one and two dimensions are Bragg gratings in optical fibers and PCFs, respectively. On the other hand, it is generally stated that the range of wavelengths that cannot propagate in a PC defines the photonic gap or the forbidden energy band ([12] and [5]).

In 1887, Lord Rayleigh explained the phenomenon of reflection in a system composed of alternating dielectric layers with different refractive indices, where only certain wavelengths could propagate through the system [13]. A century later, in 1987, Eli Yablonovitch [14] and Sajeev John [15] independently proposed, for the first time, the construction of a three-dimensional photonic crystal.

Photonic crystals are useful in the manufacturing of high-reflectance mirrors, the generation of nonlinear optical effects, the guidance of electromagnetic radiation in a circuit, among other applications ([16] and [17]). Ultimately, all these efforts lead to the fabrication of photonic devices aimed at advancing various modern technological disciplines, such as photonic computing [16].

The physical space where the structure of the photonic crystal is situated is known as the direct space and is characterized by the vectors a_i, which form a basis. When a Fourier transformation is performed on a function defined in the direct space, it is represented in the reciprocal space. The reciprocal space is the space of moments K, and the region where one typically works is known as the first Brillouin zone, which is uniquely associated with the primitive cell corresponding to the reciprocal lattice ([16] and [12]). The concept of the Brillouin zone was developed throughout the 20th century by Léon Brillouin, a French physicist. Additionally, the first Brillouin zone can be bounded to a minimum region known as the irreducible Brillouin zone by considering all symmetry groups present in the lattice while maintaining the origin of the cell ([11]). Below are the properties that the bases of both spaces must fulfill:

$$a^i \cdot a_j = 2\pi\delta^i_j, \qquad \mathbf{K} = \mathbf{K}_b + 2\pi\mathbf{p}. \tag{1.33}$$

For a photonic crystal fiber, its dielectric function can be defined periodically as a step function and then expanded into Fourier series to work in reciprocal space. The dielectric function is bounded by ϵ_1 and ϵ_2, representing the extreme values within the interval defined by the constants a and b, which are associated with the hole pitch (Λ) and hole diameter (d) of the PCF microstructure ([16] and [12]). The following equations illustrate this:

$$\epsilon(r) = \epsilon_1 + (\epsilon_2 - \epsilon_1)\ h(\tfrac{a}{2} - |r|), \tag{1.34}$$

$$-\varepsilon^{-1}(\mathbf{y}) = \textstyle\sum_{\mathbf{G}} \widehat{\varepsilon^{-1}}(\mathbf{G}) e^{i\mathbf{G}\cdot\mathbf{y}}, \tag{1.35}$$

$$\widehat{\varepsilon^{-1}}(\mathbf{G}) = \tfrac{1}{\varepsilon_1} f + \tfrac{1}{\varepsilon_2}(1-f)\delta_G^0 + \left[\tfrac{1}{\varepsilon_1} - \tfrac{1}{\varepsilon_2}\right] f \tfrac{2J_1(\|\mathbf{G}\|R)}{\|\mathbf{G}\|R}(1-\delta_G^0). \tag{1.36}$$

Where $f = \pi R^2/a^2$ is the filling fraction, and J_1 is the Bessel function of the first kind. On the other hand, the Helmholtz equation obtained from the Maxwell equations can be represented as an eigenvalue problem of the form ([16] and [17]):

$$\mathcal{L}(\mathcal{W}(u)) = E\mathcal{W}(u), \tag{1.37}$$

$$u(y) = (2\pi)^{-N/2} \textstyle\int_{\mathbb{R}^N} \widehat{u}(\mathbf{K}) e^{i\mathbf{K}\cdot\mathbf{y}} d\mathbf{K}. \tag{1.38}$$

$$u_{\mathbf{p}}(\mathbf{K}_b, \mathbf{y}) = exp(i\mathbf{K}_b \cdot \mathbf{y})\phi_{\mathbf{p}}(\mathbf{K}_b, \mathbf{y}), \tag{1.39}$$

$$u_{\mathbf{p}}(\mathbf{K}_b, \mathbf{y} + \mathbf{T}) = exp(i\mathbf{K}_b \cdot \mathbf{T}) u_{\mathbf{p}}(\mathbf{K}_b, \mathbf{y}). \tag{1.40}$$

Where the operator $\mathcal{L}$ acting on the Wannier transformation has, as its eigenfunctions, the Bloch functions u, which are quasiperiodic. Now, any square-integrable function (u) in $\mathbb{R}^N$ can be mapped to a family of pseudoperiodic functions defined by $\mathbf{K}$, denoted as $\mathcal{W}(u)$ ([16] and [17]). The operator $\mathcal{L}$ has a set of quasiperiodic eigenfunctions that form a Hilbert basis, known as Bloch waves ([16] and [17]). Then, for the TM polarization case, it takes the form $-\varepsilon(\mathbf{y})^{-1}\Delta$, and for the TE polarization case, it takes the form $-\text{div}(\varepsilon(\mathbf{y})^{-1}\mathbf{grad}(\cdot))$ as shown below:

$$-\varepsilon^{-1}(\mathbf{y})\ \Delta E_z = \left(\frac{w}{c}\right)^2 E_z, \tag{1.41}$$

$$-div(\varepsilon^{-1}(\mathbf{y})\ \mathbf{grad}(H_z)) = \left(\frac{w}{c}\right)^2 H_z. \tag{1.42}$$

Finally, the electric and magnetic fields, after being substituted into their series representations, generate the following differential equations:

$$E_z(\mathbf{K},\mathbf{y}) = \sum_{\mathbf{G}} \widehat{E}(\mathbf{K},\mathbf{G}) e^{i(\mathbf{G}+\mathbf{K})\cdot\mathbf{y}}, \tag{1.43}$$

$$H_z(\mathbf{K},\mathbf{y}) = \sum_{\mathbf{G}} \widehat{H}(\mathbf{K},\mathbf{G}) e^{i(\mathbf{G}+\mathbf{K})\cdot\mathbf{y}}. \tag{1.44}$$

$$\sum_{\mathbf{G}'} (\mathbf{K}+\mathbf{G})\cdot(\mathbf{K}+\mathbf{G}')\widehat{\varepsilon^{-1}}(\mathbf{G}-\mathbf{G}')\widehat{H}(\mathbf{K},\mathbf{G}') = \left(\tfrac{w}{c}\right)^2 \widehat{H}(\mathbf{K},\mathbf{G}) \tag{1.45}$$

$$\sum_{\mathbf{G}'} (\mathbf{K}+\mathbf{G}')^2 \widehat{\varepsilon^{-1}}(\mathbf{G}-\mathbf{G}')\widehat{E}(\mathbf{K},\mathbf{G}') = \left(\tfrac{w}{c}\right)^2 \widehat{E}(\mathbf{K},\mathbf{G}). \tag{1.46}$$

When brought into matrix form, it defines an eigenvalue problem for the electric field and its allowed propagation modes in terms of energy, according to the dielectric operator defined for a PCF whose microstructure has rotational symmetry and lies in the plane transverse to the propagation axis ([16] and [17]).

On the other hand, it is possible to approximate the waveguiding behavior of a PCF to the ordinary waveguiding mechanism of a standard optical fiber through the appropriate use of values associated with the two refractive indices corresponding to the core and cladding [18]. This is schematically illustrated below.

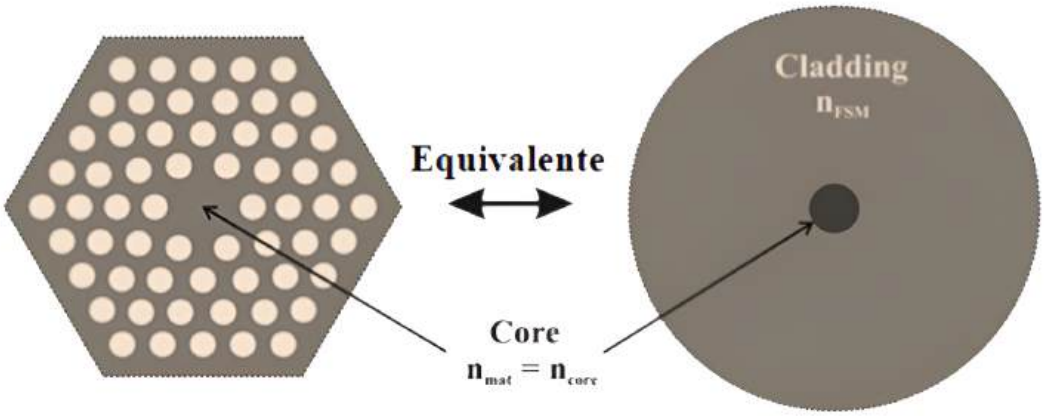

Figure 1.4: Equivalence approximation between a PCF and a standard optical fiber [8].

In this equivalence, the refractive index of the material used in the PCF core is equated with the index of the new standard optical fiber's core. The effective refractive index corresponding to the filling factor $\frac{d}{\Lambda}$ is equated with the refractive index n_{FSM} associated with the cladding of the new standard optical fiber.

1.4 Types of PCFs

Photonic Crystal Fibers (PCFs) can be classified into two types, depending on the principle under which the guidance of electromagnetic radiation occurs. Thus, in the first instance, there are PCFs whose effective refractive index allows the necessary condition for total internal reflection. In the second instance, there are PCFs whose guiding principle is based on the Photonic Band Gap (PBG) effect.

Now, within these two groups, there are further sub-classifications that correspond to the specific dimensions and shape of the microstructure, determining specific properties. This classification is shown in Figure 1.5.

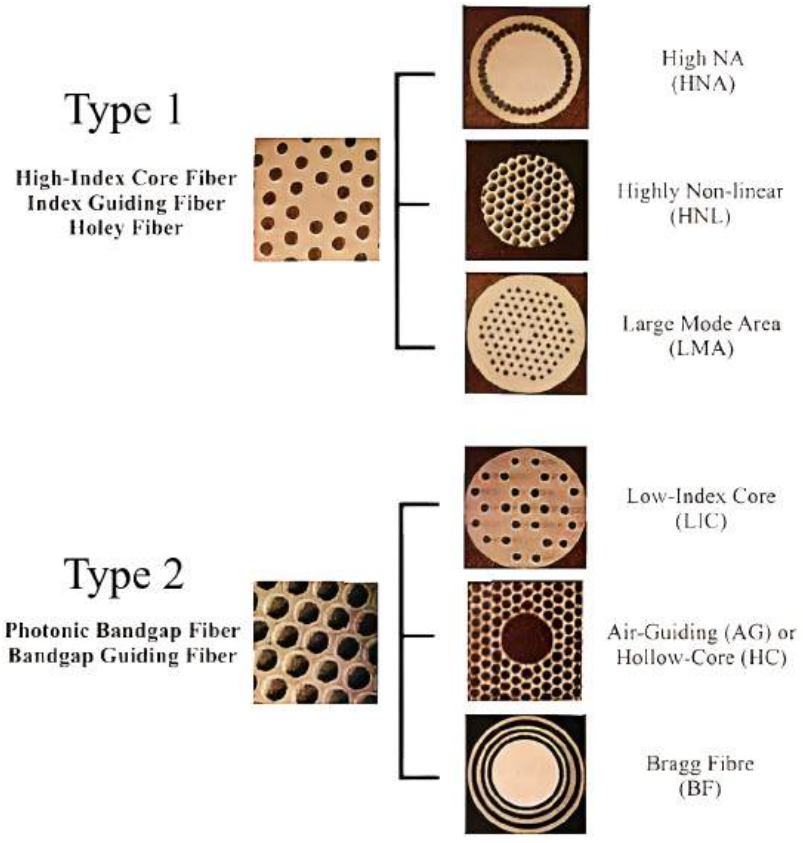

Figure 1.5: Classification of photonic crystal fibers according to their microstructures and properties [8].

Bibliography

[1] K. Thyagarajan Ajoy Ghatak. *Introduction to fiber optics.* Cambridge University Press, 1998.

[2] John A. Buck. *Fundamentals of optical fibers, second edition.* John Wiley Sons, 2004.

[3] Masanori KOSHIBA. *Optical waveguide theory by the finite element method.* KTK Scientific Publishers,, 1992.

[4] Allen H. Cherin. *An introduction to optical fibers.* McGraw-Hill, 1983.

[5] André N. Boris K. Sébastien G. Didier F. Alexander A. Sergio L. Fréderic Z., Gilles R. *Foundations of photonic crystal fibres, 2nd edition.* Imperial College Press, 2012.

[6] Maurice O'Sullivan Rongqing Hui. *Fiber optics measurement techniques.* Elsevier, Academic Press., 2009.

[7] Fundación Wikipedia. *Modo Transversal Electromagnético.* Estraído de: https://es.wikipedia.org/wiki/Modo_transversal_electromagnético, Consultado en Diciembre de 2019.

[8] Carlos Porras. *Design, fabrication and characterization of nonlinear photonic crystal fibers for telecommunication wavelength range and for near infrared wavelength supercontinuum light sources.* Tesis de Maestría, Centro de Investigaciones en Óptica., 2017.

[9] Masanori Koshiba Kunimasa Saitoh. *Empirical relations for simple design of photonic crystal fibers.* Optical Society of America, Optics Express, Vol. 13, No. 1, pp. 267-274, 2005.

[10] Kunimasa S. Masanori K. *Applicability of classical optical fiber theories to holey fibers.* Optics Letters, Vol. 29, No. 15, pp. 1739-1741, 2004.

[11] Norberto Arzate Plata L. A. Padilla Salas. *Cristales Fotónicos.* Artículos de divulgación, Explorando en la Óptica, Academia Mexicana de Óptica, 2014.

[12] L. J. Martínez J. Sánchez P. A. Postigo, A. R. Alija. *Fabricación y caracterización de cristales fotónicos bidimensionales para nuevos dispositivos optoelectrónicos.* Sociedad Española de Óptica, Opt. Pura Apl., Vol. 39, no. 2, pp. 185-188, 2006.

[13] Lord Rayleigh. *On the maintenance of vibrations by forces of double frequency, and on the propagation of waves through a medium endowed with periodic structure.* Philosophical Magazine and Journal of Science, Vol. 24, no. 147, pp. 145-159, 1887.

[14] E. Yablonovitch. *Inhibited Spontaneous Emission in Solid-State Physics and Electronics.* Phys. Rev. Lett. Vol. 58, no. 20, pp. 2059-2062, 1987.

[15] J. Sajeev. *Strong Localization of Photons in Certain Disordered Dielectric Superlattices.* Phys. Rev. Lett. Vol. 58, no. 23, pp. 2486-2489, 1987.

[16] R. B. Wehrspohn K. Busch, S. Lolkes and H. Foll. *Photonic Crystals, advances in design, fabrication, and characterization.* WILEY-VCH Verlag GmbH Co. KGaA, Weinheim, 2004.

[17] David Hernández García. *Estudio de cristales y cuasicristales fotónicos basados en silicio macroporoso.* Universitat Politècnica de Catalunya.

[18] P. St. J. Russell D. M. Atkin J. C. Knight, T. A. Birks. *All-silica single-mode optical fiber with photonic crystal cladding.* Optics Letters, Vol. 21, No. 19, pp. 1547-1549, 1996.

Chapter 2

Lossy Mode Resonance in PCFs

2.1 Design of the Device

In the previous chapters, the optical characteristics associated with cylindrical waveguides or optical fibers have been described. These properties allow us to predict the behavior of the modes that a fiber optic system can support based on the materials and dimensions of each of its parts. This fact is important to employ an appropriate mechanism in the generation of the Lossy Mode Resonance (LMR) phenomenon, as it mainly occurs due to the migration of loss modes from the fundamental mode in the spectral region where a coating with suitable optical properties can support the propagation of these modes, generating resonance.

As mentioned earlier in the introduction, conventional optical fibers need to be modified to shorten the distance between the evanescent fields of both the modes traveling through the coating and those migrating from the core. For this purpose, a part of the fiber is usually removed in a cut called D, exposing the fiber core to facilitate energy exchange with a coating that occupies the removed section, allowing the formation of the LMR phenomenon. Fiber optics for physical and chemical sensors using LMR have been intensively investigated for conventional fibers [1] y [2].

We have designed a photonic crystal optical fiber device that avoids such modification and allows greater control over the losses of the fundamental mode depending on the microstructure of the fiber. In this design, a simple taper or even just placing the coating on the outside of the fiber is sufficient to obtain the LMR phenomenon.

This design is based on the information presented in the second chapter, where it is clearly shown how it is possible to modify the optical properties of an optical fiber based on its microstructure. In this case, we can directly define a microstructure that promotes the propagation of the fundamental mode in the outer region by increasing the diameter of the fundamental mode and reducing the number of rings in the fiber to favor its migration towards the boundaries where it encounters the coating. All of this synergistically combines to achieve greater efficiency in generating the LMR phenomenon.

Next, we present the design of the device in question:

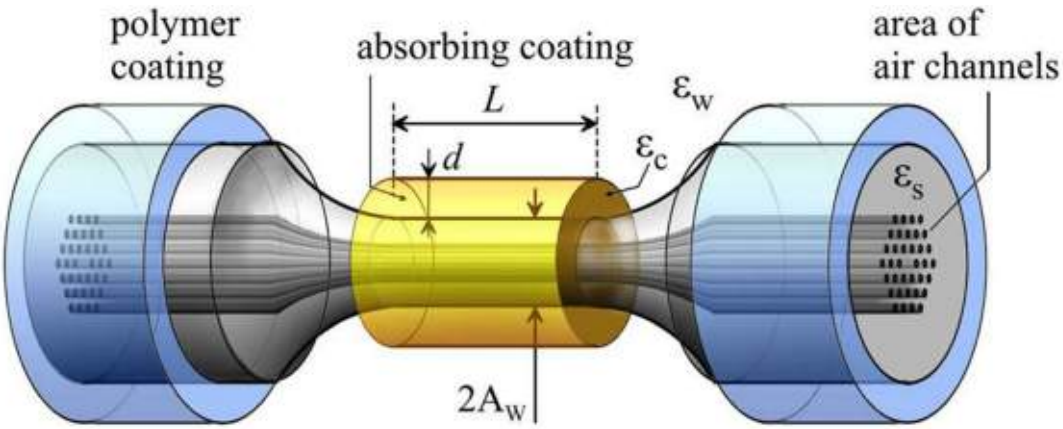

Figure 2.1: An adiabatic taper of the PCF with three hexagonal rings of air channels and an absorbing coating of length L and thickness d around the taper waist of diameter $2A_W$

In the figure 2.1, a photonic crystal fiber with 3 rings and a triangular hexagonal structure can be observed. A taper is applied to this PCF, and subsequently, a coating is placed on it. This device enables the formation of the LMR phenomenon, as will be seen below.

We explore another theoretical approach to achieve Loss Mode Resonance (LMR), facilitated by a specialized photonic crystal fiber (PCF) [3]. When the PCF is composed of a finite number of air channels within a dielectric matrix, the propagation constants of PCF modes are typically lower than the refractive index of the matrix [3, 4]. Consequently, in an unbounded matrix, the fields of these modes leak from the fiber core, resulting in confinement losses [3, 4]. In practical PCFs with bounded claddings and absorbing film coatings, these leaky modes can only be phase-matched with the leaky ones of the film coatings.

The coupling of leaky modes from different waveguides can occur at a significant distance between the waveguides. This phenomenon allows the realization of LMR through the coupling between modes of a PCF core and modes of an absorbing film coating applied directly to the outer surface of the fiber cladding, without the need for local modification of the cladding [5]. Given the current state of technology, where PCFs can be easily fabricated as single-mode [3], this approach offers the advantages of enabling single-mode operation for sensors and almost completely eliminating diffraction losses at irregularities in the PCF.

The investigation of LMR in PCFs was initially explored in [5], providing an interpretation of the experimentally observed quasi-periodic transmission spectrum of a regular PCF with an absorbing polymer coating. The aim of this work is to evaluate the features of using LMR in PCFs for sensing applications. Numerical estimates are presented for both modal properties of PCFs with absorbing coatings and transmission spectra of PCFs in sensing refractive index of a liquid, pressure in the liquid, and an adsorption nanoscale layer. The modeling is conducted using the method of integral equations [5], a full vectorial mode solver formulated with respect to the transverse components of the magnetic field within a PCF. This method allows for a rigorous calculation of the fields and propagation constants of guided and leaky modes of PCFs with layered coatings.

2.2 Condition in PCF to get LMR.

To investigate regular and adiabatically tapered Photonic Crystal Fibers (PCFs) with absorbing coatings, we conduct calculations involving the time factor $e^{i\omega t}$. The specific PCF utilized in our computations comprises a solid core surrounded by three rings of air channels arranged in a hexagonal pattern. The material of the PCF is quartz glass, with its refractive index n_s assumed to be real and described by the well-known three-term Sellmeier formula [6]. The parameters for the untapered PCF are as follows: cladding diameter $D_0 = 123.4\,\mu m$, diameter of the air holes $a_0 = 3\,\mu m$, and photonic crystal pitch $\Lambda_0 = 8.8\,\mu m$ [7].

The structure of the adiabatically tapered PCF is illustrated in Figure 2.1. During the taper fabrication process, the diameter of the holes (a) and the pitch (Λ) within the taper waist are adjusted according to the rule [8]: $a = \left(\frac{2Aw}{D_0}\right) a_0$, $\Lambda = \left(\frac{2Aw}{D_0}\right) \Lambda_0$. For the taper calculations, we adopt $2Aw = 44\,\mu m$ and $L = 3\,cm$ as values (see Figure 2.1); the chosen parameter values correspond to single-mode PCFs [3, 7]. Consequently, in the subsequent analysis, PCF modes are referred to as the fundamental modes of the PCF.

We will examine two categories of PCF modes: the first type comprises leaky modes of PCFs with an infinite cladding, denoted as PCF core modes. The second type includes modes of a PCF with a bounded cladding and an absorbing coating, referred to simply as PCF modes. Modes of the first and second types exhibit distinct imaginary parts of the propagation constants. However, they have nearly identical real parts of the propagation constants and transverse field distributions within the PCF core [5].

Figure 2.2 shows the modal dispersion $\beta(\lambda)$ for the untapered Photonic Crystal Fiber (PCF) with $2Aw = D0$. Here, β represents the dimensionless complex propagation constants of PCF modes, encompassing both types and modes of the absorbing film coating, while λ denotes the light wavelength.

The PCF is envisioned to be coated with multifunctional butyl acrylate polymer, characterized by a complex refractive index $n_c = 1.54 - i0.00002$, situated below the polymer coating. The PCF is surrounded by water ($\varepsilon_w = n_w^2$, $n_w = 1.33$, see Fig. 2.1).

In the context of Fig. 2.2a, the term 'Loss' is defined as $4\pi \times 10^7 |\mathrm{Im}\beta|/(\lambda \ln 10)$, where $\mathrm{Im}\beta$ represents the imaginary part of the propagation constant of the PCF mode.

Figure 2.2b elucidates spectral dependencies, encompassing the refractive index for quartz glass, the complex propagation constants of the PCF core mode, and the modes of the absorbing coating. This presentation aids in qualitatively explaining the non-monotonic character of the dependence shown in Fig. 2.2a.

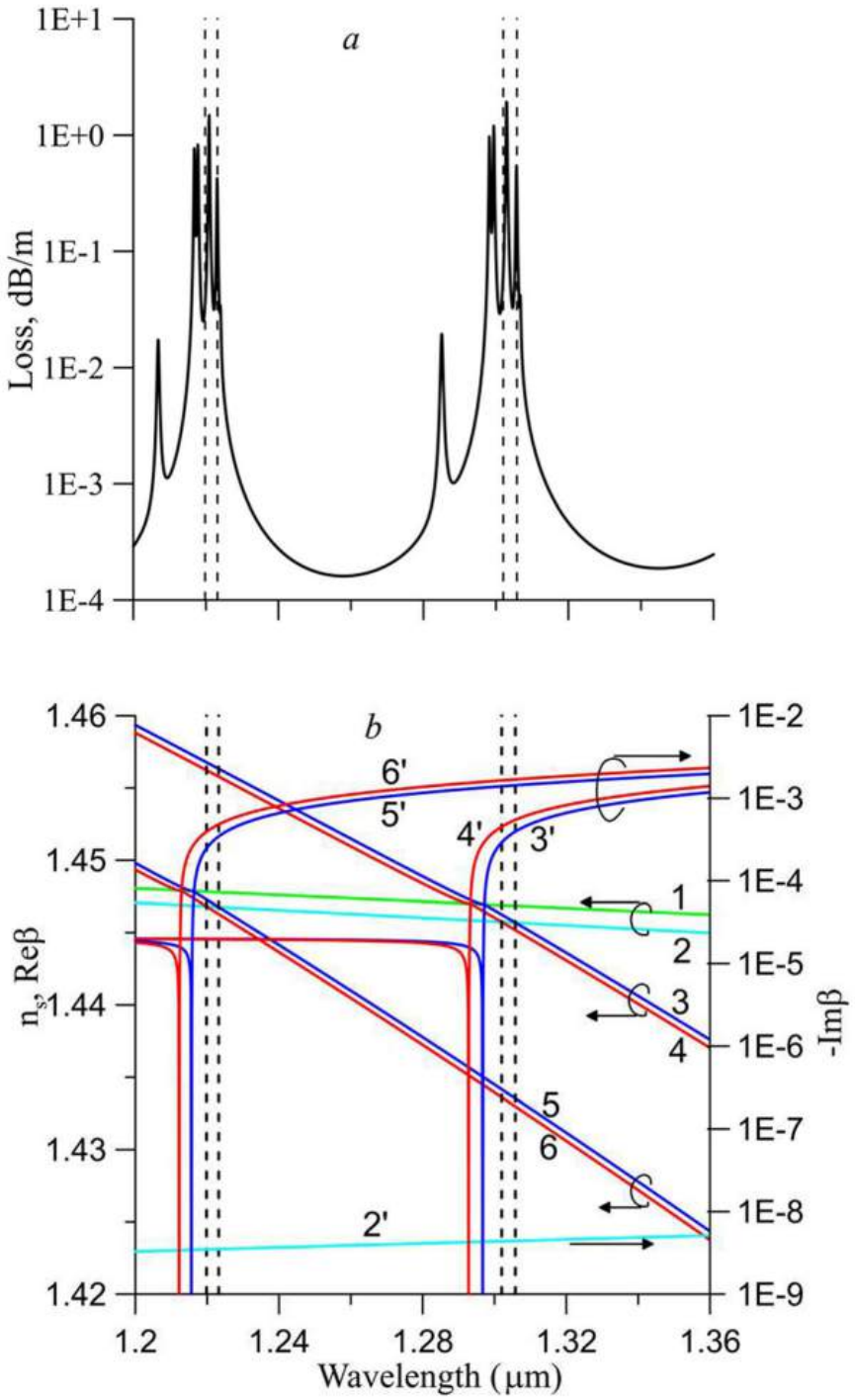

Figure 2.2: Spectral dependencies of mode propagation constants for an untapered PCF with a polymer coating of thickness $d = 20\mu m$, surrounded by water. (a) Loss of the PCF mode, (b) Phase diagram. Curve 1: Quartz glass refractive index. Curves 2 and 2' represent Re(β) and Im(β) of the PCF core mode. Curves 3 and 3', 5 and 5' depict Re(β) and Im(β) of TE modes of different orders for the coating. Curves 4 and 4', 6 and 6' show Re(β) and Im(β) of TM modes of the same orders for the coating. Dashed lines indicate wavelengths of phase synchronism of the PCF core and coating modes, corresponding to intersection points of curves 3, 4, 5, and 6 with curve 2.

The PCF core mode was calculated on the assumption that $\varepsilon_w = \varepsilon_c = \varepsilon_s = n_s^2$. According to Fig. 2.2b, for this mode, $\mathrm{Re}(\beta) < n_s$; that is, it leaks from the PCF core. At the same time, as $\mathrm{Re}(\beta) > n_w$, the PCF mode field experiences total internal reflection at the outer boundary of the PCF coating. Therefore, and also since $\mathrm{Im}n_s = 0$, loss of the PCF mode in Fig. 2.2a is entirely caused by dissipation of its energy in the coating. The corresponding solid curve in Fig. 2.2a and curves 2, 2' in Fig. 2.2b are computed through the method of integral equations [5]. Curves 3–6 and 3 – 6 in Fig. 2.2b are the results of a numerical solution by means of the contour integration method [9] of the dispersion equation for modes of a planar dielectric waveguide [10].

$$\Big[\frac{\gamma_w}{\sigma}\Big(\frac{\varepsilon_c}{\varepsilon_w}^T - \frac{\sigma}{i\gamma_s}\left(\frac{\varepsilon_s}{\varepsilon_c}\right)^T sin(k_0\sigma d) + \left[1 + \frac{\sigma}{i\gamma_s}\left(\frac{\varepsilon_s}{\varepsilon_c}\right)^T\right] cos(k_0\sigma d) = 0,$$
$$\text{where } T = \begin{cases} 0, & \text{for TE modes,} \\ 1, & \text{for TM modes,} \end{cases} \quad \text{and each constant is:} \tag{2.1}$$

$$\gamma_w = \sqrt{\beta^2 - \varepsilon_w} \quad (\mathrm{Re}(\gamma_w) \geq 0), \quad \gamma_s = \sqrt{\varepsilon_s - \beta^2} \quad (\varepsilon_s = n_s^2, \mathrm{Re}(\gamma_s) \geq 0),$$
$$\sigma = \sqrt{\varepsilon_c - \beta^2} \quad (\varepsilon_c = n_c^2, \mathrm{Re}(\sigma) \geq 0) \quad \text{and} \quad k_0 = \frac{2\pi}{\lambda}, \tag{2.2}$$

Modeling the absorbing coating of thickness d. These curves are computed based on the reasons that, from the point of view of the ray optics, the fundamental mode of the PCF is mainly formed by meridional rays [5]. When considering a reflection of such rays from the coating, the latter can be approximately replaced by a planar-parallel layer of thickness d. In this approximation, the coating modes should be understood as the modes of the planar dielectric waveguide. Due to the hybrid polarization of the PCF core mode, it can be coupled with both TE and TM modes of the coating [5].

2.3 Dependence of LMR Modes Due to Variations in Sensor Parameters

In Fig. 2.2b, segments of curves 3–6 located above curve 1 correspond to guided modes of the planar dielectric waveguide, and those below curve 1 correspond to leaky modes of the waveguide. The transition in the mode type from guided to leaky occurs as the wavelength increases [10]. At the moment of this transition at the critical wavelength $\lambda = \lambda_c$, the mode propagation constant β coincides with the refractive index of the quartz glass, n_s. In this case, $-\mathrm{Im}(\beta)$ reaches its minimum. As the difference $\lambda - \lambda_c$ grows, the value of $-\mathrm{Im}(\beta)$ increases sharply due to the leakage effect (see Fig. 2.2b).

At the same time, curve 2 passes everywhere below curve 1 in Fig. 2.2b; so, the PCF core mode is always leaky. As a result, this mode can be phase matched with only leaky modes of the coating at resonance wavelengths indicated in Fig. 2.2 by vertical dashed lines (at these wavelengths, real parts of the propagation constants of the modes coincide); in Fig. 2.2a, the loss of the PCF mode sharply grows in the vicinity of these wavelengths. As observed in Fig. 2.2a, a quasi-periodic spectrum of the PCF mode loss can be explained by the resonance coupling of the PCF core mode with leaky modes of the absorbing coating [5]. This coupling leads to a resonance capture of the PCF mode energy by the coating, and to the release of heat in it.

It should be noted that there is a large difference of about 5 orders of magnitude between the imaginary parts of the propagation constants of the PCF core mode and the absorbing coating modes in the vicinity of the resonance wavelength in Fig. 2.2b. This mismatch of propagation constants negatively affects the coupling noted. Since the attenuation of the coating modes sharply decreases with decreasing wavelength (see Fig. 2.2b), it causes a left shift of the centers of gravity of the attenuation peaks relative to the dashed lines in Fig. 2.2a. This shift increases with an increase in attenuation of the coating modes (see below).

Note also that the simple qualitative coupling model described does not allow us to fully explain the complex multi-peak loss dependence (λ) in Fig. 2.2a.

When using untapered PCFs, the mentioned coupling of leaky modes can be rather weak. As a result, it can only be observed when sufficiently long pieces (of the order of meters) of coated untapered PCFs are used (this conclusion follows from Fig. 2.2a). Besides, to realize the LMR, it is necessary to keep the coating thickness d constant along the entire sensitive piece of the PCF, with a tolerance of $0.075\lambda/\sqrt{n_c^2 - n_s^2}$ [5]. For long PCF pieces and thick coatings, this requirement is difficult enough to fulfill. It is suggested that the use of thinner coatings (less than $20\mu m$) and adiabatic PCF tapers with a length of a sensitive region (taper waist) of the order of centimeters will overcome these difficulties.

Figures 2.3 and 2.4 illustrate the modal characteristics of both untapered and tapered PCFs, both coated with the same $5\mu m$-thick polymer coating. These figures follow a similar format to Figure 2.2, but show that as the coating thickness (denoted as 'd') decreases, the spectral intervals between the dispersion curves of the coating modes widen [5]. Consequently, in the spectral range covered by Figures 2.3 and 2.4, only two coating modes (one TE and one TM) can be resonantly coupled with the PCF core modes.

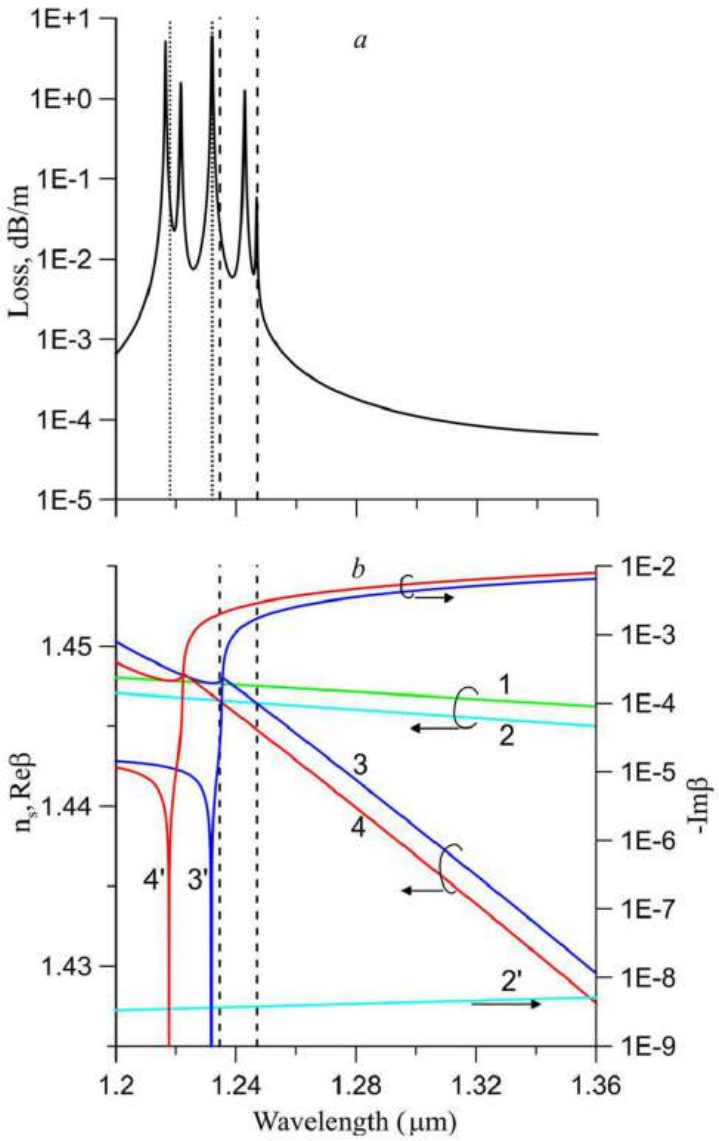

Figure 2.3: Spectral dependencies of mode propagation constants for an untapered PCF with a polymer coating of thickness $d = 5\mu m$, surrounded by water. (a) Loss of the PCF mode, (b) Phase diagram. Curve 1: Quartz glass refractive index. Curves 2 and 2' represent Re(β) and Im(β) of the PCF core mode. Curves 3 and 3', 5 and 5' depict Re(β) and Im(β) of TE modes of different orders for the coating. Curves 4 and 4', 6 and 6' show Re(β) and Im(β) of TM modes of the same orders for the coating. Dashed lines indicate wavelengths of phase synchronism of the PCF core and coating modes, corresponding to intersection points of curves 3, 4, 5, and 6 with curve 2. Dotted lines refer to minima of $|\beta - \beta_{TM}|$ (left line) and $|\beta - \beta_{TE}|$ (right line)

In Figure 2.3, the resonance wavelengths are concentrated around $\lambda = 1.24\mu m$. As evident from Figure 2.3a, the peak attenuation of the untapered PCF mode remains comparable to that in Figure 2.2a. This implies that it is predominantly determined by the confinement losses of the PCF core mode, which remain consistent

in both cases. However, in the proximity of the resonance wavelengths, the values of $-Im\{\beta\}$ in Figure 2.3b are roughly three times higher than the corresponding values in Figure 2.2b. This phenomenon demonstrates that reducing the coating thickness exacerbates the mismatch between the complex propagation constants of the PCF core mode and the coating modes. This, in turn, leads to a more pronounced leftward shift of the centers of gravity of the attenuation peaks relative to the dashed lines in Figure 2.3a compared to the analogous shift in Figure 2.2a.

To quantitatively explain this shift, we have calculated the wavelengths corresponding to the minima of the module $|\beta - \beta_{TE}|$ and $|\beta - \beta_{TM}|$ using the phase diagram depicted in Figure 2.3b. These wavelengths are marked in Figure 2.3a by dotted lines, with the left of the lines indicating min $|\beta - \beta_{TM}|$ and the right indicating min $|\beta - \beta_{TE}|$. As observed, they align well with the primary loss peaks.

To enhance the coupling between the PCF core and coating modes and, consequently, the attenuation of the PCF mode, an adiabatic PCF taper can be employed, as shown in Figure 2.4. According to Figures 2.3a and 2.4a, such a device permits a more significant influence of the absorbing coating on PCF transmission. Specifically, in Figure 2.4a, the peak of the loss dependence (λ) is an order of magnitude higher than the corresponding peak in Figure 3a. This allows for a one-order-of-magnitude reduction in the length of the fiber segment exhibiting the LMR. However, in accordance with Figures 2.3b and 2.4b, the transition to a tapered PCF results in a decrease in $Re\{\beta\}$ and an increase in $-Im\{\beta\}$ of the PCF core mode, leading to a further misalignment of the complex propagation constants of the PCF core mode and the coating modes. Consequently, the aforementioned simple coupled mode model cannot fully elucidate the transmission properties of the adiabatically tapered PCF.

In fact, in Figure 2.4a, two distinct loss peaks, located close to the resonant wavelengths $\lambda = 1.285\mu m$ and $\lambda = 1.299\mu m$, exhibit significant shifts in relation to these wavelengths. Dotted lines in Figure 2.4a, which have a similar significance as in Figure 2.3a, provide a better match with these peaks but do not align perfectly

with the peaks in detail. Additionally, alongside these sharp peaks, several broader attenuation peaks are noticeable. These additional peaks are attributed to the resonance coupling of the PCF core mode with modes of the PCF cladding concentrated in the region between air channels and the absorbing coating [8]. As a result, these cladding modes effectively interact with the coating.

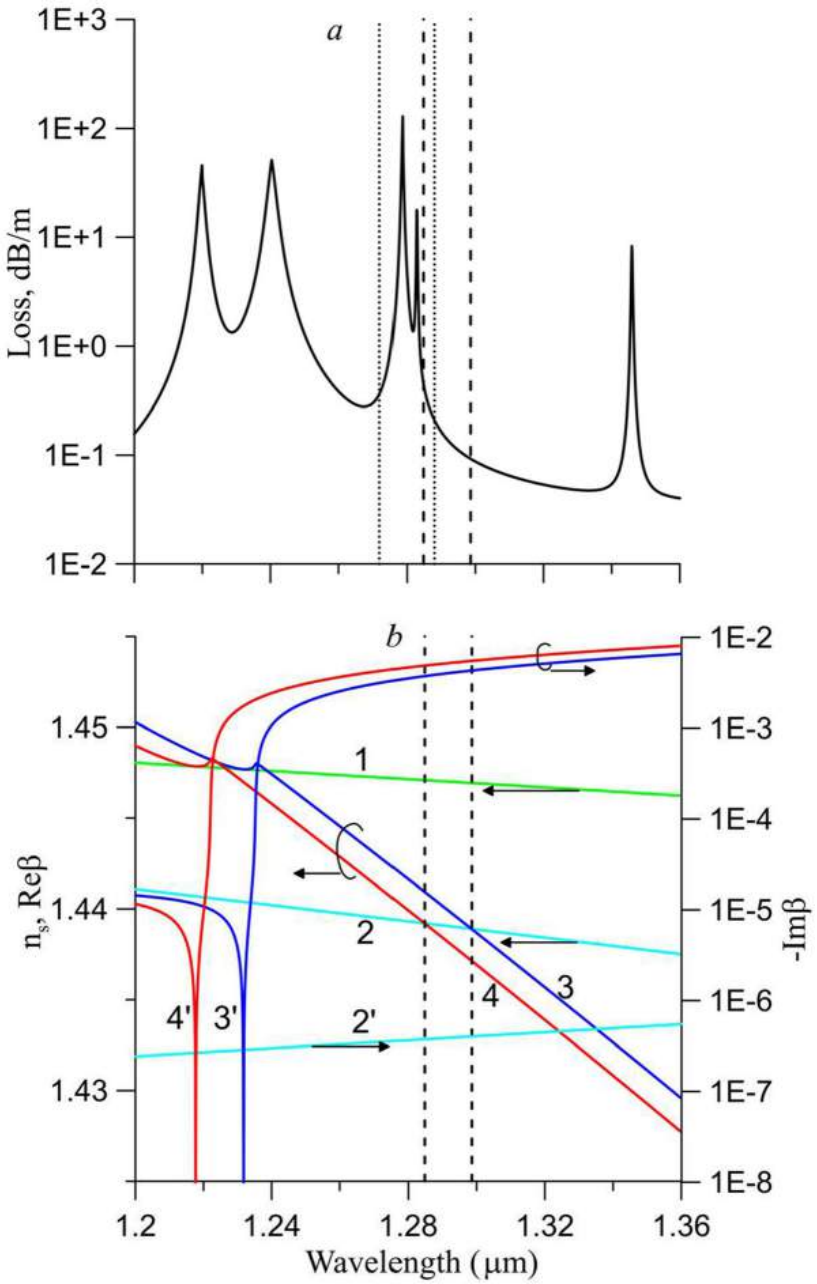

Figure 2.4: Spectral dependencies of mode propagation constants for the tapered PCF with a polymer coating of thickness $d = 5\mu m$, surrounded by water. (a) Loss of the PCF mode, (b) Phase diagram. Curve 1: Quartz glass refractive index. Curves 2 and 2' represent Re(β) and Im(β) of the PCF core mode. Curves 3 and 3', 5 and 5' depict Re(β) and Im(β) of TE modes of different orders for the coating. Curves 4 and 4', 6 and 6' show Re(β) and Im(β) of TM modes of the same orders for the coating. Dashed lines indicate wavelengths of phase synchronism of the PCF core and coating modes, corresponding to intersection points of curves 3, 4, 5, and 6 with curve 2. Dotted lines refer to minima of $|\beta - \beta_{TM}|$ (left line) and $|\beta - \beta_{TE}|$ (right line)

The losses observed in Figures 2.5a and b, occurring at the wavelengths $\lambda = 1.244\mu m$ and $\lambda = 1.279\mu m$, are attributed to the direct coupling between the tapered

PCF mode and the absorbing coating, as illustrated in Figure 2.4.

This association is affirmed by examining Figures 2.5 and 2.6, which compare the normalized intensity distributions $S_z(x, y)/S_zmax$ for the tapered PCF mode across different wavelengths. Here, $S_z(x, y)$ represents the z-component of the Poynting vector of the PCF mode field, where the $0Z$ axis aligns with the PCF.

It's important to note that, on the linear scale of $S_z(x, y)/S_zmax$ displayed in Figure 2.5, except for a narrow vicinity around the wavelength $\lambda = 1.244\mu m$, the optical density distributions for the PCF mode across the entire spectral range in Figure 2.4 visually overlap and resemble the pattern in Figure 2.5b. For more detailed information on the distribution of mode intensity at various wavelengths, Figure 2.6 presents distributions on a logarithmic scale (the orientation of the coordinate axes $0X$ and $0Y$ relative to the PCF cross-section is evident from Figure 2.5).

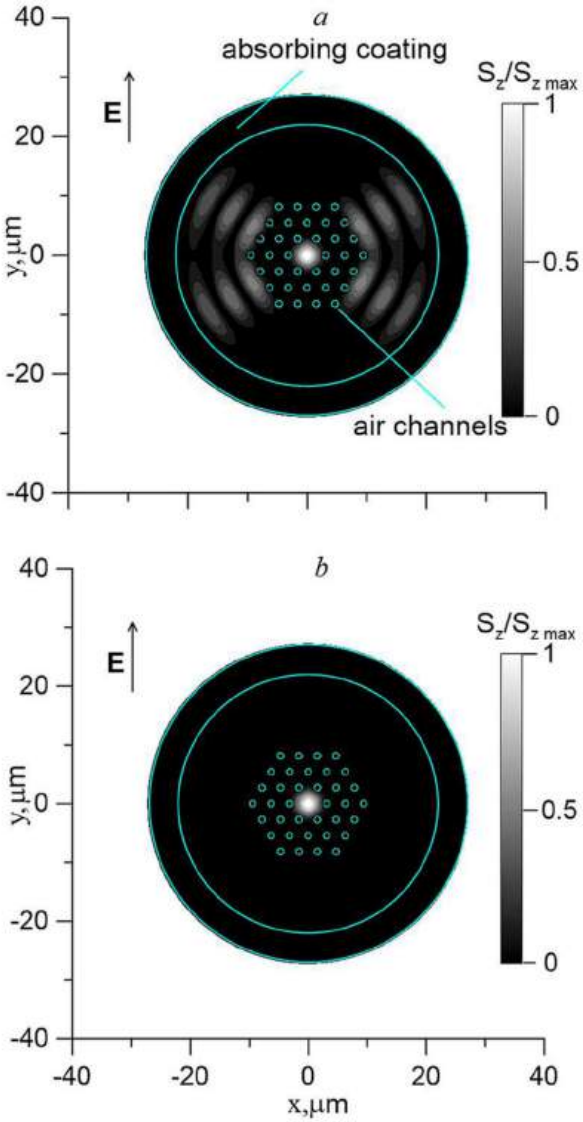

Figure 2.5: The optical densities of the fundamental mode in the tapered PCF are depicted for wavelengths $1.244\mu m$ (a) and $1.279\mu m$ (b). The arrows labeled "E" denote the primary orientation of the electric field vector of the PCF mode. The small circles represent cross-sections of the air channels encircling the PCF core.

Figures 2.6a and 2.6c offer detailed distributions of the mode intensities depicted in Figures 2.5a and 2.5b, respectively. Meanwhile, Figure 2.6b corresponds to the intermediate wavelength between the loss maxima shown in Figure 2.4a. As indicated in Figure 2.6, the peaks in mode losses at wavelengths $1.244\mu m$ and $1.279\mu m$ in Figure 2.4a are due to a relatively high normalized intensity of the PCF mode in the absorbing polymer coating. Specifically, the averaged intensities in Figures 2.6a

and 2.6b, delineated between dashed lines, are over 4 orders of magnitude higher compared to the similar intensity in Figure 2.6b.

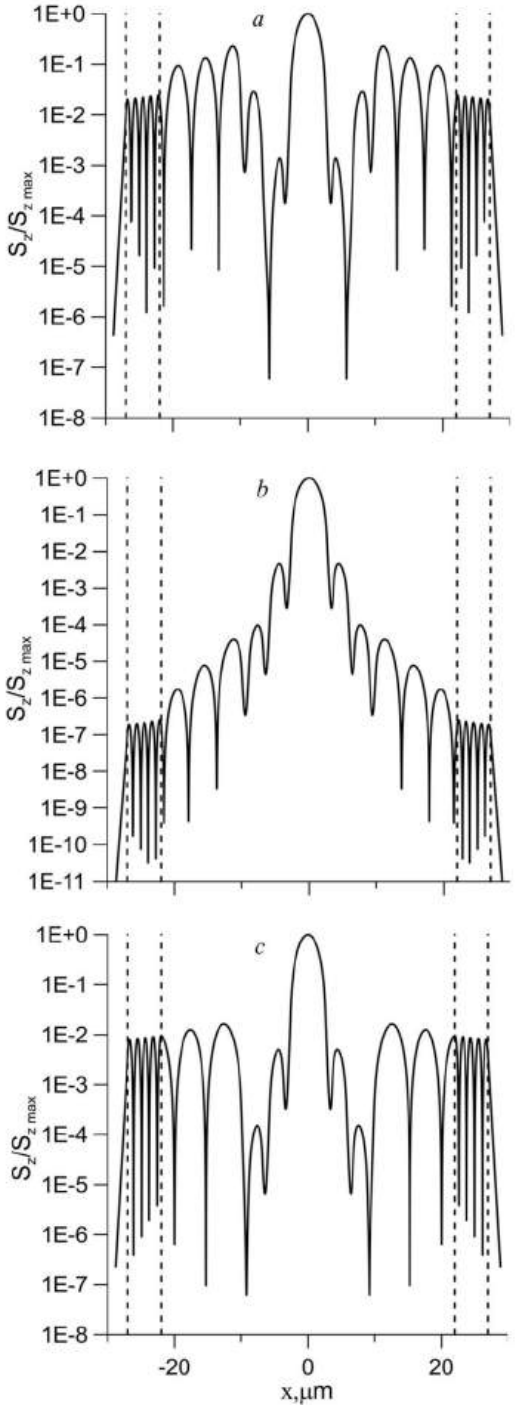

Figure 2.6: The intensity distributions of the fundamental mode in the tapered PCF, $S_z(x,0)/S_zmax$, are shown at wavelengths $1.244\mu m(a)$, $1.26\mu m(b)$, and $1.279\mu m(c)$. The dashed lines mark the boundaries of the polymer coating.

Furthermore, it is noteworthy that the optical field between the PCF core and the absorbing coating, seen in Figures 2.5a and 2.6, adopts the shape of standing waves, a natural occurrence owing to the coupling between the PCF core and PCF coating facilitated by propagating waves.

In summary, the intensity distributions presented in Figure 2.6 validate the link between the emergence of spectral peaks in PCF mode losses and the resonant capture of mode energy by the absorbing coating.

2.4 Calculation for sensing by LMR in PCF

Given the susceptibility of the modal characteristics of the PCF absorbing coating to environmental factors, alterations in environmental parameters induce a modulation in the propagation constants of leaky modes within the absorbing coating. This modulation, in conjunction with the coupling of these modes to the PCF mode, subsequently influences the fiber transmission near resonance wavelengths.

Figures 2.7 and 2.8 pertain to the adiabatic PCF taper coated with a polymer layer of thickness $d = 5\,\mu m$, surrounded by water, as previously examined. These figures demonstrate the utilization of the LMR associated with the direct coupling between the PCF mode and the leaky coating modes occurring close to $\lambda = 1.28\,\mu m$ (refer to Fig. 2.4a). Figure 2.7 showcases the application of the discussed PCF taper as a refractive index sensor for liquids, a potential application in bio-chemical sensing [11, 12].

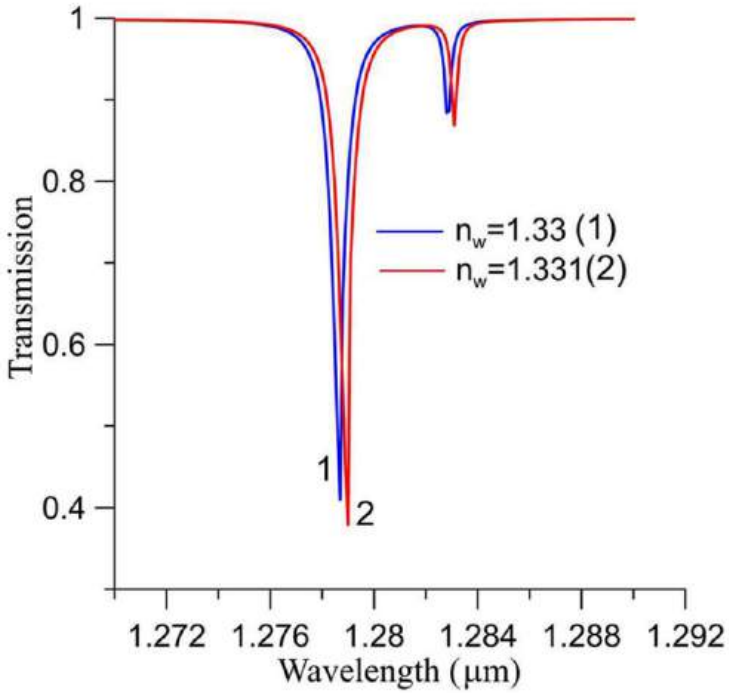

Figure 2.7: The change in the transmission spectrum of the adiabatic taper in the PCF, having a length of $L = 3$ cm and a polymer coating thickness of 5 μm, varies according to alterations in the refractive index within the surrounding liquid.

In this scenario, the efficacy of the sensor can be quantified by the sensitivity parameter $d\lambda_{\min}/dn_w$, where $d\lambda_{\min}$ denotes the shift in resonance wavelength corresponding to an infinitesimal increase in the refractive index of the environment (dn_w), and by a resonance spectral width ($\delta\lambda_{0.5}$), influencing the signal-to-noise ratio [13].

The interrelation of these parameters with the thickness of the polymer coating is presented in Table 1. Here, $\lambda_{\min}$ signifies the resonance wavelength, Transmission($\lambda_{\min}$) represents the corresponding PCF transmission at the initial environmental refractive index $n_w = 1.33$, and $\delta\lambda_{0.5}$ is the resonance spectral width calculated as $\delta\lambda_{0.5} = \lambda_2 - \lambda_1$, where λ_2 and λ_1 ($\lambda_2 > \lambda_1$) are the roots of the equation:

$$\text{Transmission}(\lambda) = 0.5\,[1 + \text{Transmission}(\lambda_{\min})]$$

The values for these parameters, derived for various thicknesses of the polymer film, are presented in Table 2.1. Comparative analysis suggests that in contrast to

multimode sensors employing an absorbing polymer coating directly applied to the silica fiber core [14], the considered devices exhibit lower sensitivity to alterations in the refractive index of the surrounding liquid. However, they display a more than tenfold decrease in the spectral width of resonances. Notably, unlike the refractive index sensors examined in [14], the sensitivity of the described PCF sensors diminishes as the thickness of the absorbing coating increases. These distinctions stem from the specific interaction between the leaky coating modes and the environment and the single-mode functionality of the sensor.

d, µm	λ_{min}, µm	Transmission (λ_{min})	$d\lambda_{min}/dn_w$, µm/RIU	$\delta\lambda_{0.5}$, µm
1.5	1.3073	0.65	0.81	$5.0 \cdot 10^{-4}$
5	1.2787	0.41	0.31	$4.5 \cdot 10^{-4}$
10	1.2538	0.89	0.10	$4.0 \cdot 10^{-4}$

Table 2.1: The adiabatically tapered PCF with a polymer coating can serve as a refractive index sensor. In this context, *RIU* stands for Refractive Index Unit.

Figure 2.8 exhibits the potential of utilizing the adiabatically tapered PCF with a polymer coating as a liquid pressure sensor. Such a sensor holds applicability in various domains such as petroleum pipelines, water conservancy, hydropower, and hydraulic machinery.

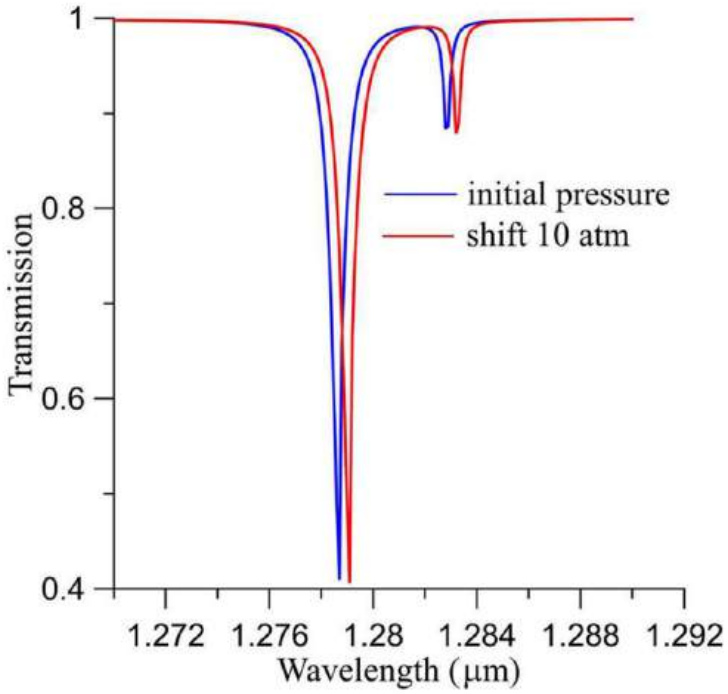

Figure 2.8: The modification in the transmission spectrum of the adiabatic taper in the PCF, featuring a length of $L = 3cm$ and a polymer coating with a thickness of $5\mu m$, is contingent upon fluctuations in pressure within the surrounding liquid.

In evaluating the pressure sensor, we considered that alterations in pressure lead to changes in the coating's thickness (Δd) and the photo elastic shift (Δn_c) of the coating's refractive index. Both these factors affect the propagation constants of the coating's leaky modes. In accordance with elasticity theory [15], the relationship between the increment in coating thickness and the increment in pressure (ΔP) in the environment is given by the formula:

$$\Delta d = -\frac{\Delta P B (B^2 + A_W^2)(1+\sigma)(1-2\sigma)}{E\left[B^2 + A_W^2(1-2\sigma)\right]}$$

Here, $B = A_w + d$, E represents Young's modulus, σ is the Poisson's ratio for the coating. The photo elastic shift (Δn_c) is estimated using the formula $\Delta n_c = K\Delta P$, where K denotes Brewster's coefficient. For butyl acrylate, we considered $\sigma = 0.3$, $K = 10^{-10}1/Pa$, and $E = 7 \times 10^8 Pa$. Neglecting slow phase effects arising from PCF cladding and core deformation due to the significantly higher Young's modulus

of quartz glass, the pressure increments in the surrounding liquid directly modulate the PCF transmission. As depicted in Figure 2.8, the sensitivity of the described pressure sensor is estimated as $d\lambda_{\min}/dP = 4 \times 10^{-5}\mu m/\text{atm}$. According to Eq. (1), the sensitivity can be altered by adjusting the thickness of the polymer coating (it will increase with an increase in d).

Figures 2.7 and 2.8 indicate that sensors employing an absorbing polymer coating are well-suited for assessing parameters in liquids.

While numerous absorbing coatings for silica fibers are currently known [1, 2], our calculations reveal that most of these coatings can be used in sensors similar to those considered here. However, the impact of leaky mode resonance coupling varies when employing low-refractive and high-refractive absorbing coatings, as evidenced by data presented in Figures 9 and 10. These figures pertain to tin dioxide coatings doped with antimony (7 wt%) that selectively adsorb ammonia molecules from air. The calculations were carried out for the adiabatic taper with the mentioned parameters, but surrounded by air instead of water. The SnO2 coating has a thickness of $0.6\mu m$, its complex refractive index is $n_c = 1.90819 - i0.00042$, and an adsorption layer of ammonia molecules on the outer surface of the coating possesses a thickness of $0.37nm$ and a refractive index $n_a = 1.355$. These parameters were chosen based on experimental data obtained using the prism-coupler scheme [16]. Figures 2.9 and 2.11 depict the sensor's initial state in the absence of an adsorption layer.

Upon comparing Figs. 2.4b and 2.9b, the transition from a low-refractive to a high-refractive coating noticeably increases the attenuation of coating modes at wavelengths corresponding to the intersection points of curves 3 and 4 with curve 2. This intensifies the mismatch between the complex propagation constants of the PCF core mode and coating modes, making the above coupling-mode model even more significant. This may explain the presence of only one loss peak in the vicinity of the dashed curves in Fig. 2.9a, contrary to the previously observed two peaks.

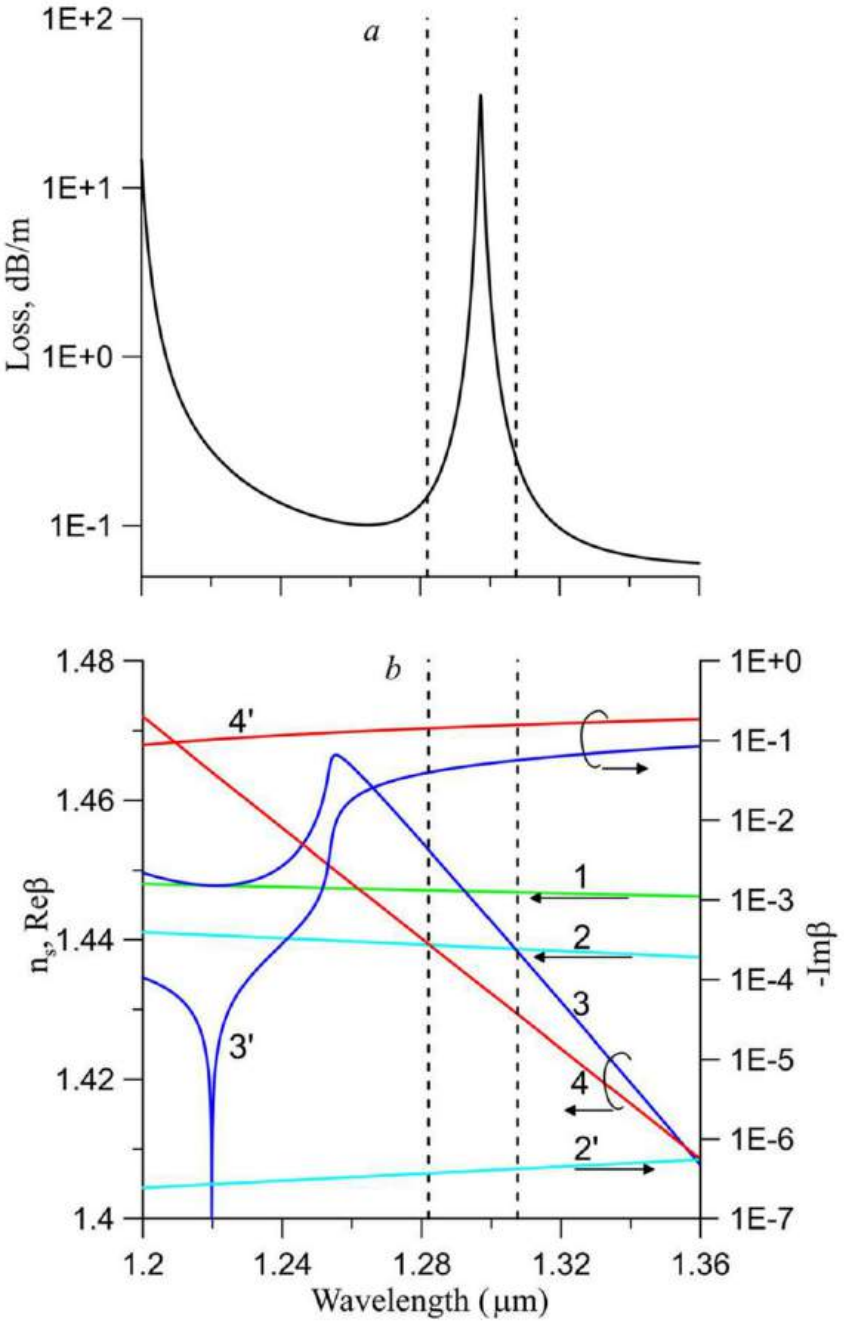

Figure 2.9: The spectral relationships of mode propagation constants are presented for the tapered PCF with a SnO2 coating of $0.6\mu m$ thickness, surrounded by air. The description of the curves is as follows: Curve 1 represents the refractive index of quartz glass. Curves 2 and 2' correspond to the real ($Re\beta$) and imaginary ($Im\beta$) components of the PCF core mode. Curves 3 and 3' depict the real ($Re\beta$) and imaginary ($Im\beta$) components of the TE mode of the coating. Curves 4 and 4' exhibit the real ($Re\beta$) and imaginary ($Im\beta$) components of the TM mode of the coating. Dashed lines indicate the wavelengths of phase synchronism between the PCF core and coating modes.

Figure 2.11 compares the intensity distributions of the PCF mode at resonant ($\lambda = 1.297\mu m$) and non-resonant ($\lambda = 1.26\mu m$) wavelengths (see Fig. 2.9a), holding a similar significance to Fig. 6. An analysis of Fig. 2.11 allows for conclusions akin to those drawn from the examination of Fig. 2.6 earlier.

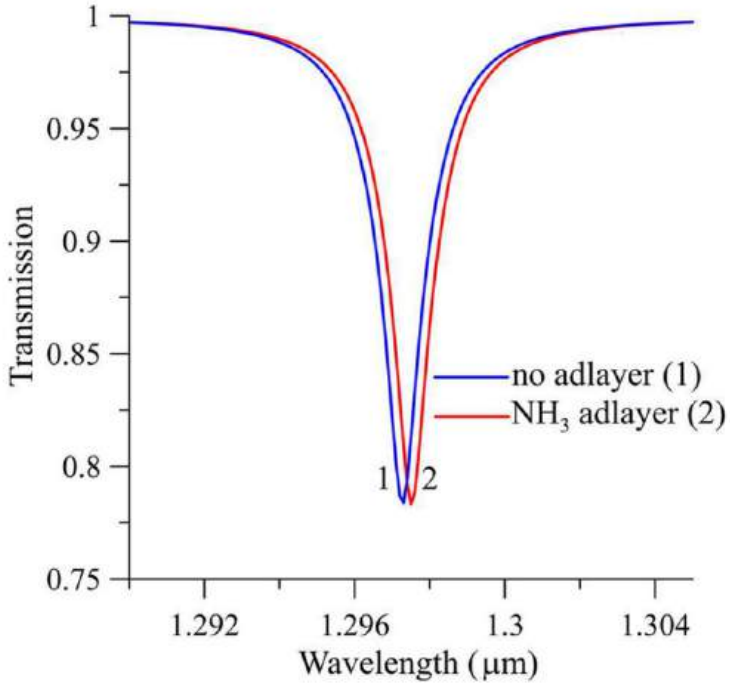

Figure 2.10: The shift in the transmission spectrum of the adiabatic taper in the PCF, having a length of $L = 3cm$ and a tin dioxide coating with a thickness of $0.6\mu m$, occurs upon the creation of an adsorption layer of ammonia molecules, with a thickness of $0.37nm$, on the surface of the coating.

Figure 2.10 demonstrates the alteration in the transmission spectrum of the SnO2-coated adiabatically tapered PCF when an adsorption layer of ammonia molecules is deposited on the coating. The thickness of this adsorption layer is known to be contingent upon the concentration of ammonia in the atmosphere. Moreover, it is imperative to note that an excessive release of ammonia can pose a threat by polluting the atmosphere [17].

Based on the data presented in Figures 2.9, 2.11, and 2.10, sensors utilizing high-refractive absorbing coatings, as described, exhibit potential for detecting nanoscale

adsorption layers.

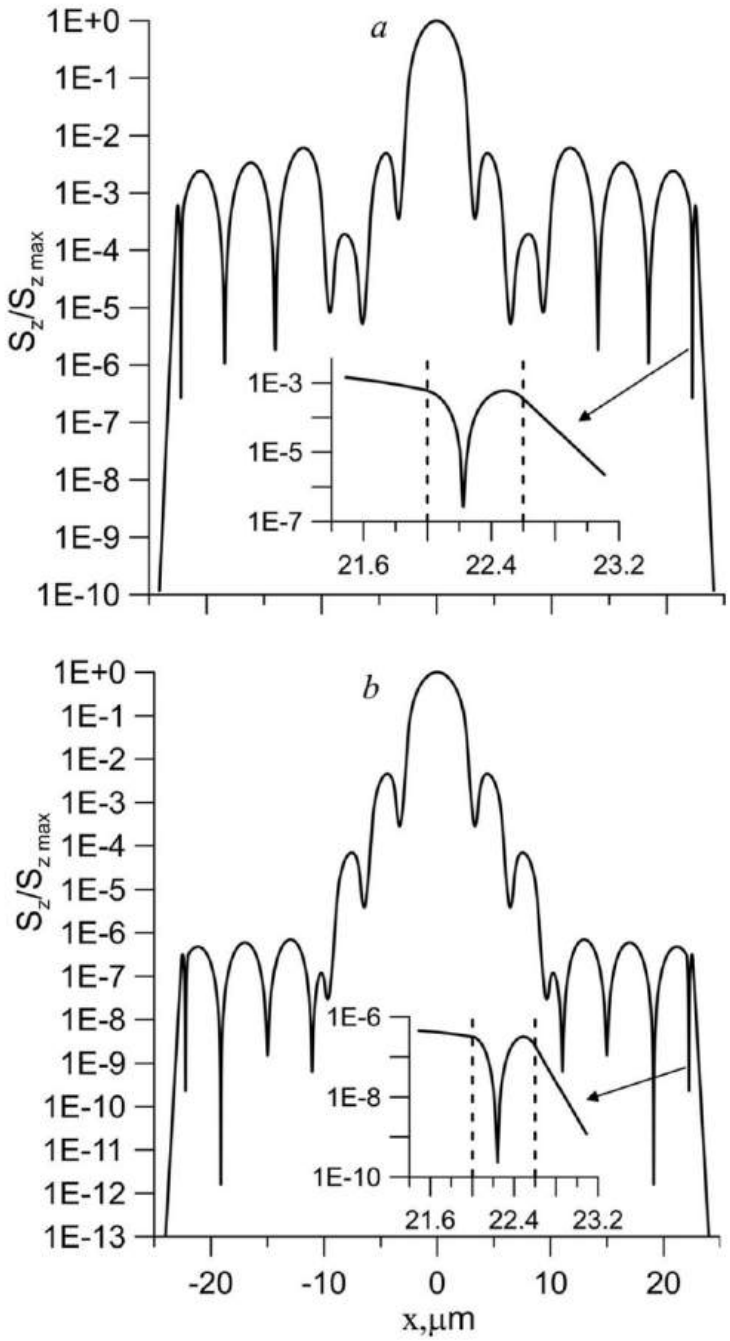

Figure 2.11: The distributions of the tapered PCF fundamental mode intensity $S_z(x,0)/S_z\,\mathrm{max}$ are illustrated at wavelengths $1.297\mu m(a)$ and $1.26\mu m(b)$. Dashed lines mark the boundaries of the tin dioxide coating.

We conducted theoretical investigations of the Leaky Mode Resonance (LMR) by utilizing specific single-mode PCFs with thin-film absorbing coatings of varying

thickness and refractive indices. The emergence of this LMR was attributed to the interaction between fundamental leaky modes of the PCF core and the coating. Our analysis of intensity distributions for the PCF fundamental mode revealed that the coupling between the PCF core mode and the absorbing coating, situated on the outer surface of the PCF, occurs through waves propagating within the fiber cladding, generating standing waves within the cladding.

We found that LMR in PCFs can be achieved by applying a thin-film coating directly to the outer surface of the PCF cladding without locally modifying the cladding. This results in multi-peak spectral transmission in the PCF. Two qualitative mechanisms were proposed for implementing such transmission. The first involves resonance coupling of the leaky fundamental PCF mode with the coating's leaky modes, leading to the capture of the fundamental PCF mode's energy by the coating and subsequent heat release. The second, observed in PCFs with sufficiently small cladding diameters in adiabatically tapered special PCFs, comprises resonance coupling of the leaky fundamental PCF mode with cladding modes located between air channels and the absorbing coating.

Compared to the latter mechanism, the first mechanism allows for the realization of narrower spectral absorption bands, making it more appealing for sensor applications. We demonstrated, through examples such as refractive index, pressure, and ammonia molecular adsorption layer sensors, that minor changes in the refractive index and/or the PCF absorbing coating's thickness lead to detectable spectral shifts in PCF transmission near resonance wavelengths.

Compared to LMR sensors utilizing standard multimode fibers where the absorbing coating is applied directly to the fiber core, the investigated sensors are less sensitive to changes in the refractive index of the surrounding liquid. However, they exhibit spectral widths of resonance more than an order of magnitude lower. Notable advantages of the considered sensors include their single-mode operation and the potential to almost entirely eliminate diffraction losses of light energy in the PCF

sensitive segment.

This work aimed to outline the fundamental aspects of LMR in PCFs with absorbing coatings and did not delve into optimizing sensor capabilities in detail. The detailed exploration and experimental realization of these devices will be the focus of a separate forthcoming publication.

Bibliography

[1] I. Del Villar, F. J. Arregui, C. R. Zamarreño, J. M. Corres, C. Bariain, J. Goicoechea, C. Elosua, M. Hernaez, P. J. Rivero, A. B. Socorro, A. Urrutia, P. Sanchez, P. Zubiate, D. Lopez, N. De Acha, J. Ascorbe, and I. R. Matias. Optical sensors based on lossy-mode resonances. *Sensors and Actuators B: Chemical*, 240:174–185, 2017.

[2] A. Ozcariz, C. Ruiz-Zamarreño, and F. J. Arregui. A comprehensive review: Materials for the fabrication of optical fiber refractometers based on lossy mode resonance. *Sensors*, 20(7):1972, 2020.

[3] V. P. Minkovich, V. Kir'yanov, A. B. Sotsky, and L. I. Sotskaya. Large-mode-area holey fibers with a few air channels in cladding: modeling and experimental investigation of the modal properties. *Journal of the Optical Society of America B*, 21(6):1161–1169, 2004.

[4] T. P. White, R. C. McPhedran, C. M. De Sterke, L. C. Botten, and M. J. Steel. Confinement losses in microstructured optical fibers. *Optics Letters*, 26(21):1660–1662, 2001.

[5] A. B. Sotsky, L. I. Sotskaya, V. P. Minkovich, and D. Monzón-Hernández. Mode attenuation in microstructured optical fibers with absorbing coating. *Technical Physics*, 54(6):865–873, 2009.

[6] I. H. Malitson. Interspecimen comparison of the refractive index of fused silica. *Journal of the Optical Society of America*, 55(10):1205–1209, 1965.

[7] G. A. Cardenas-Sevilla, D. Monzon-Hernandez, and V. P. Minkovich. Demonstration of an all-fiber band-rejection filter based on a tapered photonic crystal fiber. *Applied Physics Express*, 5(2):022502, 2012.

[8] V. P. Minkovich, D. Monzón-Hernández, J. Villatoro, A. B. Sotsky, and L. I. Sotskaya. Modeling of holey fiber tapers with selective transmission for sensor applications. *Journal of Lightwave Technology*, 24(11):4319–4328, 2006.

[9] A. B. Sotsky. *Theory of optical waveguide elements*, pages 422–427. Kuleshov University, Mogilev, 2011. [in Russian].

[10] A. B. Sotsky, L. M. Steingart, J. H. Jackson, P. Y. Chudakovskii, and L. I. Sotskaya. Prism excitation of leaky modes of thin films. *Technical Physics*, 58(11):1651–1660, 2013.

[11] V. P. Minkovich and A. B. Sotsky. Tapered photonic crystal fibers coated with ultra-thin films for highly sensitive bio-chemical sensing. *Journal of the European Optical Society - Rapid Publications*, 15(7):1–6, 2019.

[12] K. Xu. Silicon electro-optic micro-modulator fabricated in standard cmos technology as components for all silicon monolithic integrated optoelectronic systems. *Journal of Micromechanics and Microengineering*, 31(5):054001, 2021.

[13] A. K. Sharma and B. D. Gupta. On the sensitivity and signal to noise ratio of a step-index fiber optic surface plasmon resonance sensor with bimetallic layers. *Optics Communications*, 245(1–6):159–169, 2005.

[14] I. Del Villar, M. Hernaez, C. R. Zamarreño, P. Sánchez, C. Fernández-Valdivielso, F. J. Arregui, and I. R. Matias. Design rules for lossy mode resonance based sensors. *Applied Optics*, 51(19):4298–4307, 2012.

[15] L. D. Landau, E. M. Lifshitz, A. M. Kosevich, and L. P. Pitaevskii. *Theory of Elasticity*, volume 7 of *Course of Theoretical Physics*. Elsevier, 1986.

[16] A. V. Khomchenko. *Waveguide Spectroscopy of Thin Films*. Academic Press, 2005.

[17] J. Kim, H. Lee, H. T. Vo, G. Lee, N. Kim, S. Jang, and J. B. Joo. Bead-shaped mesoporous alumina adsorbents for adsorption of ammonia. *Materials*, 13(1375):1–13, 2020.

Chapter 3

Methodology of Manufacturing PCFs

3.1 Experimental Model to Calculate Optical Properties of PCFs

To study optical properties of PCFs, Koshiba and Satoih propose an experimental fitting model for the normalized frequency (V) associated with a hexagonal photonic crystal fiber that operates at a wavelength (λ) and has an effective core radius ($a_{eff} = \Lambda/\sqrt{3}$). On the other hand, the normalized frequency can be decomposed into the parameters U and W, associated with normalized transverse phase and attenuation constant, respectively. Now, these parameters do not relate the core refractive index (n_{co}) to the cladding refractive index (n_{FSM}), but rather concatenate these indices with the effective refractive index (n_{eff}) associated with the photonic crystal structure present in the optical fiber ([1] and [2]). The decomposition of the parameter V into the parameters U and W is shown below.

$$V = \frac{2\pi}{\lambda} a_{eff} \sqrt{n_{co}^2 - n_{FSM}^2} = \sqrt{U^2 + W^2} \tag{3.1}$$

$$U = \frac{2\pi}{\lambda} a_{eff} \sqrt{n_{co}^2 - n_{eff}^2} \tag{3.2}$$

$$W = \frac{2\pi}{\lambda} a_{eff} \sqrt{n_{eff}^2 - n_{FSM}^2} \tag{3.3}$$

3.2 Calculation of parameter V

The parameter V has an effective value for an effective core radius equal to the lattice spacing parameter. This value is shown below along with its corresponding fitting parameters a_{ij}.

$$V_{eff} = \frac{2\pi}{\lambda}\Lambda\sqrt{n_{eff}^2 - n_{FSM}^2} \tag{3.4}$$

$$V\left(\frac{\lambda}{\Lambda}, \frac{d}{\Lambda}\right) = A_1 + \frac{A_2}{1 + A_3 exp(A_4\lambda/\Lambda)} \tag{3.5}$$

$$A_i = a_{i0} + a_{i1}\left(\frac{d}{\Lambda}\right)^{b_{i1}} + a_{i2}\left(\frac{d}{\Lambda}\right)^{b_{i2}} + a_{i3}\left(\frac{d}{\Lambda}\right)^{b_{i3}} \tag{3.6}$$

	i=1	i=2	i=3	i=4
a_{i0}	0.54808	0.71041	0.16904	-1.52736
a_{i1}	5.00401	9.73491	1.85765	1.06745
a_{i2}	-10.43248	47.41496	18.96849	1.93229
a_{i3}	8.22992	-437.50962	-42.4318	3.89
b_{i1}	5	1.8	1.7	-0.84
b_{i2}	7	7.32	10	1.02
b_{i3}	9	22.8	14	13.4

Table 3.1: Adjustment coefficients for the parameter V.

Below is the behavior of the parameter V for some PCFs with specific values for the filling ratio d/Λ.

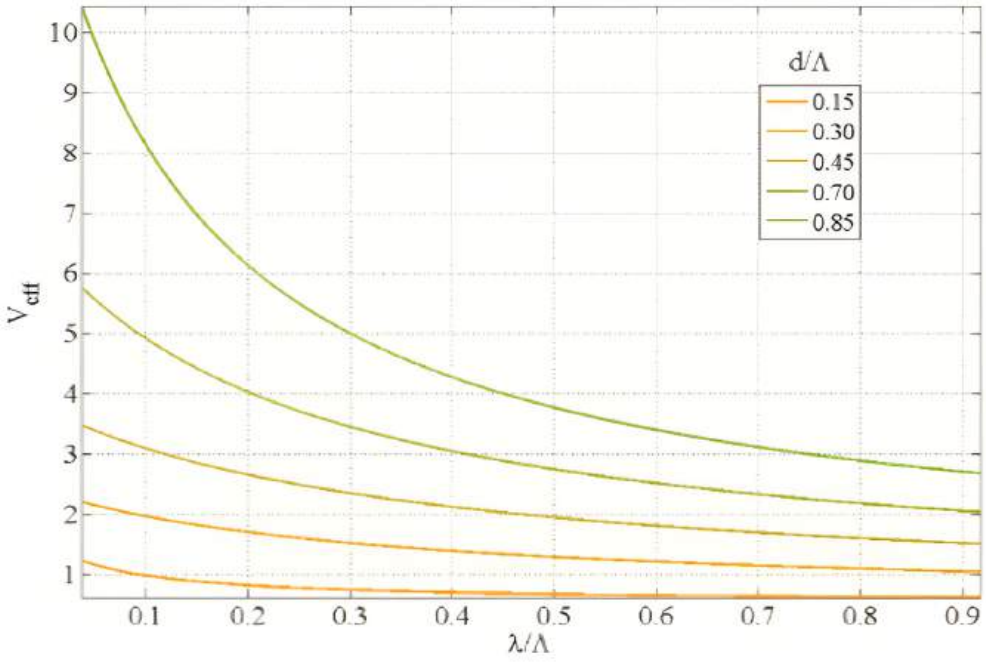

Figure 3.1: Behavior of the parameter V for some PCFs [3].

Also, it is possible to observe the single-mode and multimode regions by making a contour plot of the parameter V, specifically for the value 2.405, in relation to its independent variables λ/Λ and d/Λ. Below is the result:

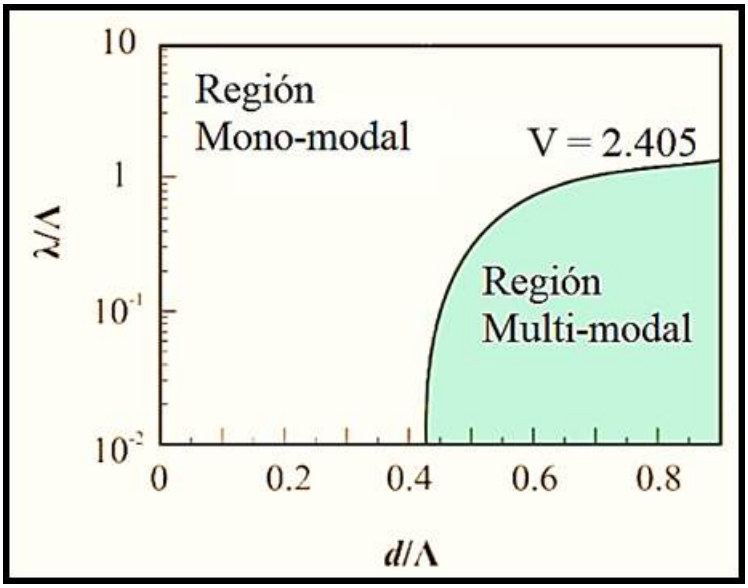

Figure 3.2: Single-mode and multimode regions using a contour plot of the normalized frequency [1].

3.3 Calculation of parameter W

Analogously, for the parameter W we have:

$$W\left(\frac{\lambda}{\Lambda}, \frac{d}{\Lambda}\right) = B_1 + \frac{B_2}{1 + B3exp(B_4\lambda/\Lambda)} \tag{3.7}$$

$$B_i = c_{i0} + c_{i1}\left(\frac{d}{\Lambda}\right)^{d_{i1}} + c_{i2}\left(\frac{d}{\Lambda}\right)^{d_{i2}} + c_{i3}\left(\frac{d}{\Lambda}\right)^{d_{i3}} \tag{3.8}$$

	i=1	i=2	i=3	i=4
c_{i0}	-0.0973	0.53193	0.24876	5.29801
c_{i1}	-16.70566	6.70858	2.72423	0.05142
c_{i2}	67.13845	52.04855	13.28649	-518302
c_{i3}	-50.25518	-540.66947	-36.80372	2.7641
d_{i1}	7	1.49	3.85	-2
d_{i2}	9	6.58	10	0.41
d_{i3}	10	24.8	15	6

Table 3.2: Adjustment coefficients for parameter W.

Below is the behavior of the parameter W for some PCFs with specific values for the filling ratio $\frac{d}{\Lambda}$.

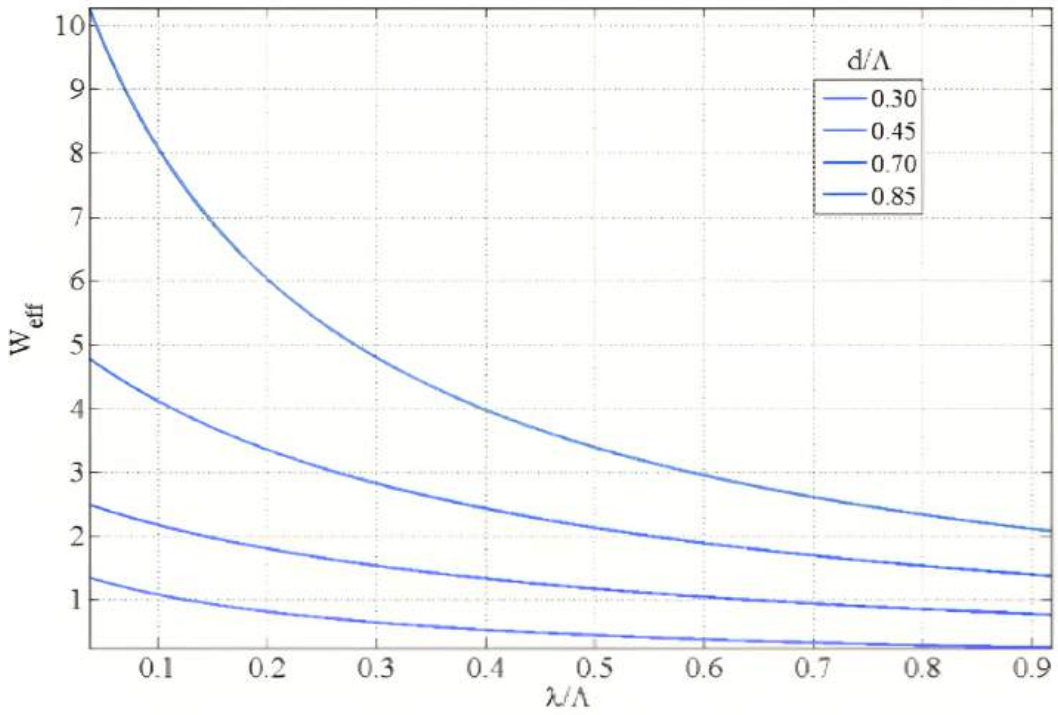

Figure 3.3: Behavior of the parameter W for some PCFs [3].

3.4 Effective refractive index n_{FSM}

Finally, the parameter of interest for calculating, for example, chromatic dispersion is the effective refractive index. To obtain it, it is necessary to solve the system of equations formed by equations 3.3 and 3.4 once the values of V and W are known, which are obtained using equations 3.5 and 3.7, collecting all the coefficients shown in tables 3.1 and 3.2 respectively ([1], [4], [2]). Now, the behavior of the refractive indices n_{eff} and n_{FSM} for different PCFs can be observed below:

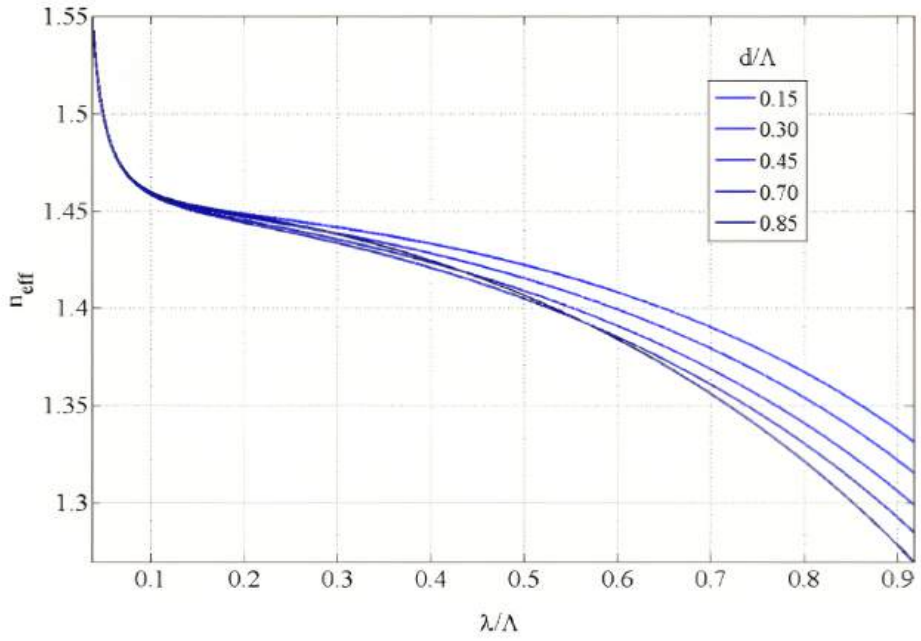

(a) n_{eff}

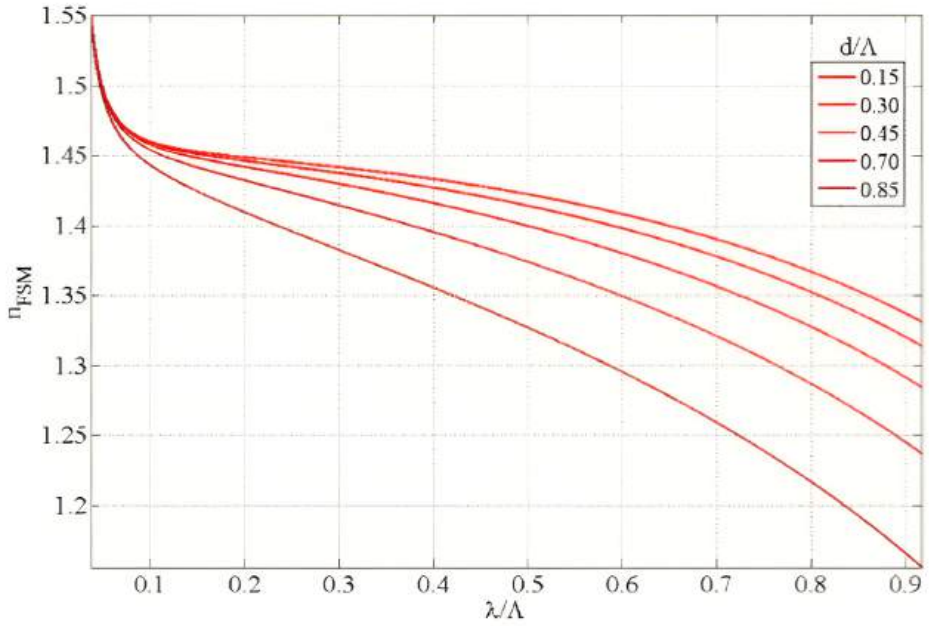

(b) n_{FSM}

Figure 3.4: Behavior of the effective and cladding refractive indices under approximation for different PCFs [3].

So, in Figure 3.5, the chromatic dispersion is shown after fixing a lattice parameter ($\Lambda = 2.5\ \mu m$) and varying the dimension of the holes to obtain different filling ratios (d/Λ).

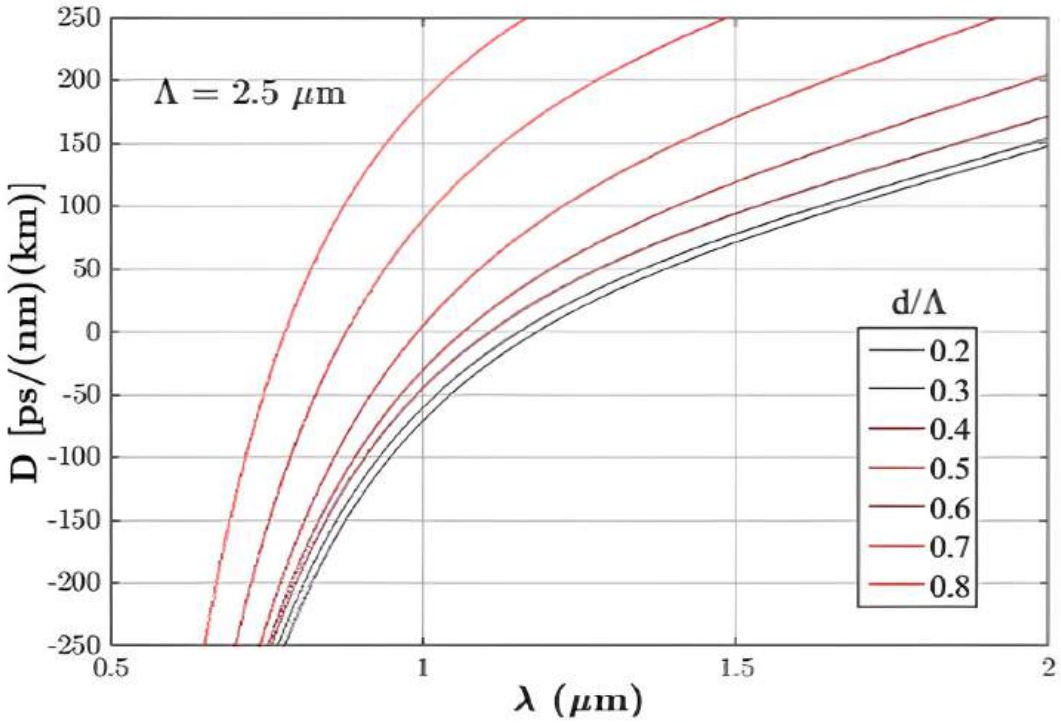

Figure 3.5: Chromatic dispersion for a PCF with a lattice parameter $\Lambda = 2.5\ \mu m$ and different hole diameters [3].

3.5 Design of the preform.

The manufacturing process of a PCF begins with the design of a stack (a set of stacked elements forming the structure of a photonic crystal fiber). The stack is composed of rods (solid tubes that help fix the stack's structure), tubes (hollow tubes that provide the hexagonal structure of the photonic crystal), and the core located in the center of the photonic crystal, which is typically made of silica. The mentioned pieces can be stacked using an epoxy resin binder with a refractive index similar to that of silica.

To determine the dimensions of the tubes, the first step is to define the dispersion zero that the PCF will have according to the required applications. Once this is defined, a dispersion curve is generated, and its zero is approximated as proposed. Since the dispersion curve explicitly depends on the structural parameters of the PCF (d and Λ), it is possible to scale these parameters according to the dimensions

of standard elements in fiber optic manufacturing processes to obtain the dimensions that the tubes should have. Subsequently, each of the tubs and rods is stretched using a fiber optic stretching tower. Below is the final design of the stack used to manufacture the series of PCFs obtained in this work, created using commercial software (AutoCAD). Additionally, the calculation of the required tubs to form the designed stack is shown, obtained from a program created in Matlab, and the program is attached in the appendices.

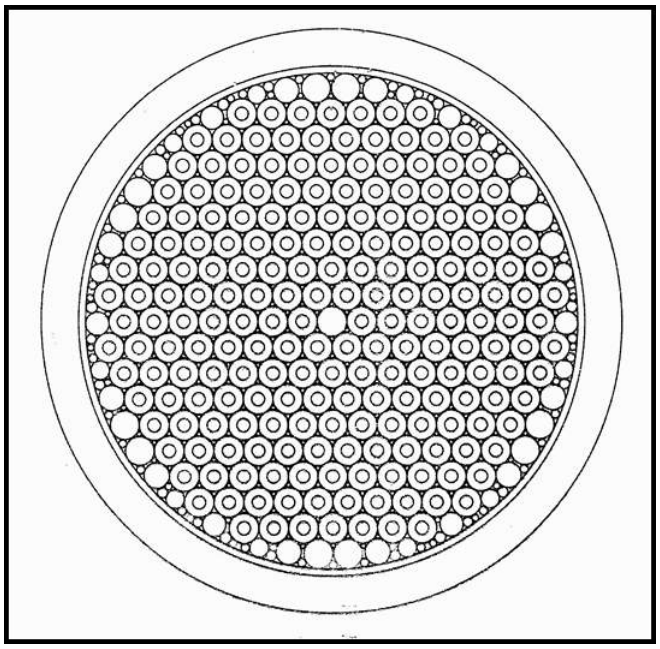

(a) Design of Stack (Tubes and Rods)

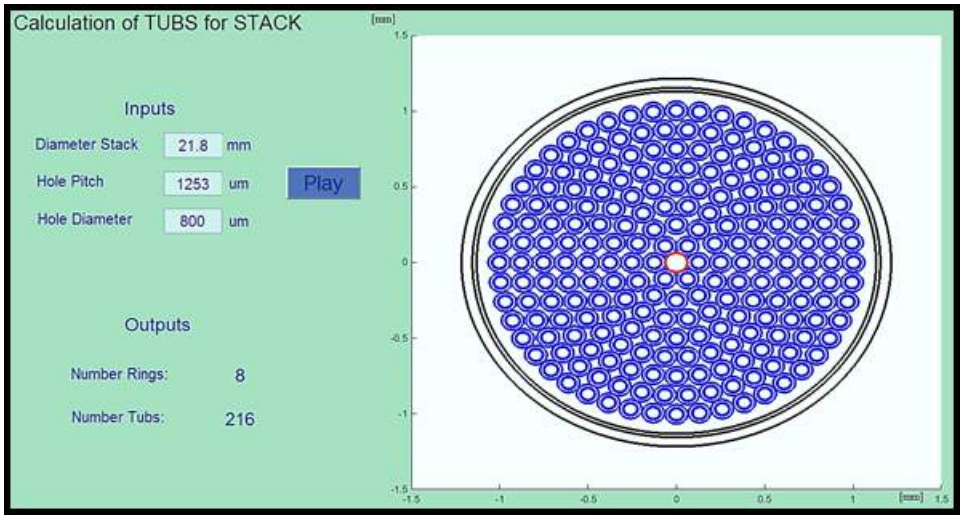

(b) Design of Stack (Tubs)

Figure 3.6: Design of Stack used to built the PCF.

This *stack* contains all the information to know how many *tubes* and *rods* need to be manufactured individually and what dimensions each one must have. Additionally, it is worth mentioning that to modify the dimensions of the external diameter of the *tubes* or *rods* the speed with which the material is extracted from the oven is varied by means of an electronically controlled pulley mechanism. Regarding the internal diameter of the *tubes*, it can be varied by changing the pressure (normally working

with a pressure of 100 mbar) of the flow of argon gas that circulates throughout the material, or also by changing the temperature of the smelting furnace (normally works at 1950 °C). This temperature is below the working temperature of 2000 °C, used to stretch standard FO, since softening the hollow structure that a PCF has requires less energy. This is also taken into account when splicing PCFs with FOs, since in the process the gaps can collapse if the parameters that occur during the process are not controlled. Below is the *stack* obtained in the laboratory after the manufacturing process of around 250 *tubes* and 150 *rods*.

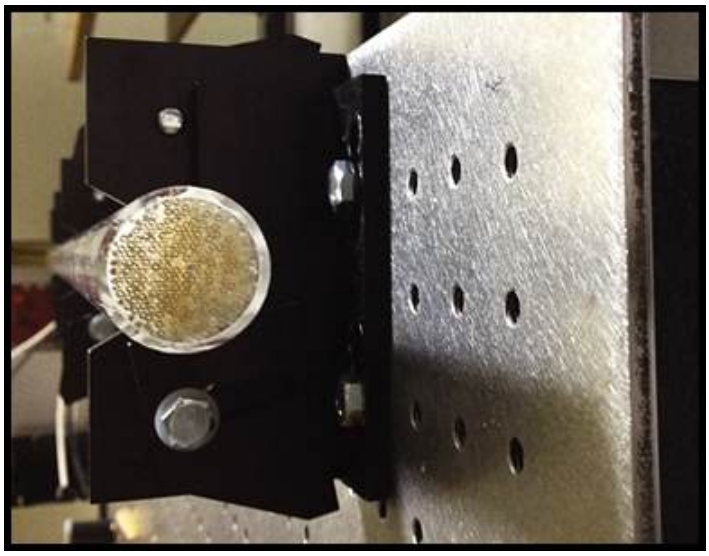

Figure 3.7: Arrangement of tubes and rods arranged to form the PCF preform.

Finally, the complete manufacturing of a PCF is obtained through stages that range from the manufacturing of the tubes and rods to form the stack, to the second preform from which the optical fiber is finally obtained. These stages are shown below:

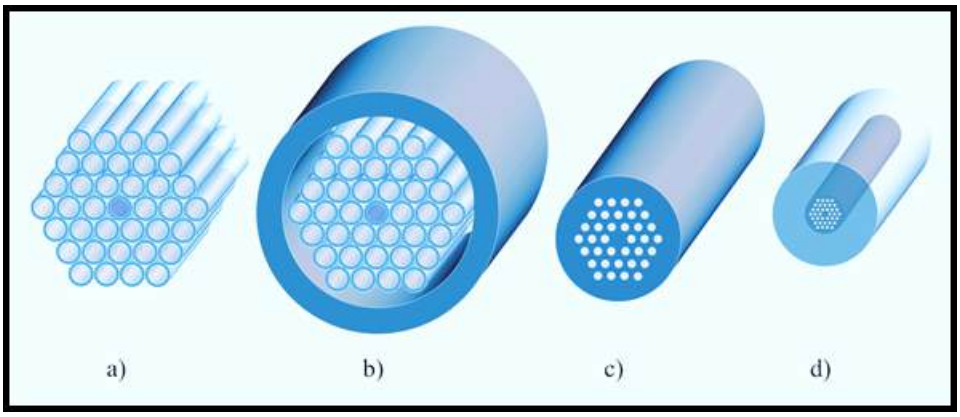

Figure 3.8: Manufacturing stages of a PCF: a) CF structure (Tubes + Rods); b) Stack; c) Cane; d) Second preform (Cane + Jacket) [3].

3.6 Preform

To obtain a PCF, it is necessary to manufacture each element of the design piece by piece. Then, the elements are assembled and fixed by sealing the ends of the manufactured stack. This is done to ensure that it does not come apart. The sealing stage of the preform is shown below.

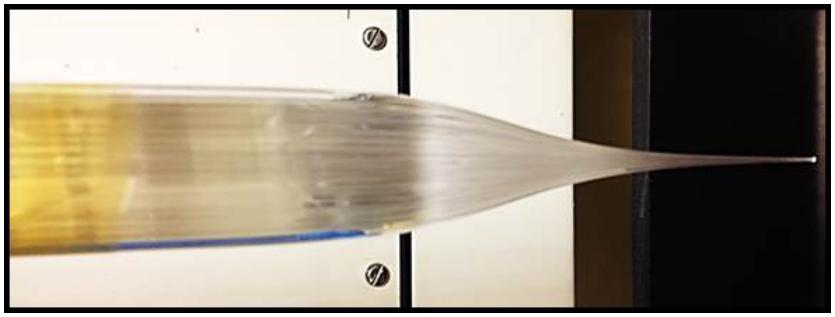

Figure 3.9: Sealing process at the preform ends for the PCF.

3.7 PCF Stretching

The phase that molten silicon dioxide or fused silica must reach to be used in the manufacturing of optical fibers is the super cooled liquid phase, so that it can later form a glass that is cast slowly or rapidly depending on the crystallization rate employed. The crystallization rate depends on viscosity, temperature ramp, and Gibbs

free energy, which determines the material's tendency to crystallize. Crystals have a melting temperature (T_m) and do not have an associated glass transition temperature (T_g); conversely, this is the case for glasses. For crystals, viscosity decreases logarithmically with increasing temperature.

To obtain cast glass from the crystalline phase, it is necessary to apply a rapid heating profile that transitions the material to the liquid phase. Subsequently, to move from the liquid phase to glass, the material must be allowed to gain volume, reducing its density progressively while decreasing the temperature. This transition occurs consecutively from the super cooled liquid phase to the cast glass phase, either slowly or rapidly, depending on the cooling profile employed. This process can be applied to each glass element used in the drawing tower with the help of a furnace that allows the material to fall by gravity. The phase diagram is illustrated below:

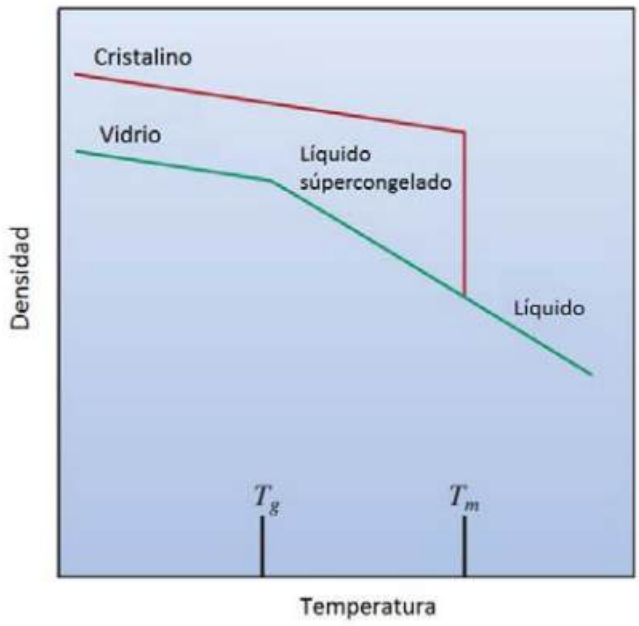

Figure 3.10: Phase diagram representing transitions from the crystalline or glass phase to the liquid phase [5].

Once the preform is obtained, it is possible to obtain the PCF. Initially, there is the preform positioning process where a light beam is used to check the material's continuity, and a flow of argon gas is passed through to support the structure and

prevent it from collapsing. Subsequently, there are the PCF diameter gauges and the stretching mechanism that allow for controlling and monitoring the PCF dimensions. Next, the process involves adding the polymeric coating to the PCF using a liquid solution, which is then sealed with UV radiation. Finally, the PCF is collected in a container at the end of the process. The steps that the PCF goes through in the drawing tower are illustrated below.

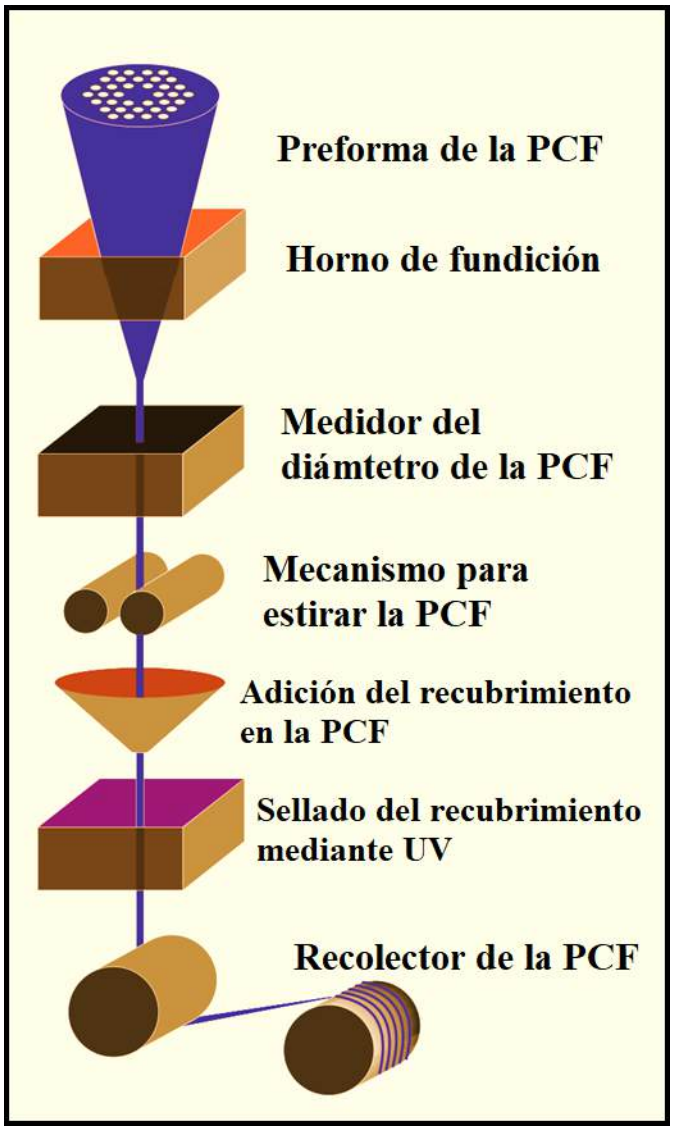

Figure 3.11: Stretching process of the PCF [3].

Now, it is worth noting that the guiding mechanism for this optical fiber is through refractive index (IG, index-guiding) and not through a forbidden energy band since

this PCF has a solid core of silica doped with germanium.

It is important to note that when the pressure of the argon gas flow is excessive, it can distort the preform because the material is softened and can be deformed by the formation of bubbles inside, due to the pushing force of the gas in the cross-section of the preform. This is illustrated below.

Finally, we show a photograph from an optical microscope of a PCF where the tubes or capillaries have collapsed due to the use of high pressure in the preform during the manufacturing process. The structure of this PCF is completely distorted compared to the designed stack.

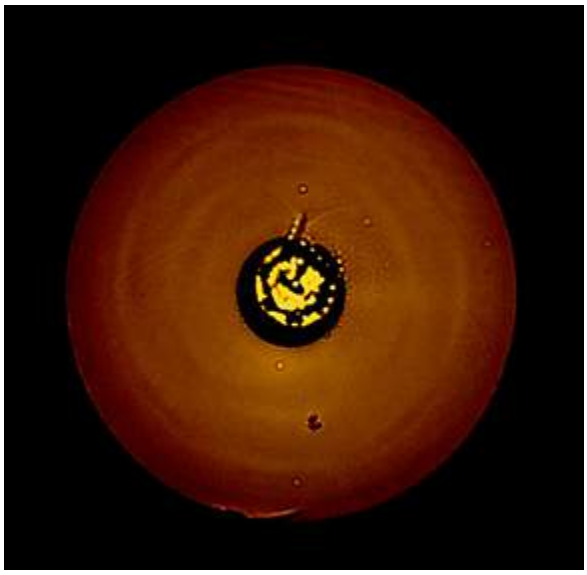

Figure 3.12: Cross section of the PCF altered by the use of high pressures in the capillaries seen from an optical microscope.

3.8 Confinement Losses by Influence of Microestructure Parameters of PCFs

The leakage properties depend on hole diameter, on their pitch and on the number of ring witch define the microestructure and the behavior of the field confinement and

its decay rate.

In figure 3.13, confinement losses are presented as functions of hole diameter with a constant pitch for different numbers of rings and of pitch for different ratios of microestructure:

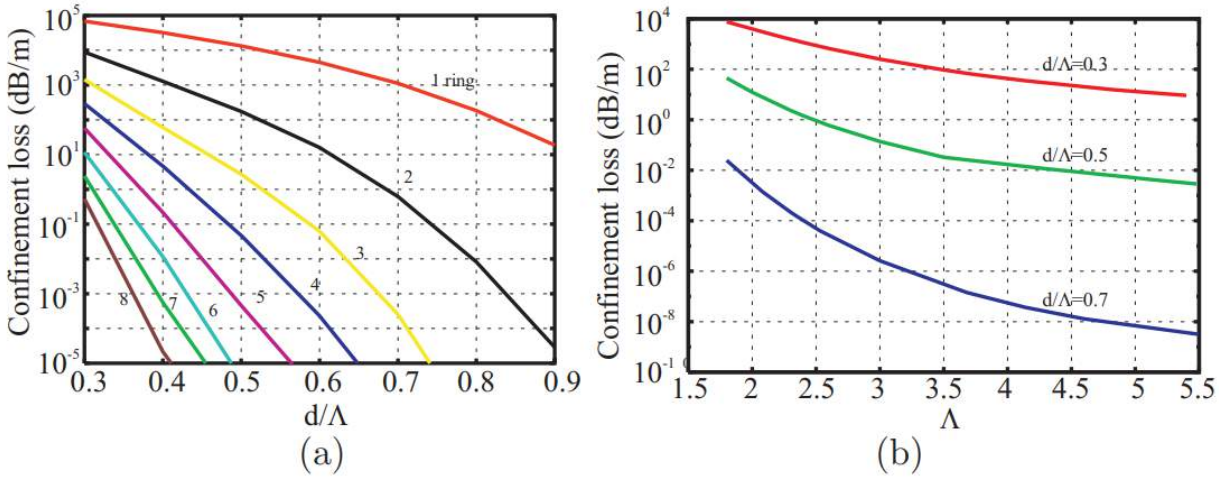

Figure 3.13: (a): Confinement loss as a function of hole diameter 'd' normalized to pitch '$\Lambda = 2.3\mu m$' for different numbers of rings. (b): Confinement loss as a function of pitch 'Λ' for different ratios 'd/Λ'. In both cases, a wavelength '$\lambda = 1.55\mu m$' is assumed. [6]

Confinement losses decrease when the microestructure ratio increase respect to the hole diameter. They also show high values for low number of rings and the other way around it presents small values for many rings. Furthermore, confinement losses decay when pitch is increased respect to different constant microestructure ratios and they get high values for microestructure ratios with low value.

3.9 Fabrication of a 2 Ring PCF for Sensing

Fiber optic sensors exploiting lossy mode resonance (LMR) have been the subject of extensive research [7, 8]. LMR arises from the interaction between light trav-

eling through an optical fiber and a specially designed thin-film absorbing coating, often present on a side-polished section of the fiber cladding. When coating modes are aligned with the fiber modes, they can couple together. The manifestation of LMR is contingent upon the properties of the coating and variations in the surrounding medium's optical properties. These alterations cause noticeable changes in the transmission spectrum of the fiber, creating a sensory effect [9, 10].

Traditionally, devices leveraging this effect have relied on standard multimode optical fibers, resulting in relatively broad absorption bands. Moreover, these conventional fibers are notably delicate due to their modified claddings in regions supporting LMR [11, 12].

An alternative approach to realize LMR, as discussed theoretically in the previous chapter, involves utilizing specialized photonic crystal fibers (PCFs) featuring three air channel rings that were fabricated preliminary before starting the work on this thesis. We spent about two and a half of months to fabricate adiabatic tapers from these three air channel rings PCFs to confirm our theoretical results presented in our Chapter 2. Unfortunately, by using our CIO tapering equipment we did not fabricate the needed tapers with stable waist diameters. For this reason, we designed and fabricated new PCFs with two air channel rings to use in our subsequent research these untapered PCFs with an absorbing coating made from butyl acrylate polymer mentioned in our calculation.

The stack-and-draw method [3] was employed in the fabrication of our PCFs. The design of the preform for drawing the PCFs is outlined in Figure 3.14(a). This preform is based on a cladding tube characterized by an inner diameter of 9.5 mm and an outer diameter of 19.9 mm. Two complete hexagonal layers of capillaries and supplementary rods are arranged around a solid core rod. Additional filler rods are incorporated to mitigate preform deformation during PCF fabrication and prevent the emergence of unintended channels. A cross-sectional view of the preform is depicted in Figure 3.14(b).

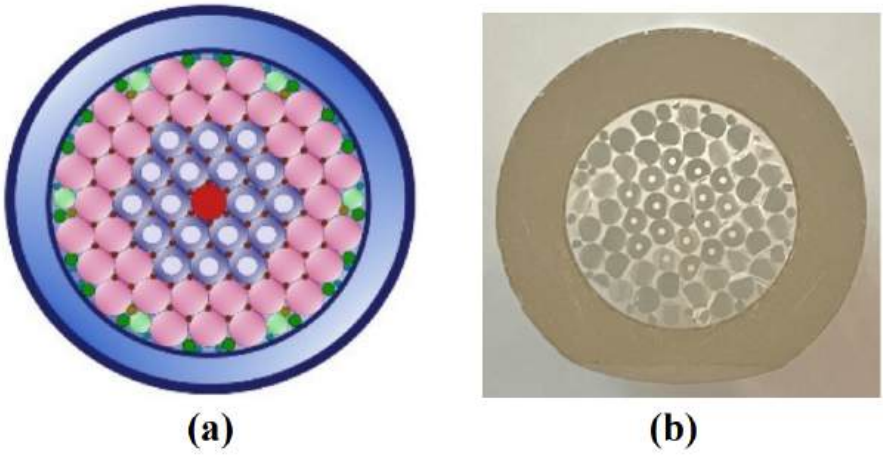

Figure 3.14: (a) Design of our preform and (b) a transversal image of the preform.

We produced our fibers from the previously mentioned preform in a single step by heating it using a Centorr Vacuum Ind. optical drawing furnace and an upgraded conventional fiber drawing tower (Heathway Inc.). This preform underwent drawing to create two PCFs (F1 and F2), possessing an outer diameter of $124 \pm 1\mu m$. This was achieved by utilizing varying gas pressures within the PCF preform and different drawing velocities. Finally, the PCFs were coated with a butyl acrylate polymer, resulting in an outer diameter of $220 \pm 2\mu m$.

The manufactured PCF samples, each approximately 300 meters in length, were wound onto spools measuring 16 cm in diameter. Figure 3.15 showcases optical microscope images, captured with a 40x objective, displaying the cleaved end faces of PCFs (F1) and (F2) with $d/\Lambda = 0.36$ [Figure 3.15(a)] and 0.43 [Figure 3.15(b)], respectively. Here, 'd' represents the diameter of the PCF air channels, while 'Λ' signifies the spacing between the air channels.

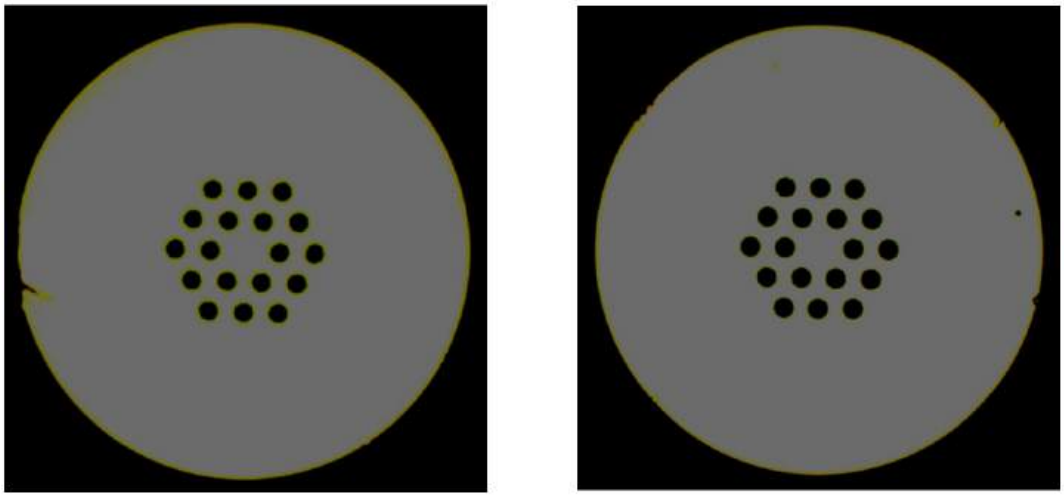

(a) (b)

Figure 3.15: Transversal cut images of fabricated PCFs: (a) PCF (F1), (b) PCF (F2).

To determine the geometric dimensions of 'd' and 'Λ' for our fibers, we employed an atomic force microscope (Digital Instruments) with a resolution of 50 nm for 30 µm x 30 µm images. Three measurements were taken for 'd' and 'Λ' for each of the fabricated PCFs, and their averages were subsequently calculated. Additionally, we calculated the mode field diameters (MFDs) for the fabricated fibers at 1.31 µm. The obtained results are presented in the following table.

Fibers	$d_{avg}(\mu m)$	$\Lambda_{avg}(\mu m)$	d/Λ	$MFD(\mu m)$
F1	3.31	9.10	0.36	6.70
F2	3.93	9.19	0.43	6.09

Table 3.3: Measurement results of geometric dimensions and results of our MFD calculations for fabricated PCFs.

Attenuation measurements were conducted using a cut-back method, as illustrated in figure 3.16(a). We utilized a white light source (AQ-4305) and an optical spectrum analyzer (AQ-6315E) for these measurements. The attenuation spectra for the fabricated fibers are depicted in figure 3.16(b). The spectra reveal three distinct

absorption peaks corresponding to the presence of OH- function groups situated at 950 nm, 1244 nm, and 1383 nm.

The fabricated fibers operate as single-mode fibers within the wavelength range from 550 nm to 1700 nm. They exhibit relatively high optical losses, exceeding 40 dB/km. The attenuation in the F1 fiber surpasses that in the F2 fiber due to the smaller 'd/Λ' ratio for the F1 fiber. Consequently, it is evident that the attenuation of the PCF fundamental mode in our fibers can be altered by varying 'd/Λ'. Estimations suggest that such fibers can be employed for fiber optic sensors measuring refractive index or pressure and for detecting a nanoscale adsorption layer of ammonia molecules deposited on a specialized, thin, absorbing coating.

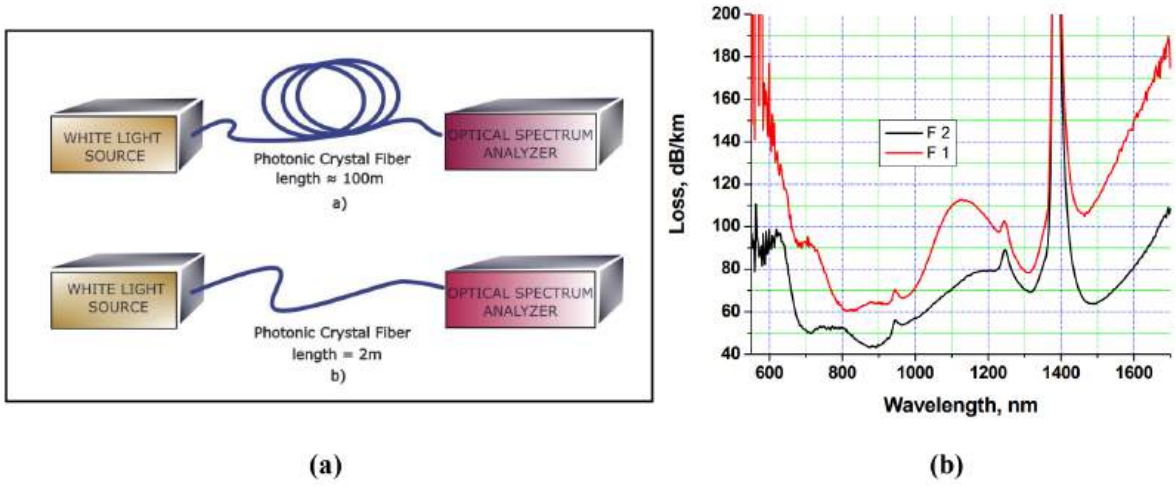

Figure 3.16: (a) Experimental scheme for attenuation measurements and (b) attenuation spectra for fabricated fibers.

In this study, we detail the design and fabrication process of specialized silica PCFs containing a solid core and two air channel rings within their claddings, tailored for use in fiber optic sensors relying on lossy mode resonance. Geometrical dimensions of 'd' and 'Λ', as well as mode field diameters for our fibers, were both measured and calculated. Two photonic crystal fibers, with relative channel diameters of 'd/Λ' equal to 0.36 (F1) and 0.43 (F2), were fabricated and subjected to attenuation measurements. These fibers exhibit attenuation rates exceeding 40 dB/km, with the F1

fiber displaying higher attenuation compared to the F2 fiber due to its smaller 'd/Λ' ratio.

Within our measured wavelength range spanning from 550 nm to 1700 nm, these fibers operate as single-mode fibers. We anticipate that these developed fibers, coupled with thin-film specialized absorbing coatings, hold substantial potential for diverse applications in various fiber optic sensors.

Bibliography

[1] Masanori Koshiba Kunimasa Saitoh. *Empirical relations for simple design of photonic crystal fibers.* Optical Society of America, Optics Express, Vol. 13, No. 1, pp. 267-274, 2005.

[2] Kunimasa S. Masanori K. *Applicability of classical optical fiber theories to holey fibers.* Optics Letters, Vol. 29, No. 15, pp. 1739-1741, 2004.

[3] Carlos Porras. *Design, fabrication and characterization of nonlinear photonic crystal fibers for telecommunication wavelength range and for near infrared wavelength supercontinuum light sources.* Tesis de Maestría, Centro de Investigaciones en Óptica., 2017.

[4] Naoya Inoue Yoh Imai Yutaka Sasaki Hirohisa Yokota, Kosuke Ushiroda. *Fabrication of photonic crystal fiber optical attenuators with air hole diameter control using CO2 laser irradiation technique.* Elsevier, Optical Fiber Technology, Vol. 23, pp. 37–41, 2015.

[5] Alejandro Santos. *Caracterización de las Propiedades Ópticas no Lineales de Vidrios de Telurio (TeO2) con Nanocristales Embebidos por Medio de la Técnica Z-scan.* Tesis de Maestría, Centro de Investigaciones en Óptica., 2014.

[6] K. Saitoh and M. Koshiba. Confinement losses in air-guiding photonic bandgap fibers. *IEEE Photonics Technology Letters*, 15(2):236–238, 2003.

[7] I. Del Villar, F. J. Arregui, C. R. Zamarreño, J. M. Corres, C. Bariain, J. Goicoechea, C. Elosua, M. Hernaez, P. J. Rivero, A. B. Socorro, A. Urru-

tia, P. Sanchez, P. Zubiate, D. Lopez, N. De Acha, J. Ascorbe, and I. R. Matias. Optical sensors based on lossy-mode resonances. *Sensors and Actuators B: Chemical*, 240:174–185, 2017.

[8] V. P. Minkovich, V. Kir'yanov, A. B. Sotsky, and L. I. Sotskaya. Large-mode-area holey fibers with a few air channels in cladding: modeling and experimental investigation of the modal properties. *Journal of the Optical Society of America B*, 21(6):1161–1169, 2004.

[9] T. P. White, R. C. McPhedran, C. M. De Sterke, L. C. Botten, and M. J. Steel. Confinement losses in microstructured optical fibers. *Optics Letters*, 26(21):1660–1662, 2001.

[10] J. Stone and G.E. Walrafen. *Overtone vibrations of OH groups in fused silica optical fibers.* The Journal of Chemical Physics., 76:1712, 1982.

[11] U. Grzesik U. Haken O. Humbach, H. Fabian and W. Heitmann. *Analysis of OH absorption bands in synthetic silica.* Journal of Noncrystalline Solids, 203:19–26, 1996.

[12] L. Bosselaar M. Bredol, D. Leers and M. Hutjens. *Improved model for OH absorption in optical fibers.* Journal of Lightwave Technology., 8(10):1536–1540, 1990.

Chapter 4

Applications for Bending and RI Sensing

4.1 Scheme of the platform system for sensing

In this chapter we present a PCF (Fiber F1) system with a dual-rings configuration using a bending setup that allows for the characterization of substances based on their refractive index. We demonstrate its application by measuring different concentrations of glycerin diluted in water.

When configuring the optical fiber system with a bending setup instead of using a straight optical fiber, a characteristic pattern of loss peaks appears. These peaks are formed by interference phenomena, whose appearance is associated with the optical path difference generated by the pressure applied to the system and the formation of resonant loss modes due to the increase in loss modes exiting the core towards the cladding caused by the bending. The scheme is shown in the next figure:

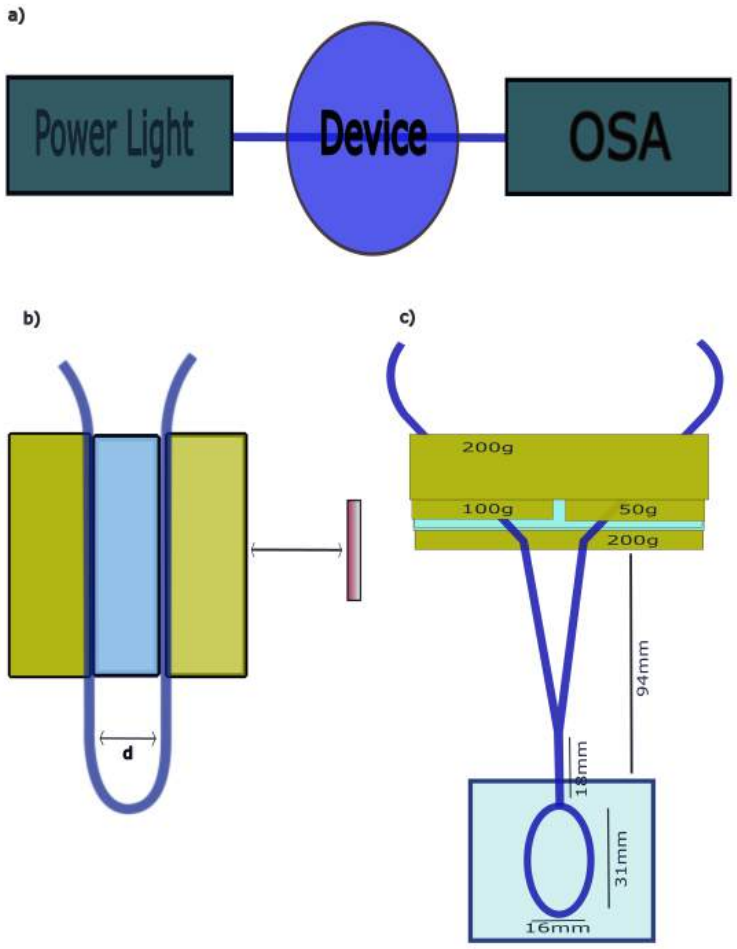

Figure 4.1: a) Scheme of the platform of sensing for different setups. b) setup for measurements of different kinds of bending and c) setup for several glycerin concentration measurements.

The sensing experiments consist of supplying white light to any of the given configurations in the optical fiber system and then measuring the resulting transmission. In the case of the bending configuration, the light transported inside the optical fiber is forced out of the core due to the change in the direction of the normal vector at the interface with the bending. This causes the spatial breakdown of the total internal reflection principle at each interface of the curved section. Ultimately, this results in the appearance of a loss spectrum associated with the magnitude of the applied bending. The nature of the loss pattern is due to interference phenomena and resonant loss modes, as periodicity is observed, and when the cladding is removed, fewer

losses are observed, since the possibility of resonance is eliminated.

On the other hand, for the experiment measuring the refractive index, we have 2 fixed weights at the input and output of a bending characterized by maximum amplitude. This configuration allows us to obtain a loss pattern associated with maximum bending, and additionally, losses can be increased by including fixed weights as they add elastic deformation to the fiber's cross-section and possibly birefringence in the affected area. The elastic deformation and birefringence produced by the fixed weights are considered negligible for theoretical calculations but relevant for experimental measurements because they enhance the sensitivity of the optical system.

4.2 Bending Measurements

Initially, the attenuation behavior was analyzed as a function of the separation of the optical fiber at the ends of the bending, as shown in scheme b of the previous figure. The appearance of a loss pattern composed of several peaks can be observed, shifting towards the infrared from the visible spectrum starting at a bending separation or bending diameter of 3.5 cm. The most pronounced loss peak is the last one in each case, which we assume is due to the formation of a resonant loss mode in the bending coating area. This assumption is based on the irregularity in the amplitude and wavelength of the peaks and the observation that when the coating is removed, the intensity of the loss pattern decreases. This behavior is shown in the figure 4.2.

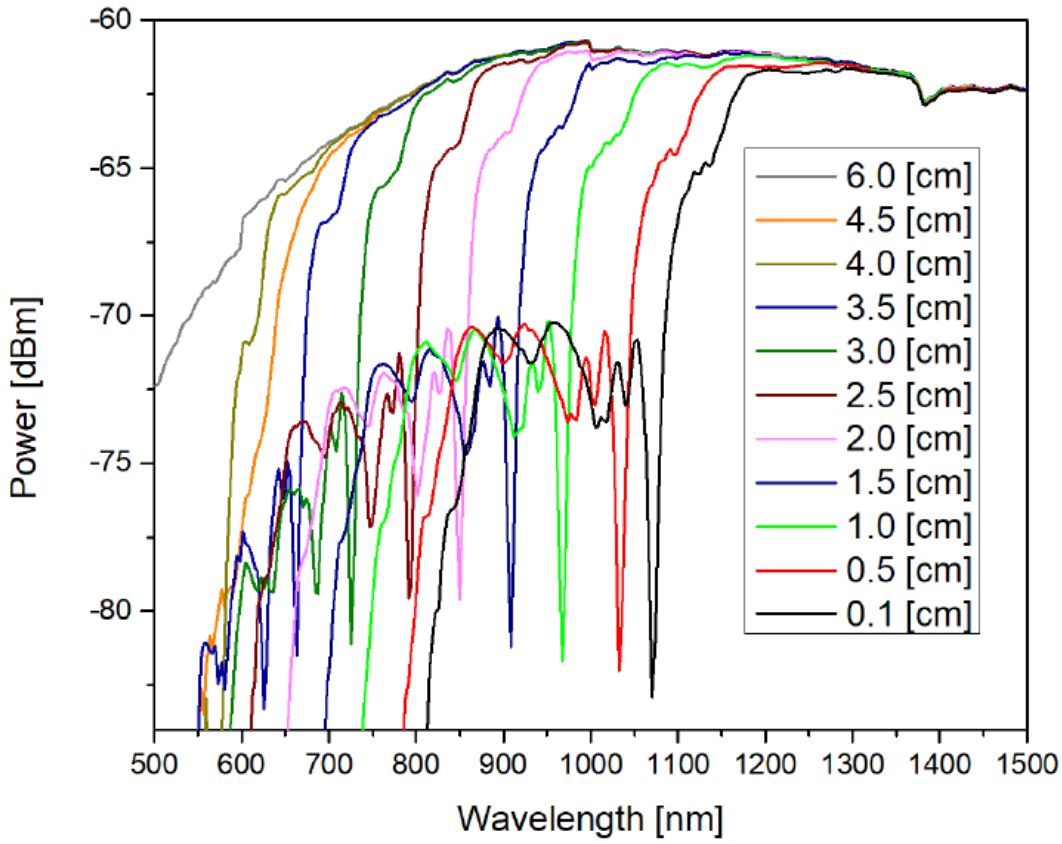

Figure 4.2: The loss in the fiber for different bendings by changing the bending diameter between the edges.

Subsequently, a data fitting was performed with the collected data for each peak as a function of their separation, and it was found that the data follow a linear behavior between the displacement of the last loss peak and the separation distance of the bending ends. From this data, we can extrapolate new values beyond the measurements taken with an R-squared fidelity greater than 99.85%. The remaining fitting data are available in the upper table accompanying the fit.

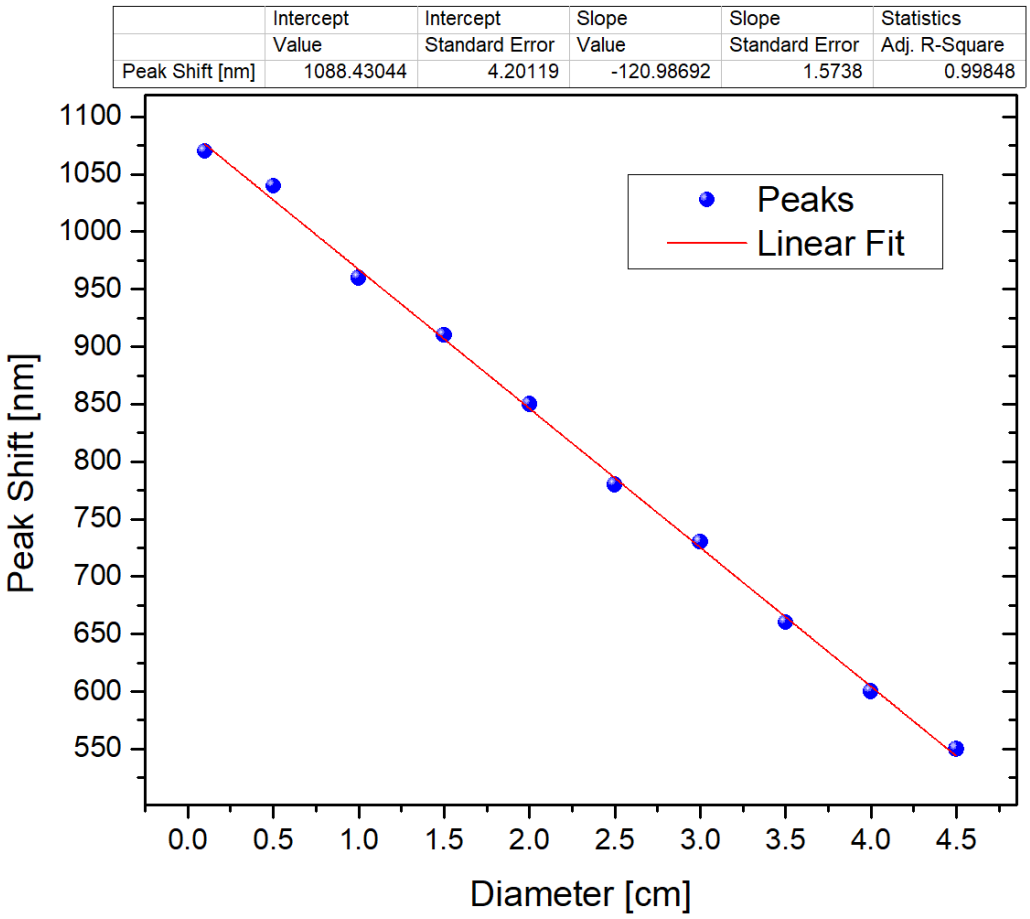

Figure 4.3: The fit for the shift of peaks for different bendings by changing the bending diameter between the edges.

4.3 Glycerin Concentration Measurements.

Subsequently, we selected the minimum separation as it allowed for a more efficient experimental implementation, with the transfer spectrum showing the last loss peak in the infrared range. The first setup used was to vary the bending diameter (figure 4.1b) and and then we use the second setup to measure the glycerin concentration (figure 4.1c).

After selecting the minimum separation for the bending, we decided to apply weights to the input and output of the bending, as this significantly increased the

system's losses. Due to the system's sensitivity to small variations in any of the possible degrees of freedom configuring the bending, multiple measurements had to be taken and the system parameters had to be carefully monitored to obtain a characteristic loss pattern. This pattern could then be analyzed for future variations when implemented as a refractometer. Newly all that is shown in 4.1c.

The measurements of the refractometer are of particular interest for our sensing platform, as they establish a basis for characterizing systems across multiple fields of interest, ranging from physical variables to biomedical variables, depending on future functionalizations of the system due to coatings that can be applied in the bending region.

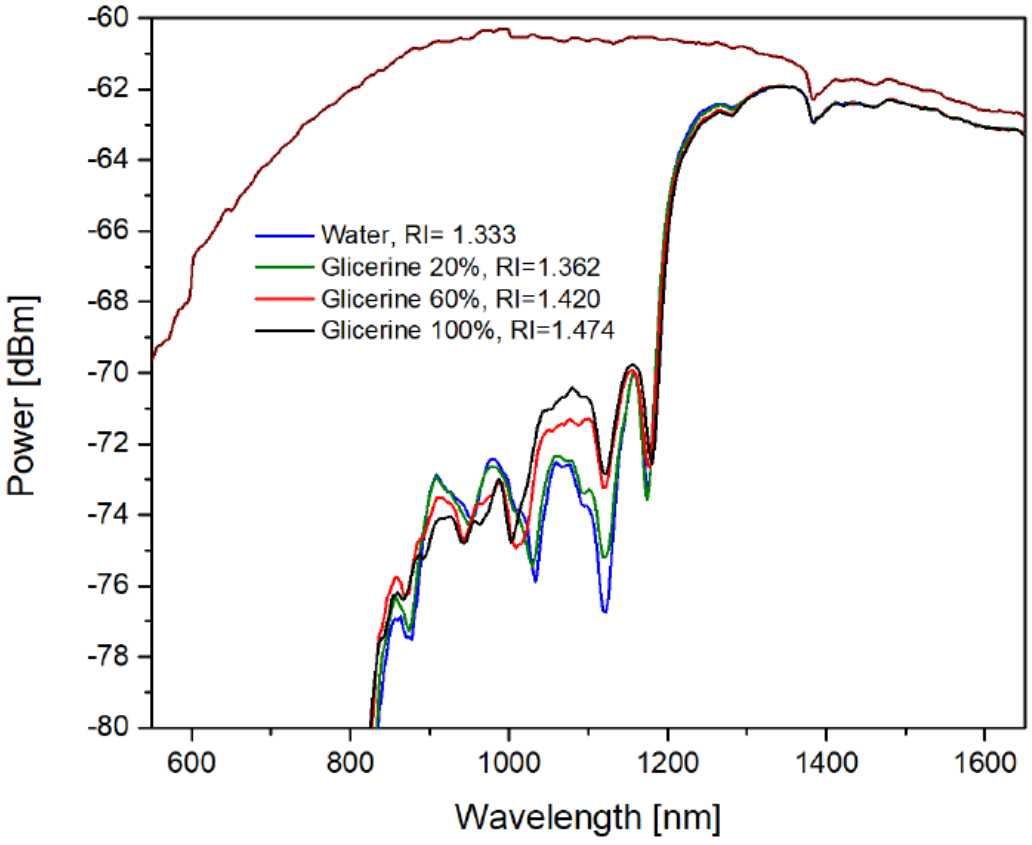

Figure 4.4: The behaviors of the losses for different concentration of glycerin.

In figure 4.4, we observe a family of functions from the transmission spectrum obtained for different concentrations of glycerin. We found a characteristic and stable pattern with variations in two peaks of interest. One peak shows variations in amplitude, while the other shows variations in wavelength. As mentioned earlier, the formation of these peaks is associated with phenomena occurring in the optical fiber coating in the bending region, as their removal results in a significant decrease in losses. It should be noted that the refractive index for air is 1.000, for distilled water it is 1.333, for 60% glycerin it is 1.420, and for 100% glycerin it is 1.474.

In figure 4.5, we can clearly observe the transmission of the fiber before and after removing the coating, as well as before and after applying the bending. This measurement was conducted for various bending diameters, but we only show the result for a bending diameter of 0.5 cm. The behavior was the same in all cases. Without bending, similar results were observed with and without coating. Upon applying the bending, greater losses were observed for the fiber with coating compared to the fiber from which the coating was removed. This is experimental evidence that, by using a single-mode fiber with high confinement losses, we are achieving strong resonance in the coating when the bending is applied.

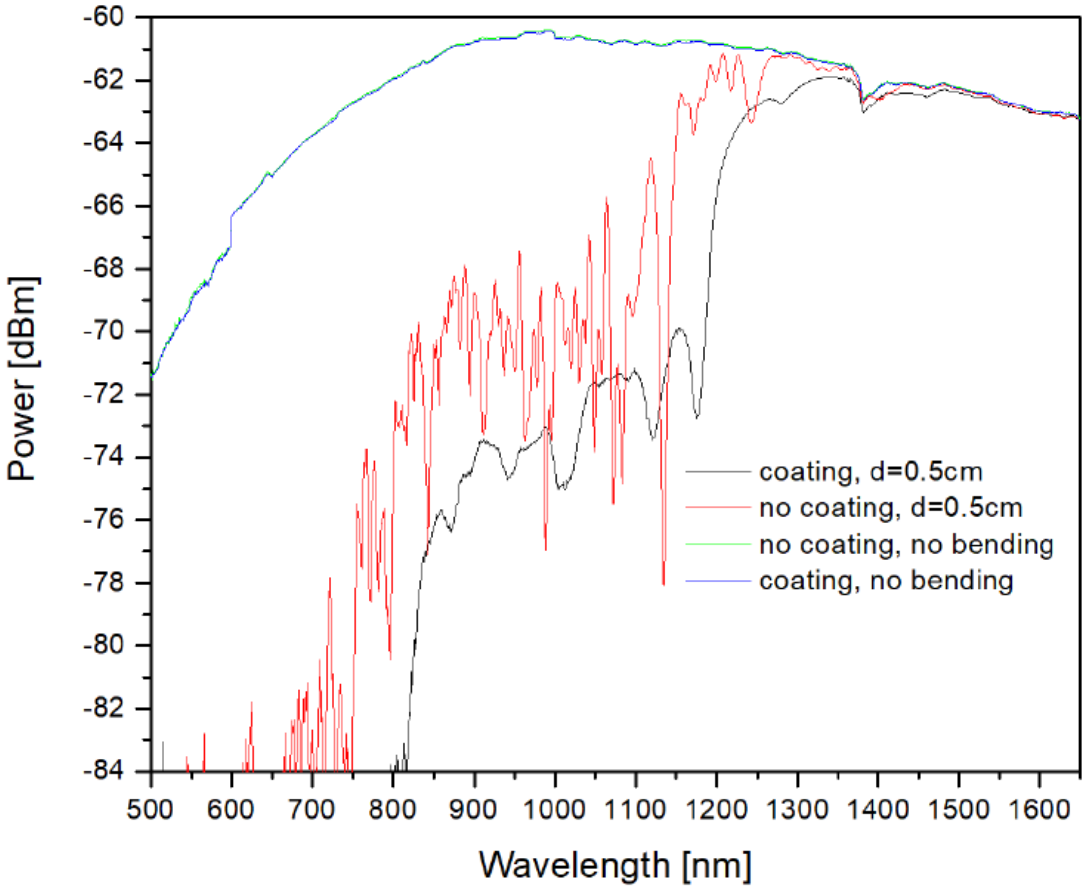

Figure 4.5: The response of the system with a polymer coating and without coating.

Now, by taking an enlargement of the region of interest where the aforementioned peaks are located for different glycerin concentrations, we can detail the variations observed for each peak (amplitude and wavelength) and establish a relationship between the concentration and the changes for each corresponding peak. The zoom is shown in the figure 4.6

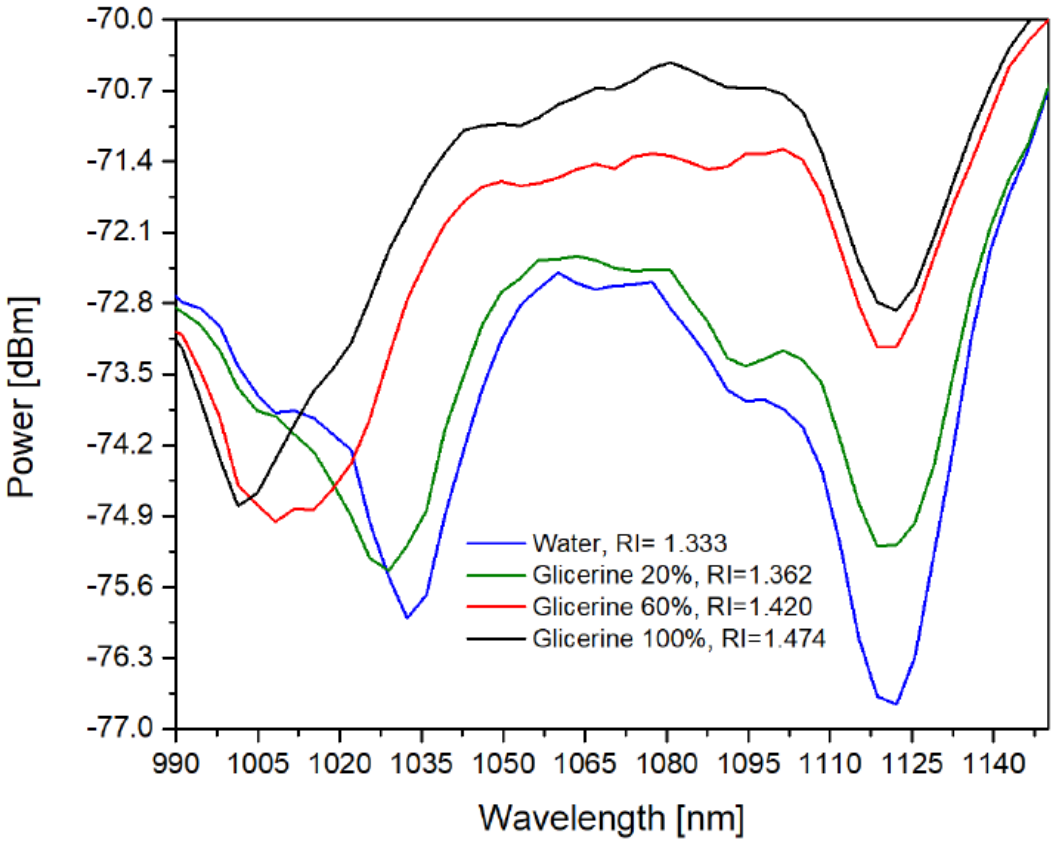

Figure 4.6: A zoom for the interest region in the transmission spectra for the platform of sensing.

After conducting multiple measurements to ensure a characteristic loss spectrum for different concentrations of glycerin in water, the transmission spectra of the sensing system were obtained. These transmission spectra show regular variations in two peaks of the loss pattern. Both variations are linear and vary according to the glycerin concentration with respect to the amplitude of the losses for the last peak of the loss pattern and the position of the penultimate peak within the same loss pattern.

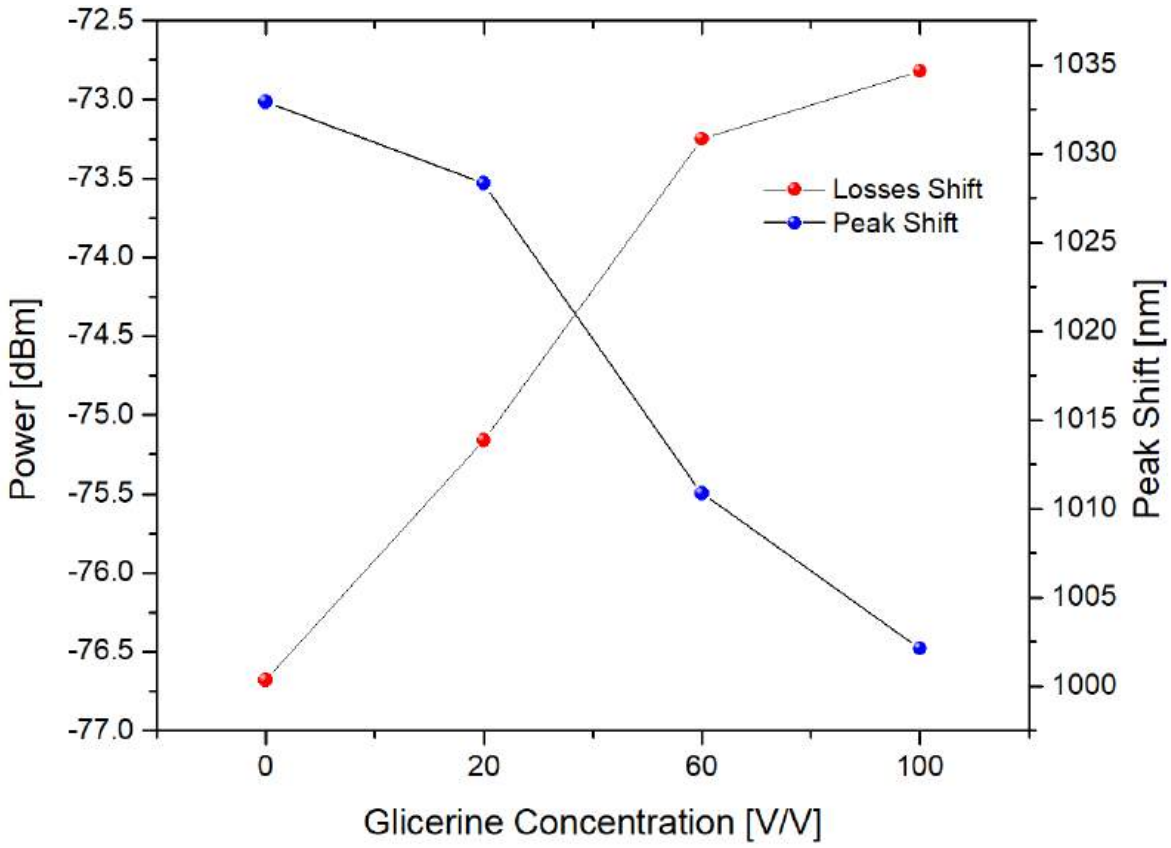

Figure 4.7: The variations in amplitude and wavelength for each peaks.

In the figure 4.7 we can see a record of the variations in amplitude and wavelength for the peaks of interest.

4.4 Fitting for the refractometer

The linear fit of the data for each peak of the loss pattern allows us to determine new sample concentrations through extrapolation. With these results, we can highlight that the configuration given to the dual-ring PCF enables the formation of a sensing system susceptible to variations in the refractive index for samples that can be brought into contact with the system's bending region.

In figure 4.8, the minima of the loss peaks for each glycerin concentration were plotted. The reduction in loss depth for each loss peak corresponds to the sample

change (water and 20% glycerin) and the densification of the medium for higher concentrations (60% and 100% glycerin), explaining the linear and positive trend of peak depth versus concentration. Additionally, the slope of 0.03826 represents the sensitivity of the system, as it is the ratio of the variation in losses in dBm with respect to the different glycerin concentration percentages.

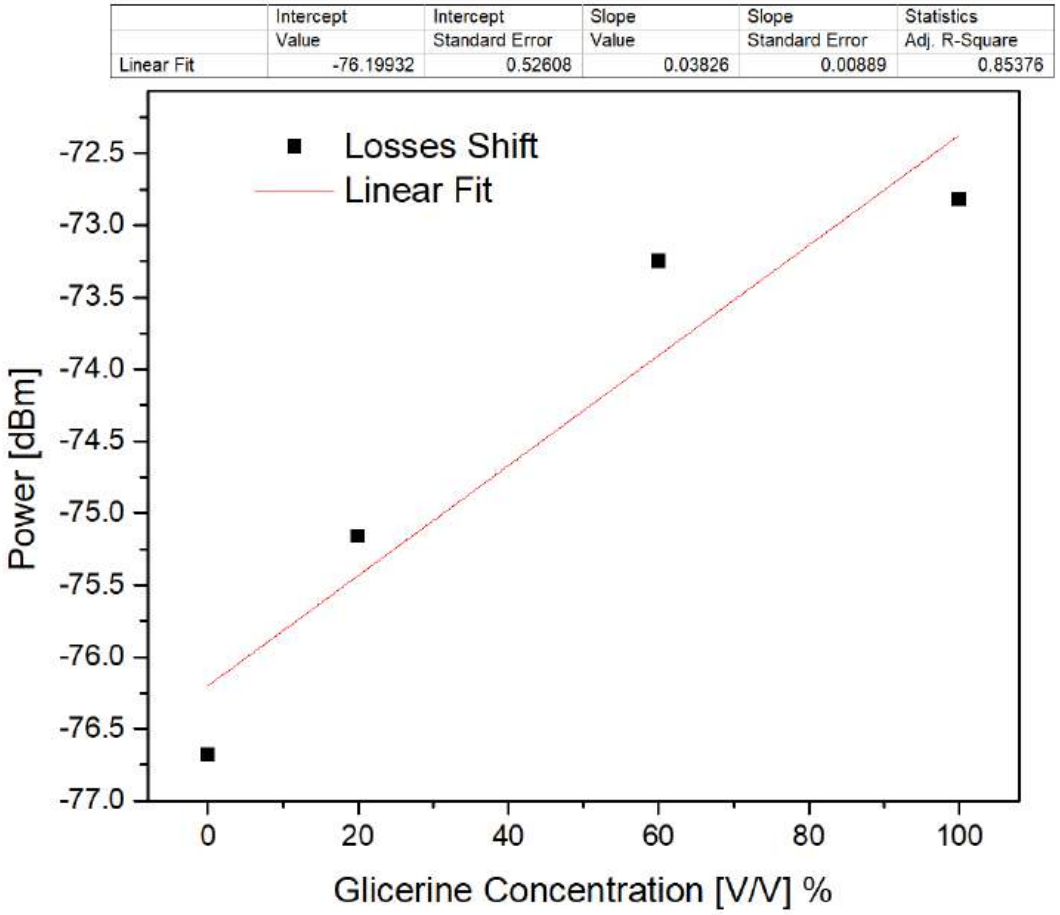

Figure 4.8: A fit for the first peak which has variations in losses

In both cases, linear fits were obtained with an R-squared of 85.38% for the first peak and 96.97% for the second peak. Recall that these variations correspond to wavelength and amplitude for each concentration. It is noteworthy that the displacement in wavelength and amplitude is anomalous because absorption should increase with higher concentration, and there should also be resonance at a higher wavelength

when the concentration increases. We believe this behavior is due to the formation of LMR in the bending region, resulting in low penetration of the evanescent field and, consequently, modified coupling conditions compared to the findings studied in previous chapters regarding this phenomenon.

It is also worth noting that the experimental system used as a multiparameter platform differs significantly from the initial design analyzed in Chapter 2, as the fiber used has 2 rings instead of 3, and bending was introduced along with some weights at the system's input and output. This added some birefringence to the system in exchange for obtaining a better loss profile within the transmission spectrum of the sensing platform. Additionally, the single-mode regime is maintained for both studies, and the characteristic of seeking high confinement losses depending on the number of rings is preserved.

In figure 4.9, the wavelength shifts of the other loss peak for each glycerin concentration were plotted. The blue shift of the wavelength for each loss peak minimum corresponds to the sample change (water and 20% glycerin) and the densification of the medium for higher concentrations (60% and 100% glycerin), explaining the linear and negative trend of the wavelength shift versus concentration. Additionally, the slope of -0.32386 represents the sensitivity of the system, as it is the ratio of the variation in wavelength shift of the other loss peaks with respect to the different glycerin concentration percentages.

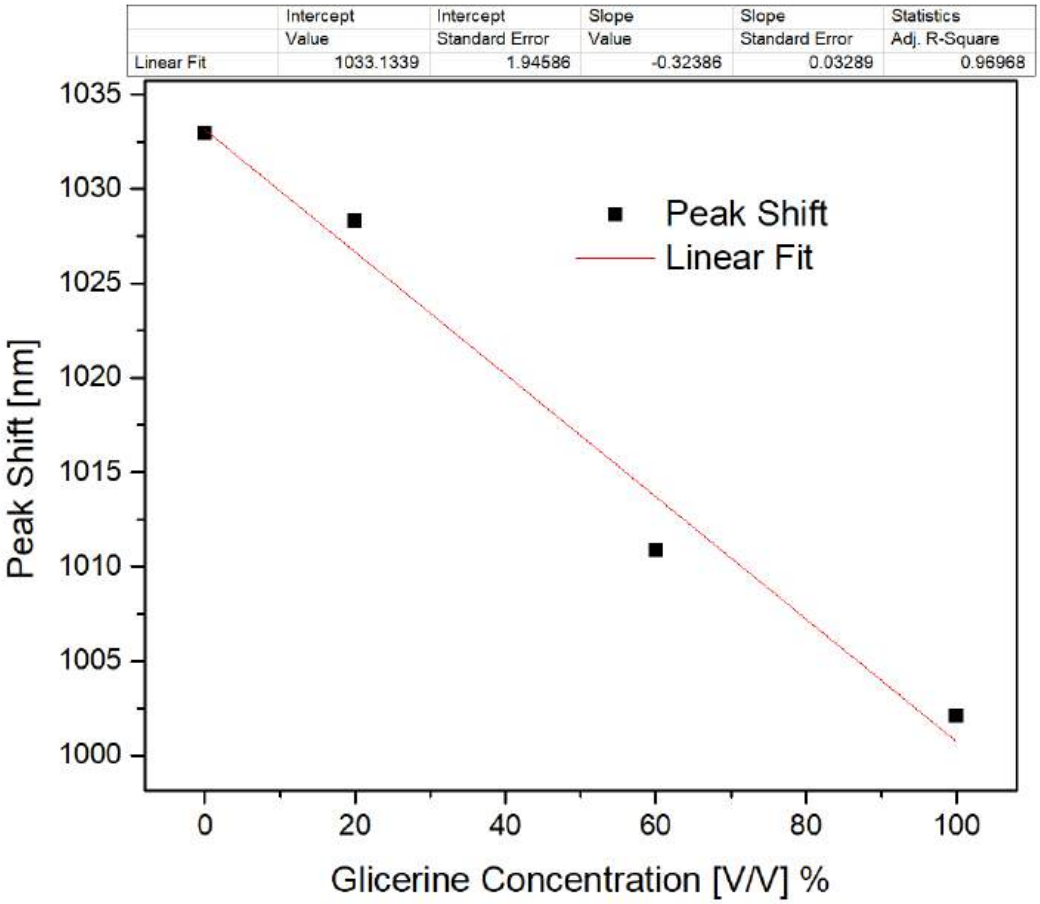

Figure 4.9: A fit for the second peak which has a wavelength shift.

During the completion of this doctoral thesis project, techniques were also developed to deposit layer-by-layer intercalated films of a graphene oxide and polymer. The aim was to find the ideal thickness by observing the resulting transmission spectrum and to enhance the device's functionality through the advantages offered by the graphene oxide in the field of biosensing. The characterization of the attenuation spectrum with respect to the number of the a graphene oxide and polymer layers is sheduled in the future work. The future work is proposed, as tests on this alternative system are ongoing, in conjunction with another doctoral thesis.

Conclusions

- A multiparameter detection system based on a special photonic crystal fiber was designed to study the formation of lossy mode resonance in an absorbing coating, the results were published in 2 scientific articles.

- It was found that the thicker the fiber waist, the greater the resonance length is obtained and it was also found that the thicker the absorbing coating, the more LMR modes it can support as they move towards the infrared.

- A multiparameter detection platform was built to measure variations in refractive index using a 2-ring single-mode optical fiber with high confinement losses.

- Linear fits were found for the bending diameter and its spectrum and the correlation of the variations of 2 characteristic peaks with the glycerin concentration.

- The influence of the coating on the formation of the characteristic loss peaks of the system was observed, this being an argument in favor of the formation of resonance modes in the coating.

Publications

1. **M. Salazar Sicachá**, Vladimir P. Minkovich, A.B. Sotsky, A.V. Shilov, L.I. Sotskaya, and E.A. Chudakov, "Lossy mode resonances in photonic crystal fibers", *Journal of the European Optical Society-Rapid Publications*, Vol. 17, No. 24, p. 1-12, 2021. DOI: 10.1186/s41476-021-00169-4

2. **M. Salazar Sicachá**, V.P. Minkovich, A.B. Sotsky, A.V. Shilov, L.I. Sotskaya, "Transmittance of tapered photonic crystal fibers with absorbing coatings", *Journal of Nanotechnology Research*, Vol. 4, No. 3, p.125-129, 2022. DOI: 10.26502/jnr.2688-85210035

Congress Participation

1. **M. Salazar Sicachá**, Vladimir P. Minkovich, A.B. Sotsky, A.V. Shilov, L.I. Sotskaya, "Transmittance of tapered photonic crystal fibers with absorbing coatings", *Proc. of EOS Conference, EOSAM 2020, EPJ Web of Conferences*, Vol. 238, 08005, p.1-2, 2020. DOI: 10.1051/epjconf/202023808005

2. **M. Salazar Sicachá**, Vladimir P. Minkovich, "Design, fabrication and characterization of nonlinear photonic crystal fibers for sources of correlated photon pairs", *Journal of Physics, Conference Series*, Vol. 2307, p. 1-6, 2022. DOI: 10.1088/1742-6596/2307/1/012005

3. **M. Salazar Sicachá**, J.S. Buriticá Bolaños, Vladimir P. Minkovich, Sergio Calixto, "Design and fabrication of special photonic crystal fibers for sensing applications", *Proc. of SPIE*, Vol. 12573, p.1-4, 2023. DOI: 10.1117/12.2664339

Groups of Collaboration

1. *Mogilev State University*, Physics Department, Mogilev (Belarus).

2. *Escuela Técnica Superior de Ingeniería de Bilbao*, Universidad del País Vasco (UPV), Bilbao, Spain.

Annexes

A.1 Matlab Code to Calculate Optical Properties in a PCF.

```
%script basado en los articulos de Koshiba y Saitoh.
clc, clear;

%definición de los parámetros experimentales para hacer la aproximacion del
%método full-vectorial mediante un modelo experimental; los vectores a,b
%contienen la información de los parámetros de ajuste para V y los
%parámetros c,d contienen los parámetros de ajuste para W.

a = [
    [0.54808 0.71041 0.16904 -1.52736];
    [5.00401 9.73491 1.85765 1.06745];
    [-10.43248 47.41496 18.96849 1.93229];
    [8.22992 -437.50962 -42.4318 3.89]
];

b = [
    [5 1.8 1.7 -0.84];
    [7 7.32 10 1.02];
```

```
19      [9 22.8 14 13.4]
20  ];
21
22  c = [
23      [-0.0973 0.53193 0.24876 5.29801];
24      [-16.70566 6.70858 2.72423 0.05142];
25      [67.13845 52.04855 13.28649 -5.18302];
26      [-50.25518 -540.6647 -36.80370 2.7641]
27  ];
28
29  d = [
30      [7 1.49 3.85 -2];
31      [9 6.58 10 0.41];
32      [10 24.8 15 6]
33  ];
34
35  %parámetros para usar la formula de sellmeier
36
37  f = [0.696166300 0.407942600 0.897479400];
38
39  g = [4.67914826E3 1.35120631E4 97.9340025E6];
40
41  %fibra 3
42  hd = 1.15E3;
43  hp = 1.65E3;
44
45  %Radio
46  R = hd/hp;
47  %R=0.4;
48  %hp=2.5E3;
```

```
49
50 %nucleo y dispersión constantes
51 %nCsilice = 1.548;
52 %Dm = -1.85E-4;
53 %nCaire = 1;
54
55 %coeficientes calculados a partir de los datos experimentales para usarlos
56 %en la estimación del valor de los parametros V (Ai) y W (Bi).
57 A1 = a(1,1) + a(2,1)*R^(b(1,1)) + a(3,1)*R^(b(2,1)) + a(4,1)*R^(b(3,1));
58 B1 = c(1,1) + c(2,1)*R^(d(1,1)) + c(3,1)*R^(d(2,1)) + c(4,1)*R^(d(3,1));
59 A2 = a(1,2) + a(2,2)*R^(b(1,2)) + a(3,2)*R^(b(2,2)) + a(4,2)*R^(b(3,2));
60 B2 = c(1,2) + c(2,2)*R^(d(1,2)) + c(3,2)*R^(d(2,2)) + c(4,2)*R^(d(3,2));
61 A3 = a(1,3) + a(2,3)*R^(b(1,3)) + a(3,3)*R^(b(2,3)) + a(4,3)*R^(b(3,3));
62 B3 = c(1,3) + c(2,3)*R^(d(1,3)) + c(3,3)*R^(d(2,3)) + c(4,3)*R^(d(3,3));
63 A4 = a(1,4) + a(2,4)*R^(b(1,4)) + a(3,4)*R^(b(2,4)) + a(4,4)*R^(b(3,4));
64 B4 = c(1,4) + c(2,4)*R^(d(1,4)) + c(3,4)*R^(d(2,4)) + c(4,4)*R^(d(3,4));
65
66 syms l;
67
68 %Definición de las ecuaciones para las magnitudes física de interés a partir
69 %de los parámetros definidos previamente
70 nm = (1 + (f(1) * l^2)/(l^2 - g(1)) + (f(2) * l^2)/(l^2 - g(2)) +
71 (f(3) * l^2)/(l^2 - g(3)))^(1/2);
72 nC = subs(nm,l);
73
74 V = A1 + A2/(1+A3*exp(A4*l/hp));
75 W = B1 + B2/(1+B3*exp(B4*l/hp));
76 nFSM = (nC^2-(V*l/(2*pi*hp/3^(1/2)))^2)^(1/2);
77 nEFF = (nFSM^2+(W*l/(2*pi*hp/3^(1/2)))^2)^(1/2);
78
```

```
%calculo de la dispersión a partir de la dispersión material y la
%dispersión material.
Dm = diff(nC,1);
D2nEFF = diff(nEFF,2);
D = -(l/3E-7)*D2nEFF + Dm/3E-7;

l = 500:10:2200;
l1 = l+120;
hold on;

win = figure(1);
win(1) = subplot(5, 2, [1,2]);
win(2) = subplot(5, 2, [3,4]);
win(3) = subplot(5, 2, [5,6]);
win(4) = subplot(5, 2, [7,8]);
win(5) = subplot(5, 2, [9,10]);

set(win,'Nextplot','add');

y = double(subs(D,l1));
plot(win(1),l,y);
%title(win(1),'Dispersión Cromática');
xlabel(win(1),'\lambda [nm]');
ylabel(win(1),'D [ps/(Km-nm)]');
win(1).XGrid = 'on';
win(1).YGrid = 'on';
%axis([600 1600 -200 200])

%calculo de la apertura numérica
acore=hp/sqrt(3);
```

```
109 w0 = 1E-3*acore*(0.65 + 1.619./(double(subs(V,l1)).^(3/2)) +
110 2.879./(double(subs(V,l1)).^6));
111 plot(win(2),l,w0);
112 %title(win(2),'Radio del Modo Fundamental');
113 xlabel(win(2),'\lambda [nm]');
114 ylabel(win(2),'\omega [\mu m]');
115 win(2).XGrid = 'on';
116 win(2).YGrid = 'on';
117 %axis([-1 1 0 1.1])
118
119 NA = double(subs(V,l1)).*(l1)./(2*pi*acore);
120 plot(win(3),l,NA);
121 %title(win(3),'Apertura numérica');
122 xlabel(win(3),'\lambda [nm]');
123 ylabel(win(3),'NA');
124 win(3).XGrid = 'on';
125 win(3).YGrid = 'on';
126 %axis([-1 1 0 1.1])
127
128 Veff = double(subs(V,l1));
129 plot(win(4),l,Veff);
130 %title(win(4),'Frecuencia normalizada');
131 xlabel(win(4),'\lambda [nm]');
132 ylabel(win(4),'V');
133 win(4).XGrid = 'on';
134 win(4).YGrid = 'on';
135 %axis([-1 1 0 1.1])
136 %{
137 subplot(5,2,6);
138 Nc = double(subs(nC,l1));
```

```
plot(l,Nc);
title('Índice Core');
xlabel('\lambda [nm]');
ylabel('nCore');
%axis([-1 1 0 1.1])
grid on;

subplot(5,2,7);
Neff = double(subs(nEFF,l1));
plot(l,Neff);
title('Índice Efectivo');
xlabel('\lambda [nm]');
ylabel('nEFF');
%axis([-1 1 0 1.1])
grid on;

subplot(5,2,8);
Nfsm = double(subs(nFSM,l1));
plot(l,Nfsm);
title('Indice Cladding');
xlabel('\lambda [nm]');
ylabel('nFSM');
%axis([-1 1 0 1.1])
grid on;
%}
CNL = 6*(3.2E-2)./((l1)*hp^2)*1E12;
plot(win(5),l,CNL);
%title(win(5),'Coeficiente de no-linealidad');
xlabel(win(5),'\lambda [nm]');
ylabel(win(5),'\gamma [Km-W]^{-1}');
```

```
169 win(5).XGrid = 'on';
170 win(5).YGrid = 'on';
```

A.1.1 Matlab Code to desing tubs from Stack in a PCF.

```
1  %código para generar el Stack de la PCF
2  ph = 1;
3  hd = 0.5;
4  x = 0;
5  y = 0;
6  n = 8;
7
8  hold on
9
10 %Algoritmo que crea el stack poniendo esferas equidistantes en cada anillo
11 for i = 1:n
12    for j=0:i*6
13          viscircles([x+i*ph*cos(2*pi/(i*6)*j),y+
14          i*ph*sin(2*pi/(i*6)*j)],ph/2,'EdgeColor','b');
15          viscircles([x+i*ph*cos(2*pi/(i*6)*j),y+
16          i*ph*sin(2*pi/(i*6)*j)],hd/2,'EdgeColor','b','LineStyle','--');
17    end
18 end
19
20 viscircles([x,y],(n+0.5)*ph,'EdgeColor','black');
21 viscircles([x,y],(n+1)*ph,'EdgeColor','black');
22 viscircles([x,y],ph/2,'EdgeColor','r');
```

A.2 Absorbing Coating with Films of Graphene Oxide and Polymer.

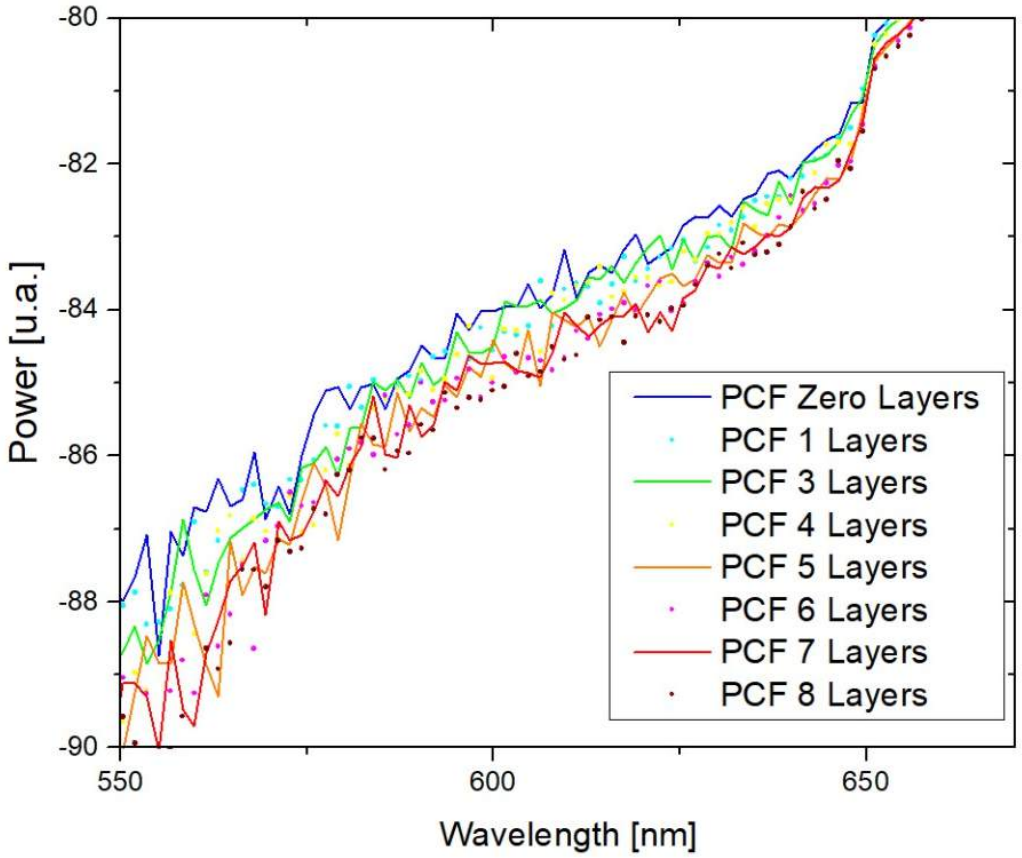

Figure A.1: Comparison of the transmission of PCF with Absorptive Coating for Different Numbers of Interleaved Layers of Graphene Oxide and Polymer.

Figure A.1 shows the transmission spectrum of a photonic crystal fiber from which a 6 cm segment of the cladding has been removed. Subsequently, alternating layers of graphene oxide (GO) and PEI (a polymer based on ethylenimine monomers) were deposited via an electrochemical process. The figure shows that the transmission pattern is the same for each sample, but as more GO-PEI layers are added, the transmitted power decreases due to the losses generated by the cladding, which absorbs an increasing amount of energy as its thickness increases. This is an indication that the cladding thickness gradually increases with the applied electrochemical deposition

method, which can be used to add layers in a controlled manner. Later, through a bending configuration like the one shown in Chapter 4, a system based on the LMR phenomenon can be implemented to perform sensing measurements, taking advantage of the GO properties through specific functionalizations.

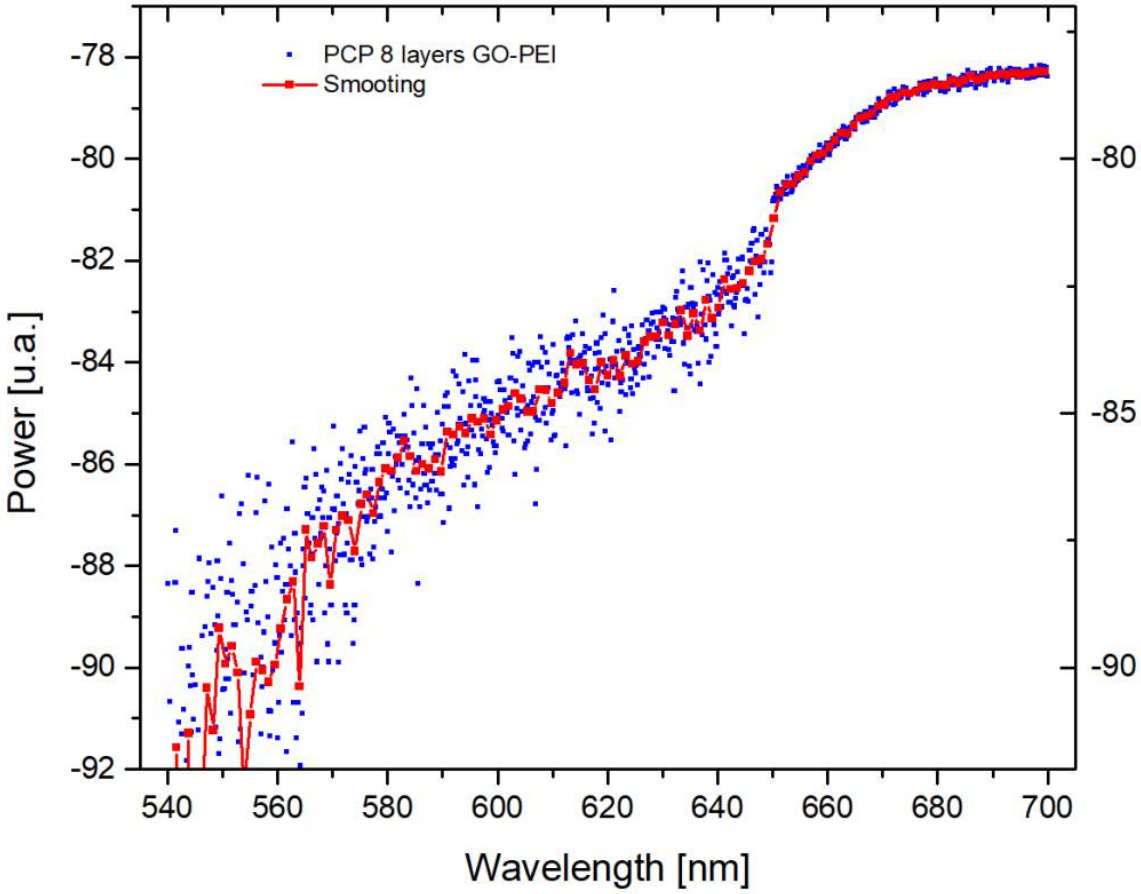

Figure A.2: The transmission of PCF with Absorptive Coating for 8 Interleaved Layers of Graphene Oxide and Polymer.

Figure A.2 specifically shows the data distribution obtained for the transmission spectrum of a PCF on which 8 layers of GO-PEI have been deposited. Additionally, a fit is performed to analyze the average trend of losses concerning wavelength. Once the data adjustments were made for each of the layers that were being added, they were plotted as shown in the previous figure to observe their overall behavior.

A.3 Analysis of the Photonic Crystal Fiber with 3 Rings for Bending Configuration

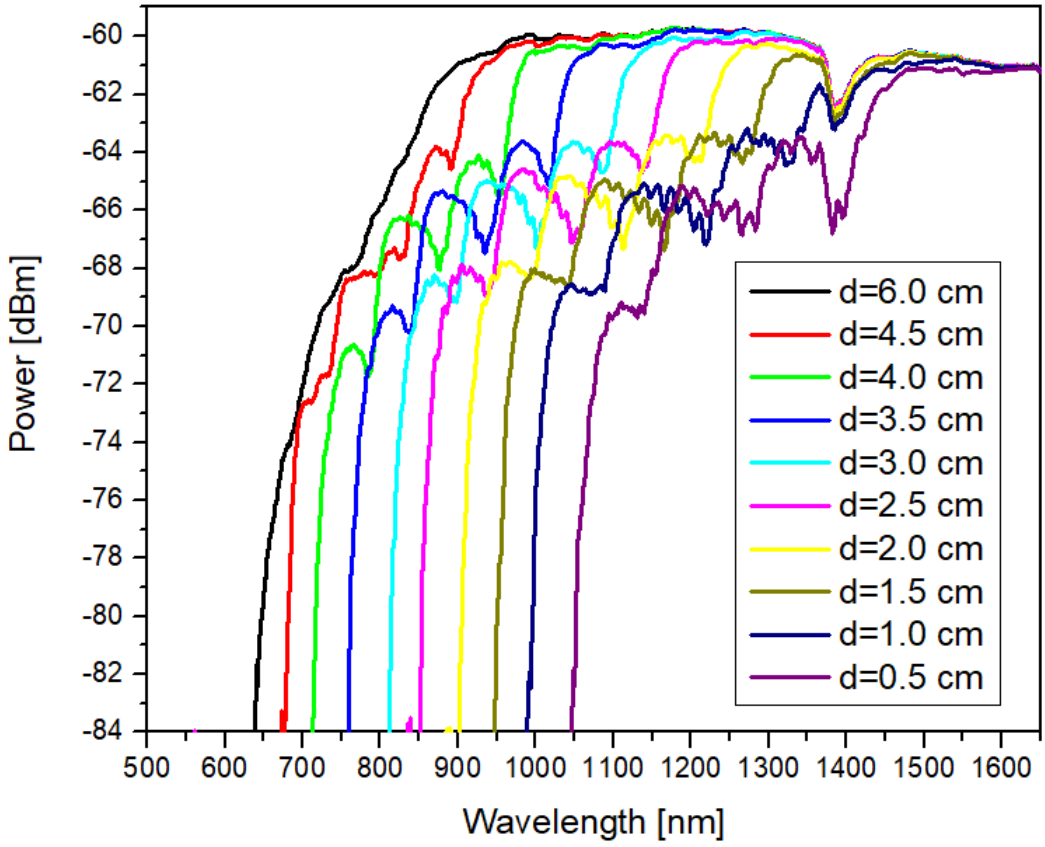

Figure A.3: The transmission of the Photonic Crystal Fiber with 3 Rings for Bending Configuration.

In the figure A.3, we can observe the transmission of an optical fiber with 3 hexagonal rings used in the bending configuration. We can see a behavior analogous to that observed in the system with 2 rings, as there is a loss pattern associated with the curvature applied to the fiber and a redshift as the bending increases. On the other hand, when comparing the losses, it is observed that the 2-ring fiber experiences losses 4 times greater. This is because the depth of the peaks for the 3-ring fiber is around 5 dBm, while for the 2-ring fiber, depths of 20 dBm are observed. This difference in the loss pattern is justified by the design of the fibers used, as the confinement losses

in the fundamental mode increase with a lower number of rings.

A.4 Analysis of coupling losses in a splice between PCF and SMF-28.

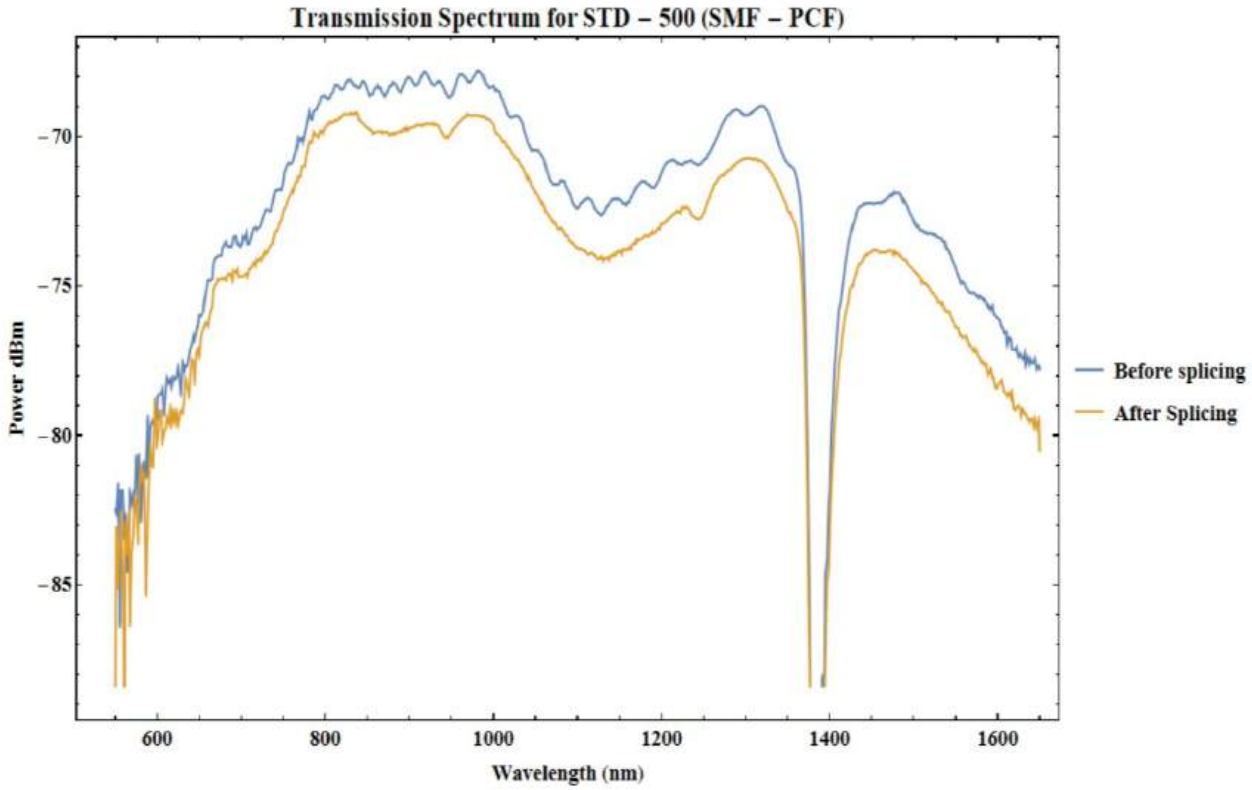

Figure A.4: Results of the transmission spectrum measurements before and after splicing the 2-ring PCF and SMF-28 sections.

It can be observed in figure A.4 a splice that was made by adjusting the STD (Standard) option, which defines the power of the arc discharge used for the splicing, while maintaining a constant fusion time of 100 ms. It is possible to see that after splicing the conventional fiber with the 2-ring PCF, low and stable losses are obtained under the employed configuration. These losses are around 2 dBm across the entire spectrum. Therefore, this splice allows remote measurement in the PCF using conventional fiber, which is advantageous since SMF-28 is more durable than the 2-ring PCF. This result also enables us to couple the 2-ring PCF system and work with the

phenomena it generates, such as LMR (Lossy Mode Resonance), to transmit the signal to other conventional optical devices. All of this is possible thanks to the design of the 2-ring PCF, which has a fundamental mode diameter smaller than 7 μm.